

論文 / 著書情報
Article / Book Information

題目(和文)	
Title(English)	Nonthermal plasma-enabled catalysis of methane dry reforming
著者(和文)	ShengZunrong
Author(English)	Zunrong Sheng
出典(和文)	学位:博士(工学), 学位授与機関:東京工業大学, 報告番号:甲第11636号, 授与年月日:2020年9月25日, 学位の種別:課程博士, 審査員:野崎 智洋,山中 一郎,末包 哲也,肖 鋒,赤坂 大樹
Citation(English)	Degree:Doctor (Engineering), Conferring organization: Tokyo Institute of Technology, Report number:甲第11636号, Conferred date:2020/9/25, Degree Type:Course doctor, Examiner:,,,,,
学位種別(和文)	博士論文
Type(English)	Doctoral Thesis

Nonthermal plasma-enabled catalysis of methane dry reforming

A DISSERTATION

SUBMITTED TO THE FACULTY OF SCHOOL OF ENGINEERING,
GRADUATE MAJOR OF ENERGY SCIENCE AND ENGINEERING
OF TOKYO INSTITUTE OF TECHNOLOGY

BY

Sheng Zunrong

IN PARTIAL FULFILLMENT OF THE REQUIREMENTS
FOR THE DEGREE OF
DOCTOR OF ENGINEERING

Supervisor:

Professor Tomohiro Nozaki

June 2020

Abstract

This thesis presents the experimental study of nonthermal plasma-enabled methane dry reforming ($\text{CH}_4 + \text{CO}_2 \rightarrow 2\text{H}_2 + 2\text{CO}$), aiming for providing deep insight into plasma-catalyst interfacial physicochemical phenomena. The DBD (dielectric barrier discharge) provides vibrationally excited species by low-energy electron impact. Firstly, oxidation behavior of Ni/Al₂O₃ catalyst was clarified that DBD-activated CO₂ enables a surface NiO layer formation which further drives oxidation-reduction cycle for coke suppress. Then a comprehensive surface chemistry study on lanthanum-modified Ni/Al₂O₃ catalyst reveals DBD-activated CO₂ enhances surface carbonate species formation, which provides abundant adsorbed oxygen-contained species to chemisorbed CH₄ in surface reaction. The study of electrical properties and electron collision kinetics demonstrates that increase of the mean discharge current is critical to strengthen plasma-induced synergism via vibrationally excited CH₄. Finally, kinetic analysis reveals that the activation energy decreases from 91 to 44.7 kJ/mol, which is correlated with the state-specific gas-surface reactivity of CH₄ on Ni surfaces.

Acknowledgment

This PhD thesis is the result of a three-year research project carried out at Tokyo Institute of Technology. I have many people to acknowledge for their support and contribution to my doctoral research.

First and foremost, I have deepest gratitude to my supervisor Prof Tomohiro Nozaki for his patient guidance and continuous support. He has supported overall theoretical guidance and experimental setups for this thesis. I also appreciate his guidance in technical writing and conference presentation. His direction and suggestion helped me to move forward with investigation in depth and achieve my goal.

My sincere thanks also go to Dr. Hyun-Ha Kim (AIST). He supports the DRIFTS experiment setup for me and gave me detailed guidance in AIST. Moreover, the EDS analysis in this thesis is supported by Dr. Kim. It is a pleasure to thank Prof. Shuiliang Yao (Changzhou University). Prof. Yao is an excellent expert on plasma-DRIFTS and provided a lot of support to this thesis.

I have deep gratitude for my fellow numbers who ever worked with me together in reforming group: Seigo Kameshima, Takumi Yamazaki, Kenta Sakata, Yoshiki Wantanabe, Adrianto Dimas, Xiaozhong Chen, Sho Murata, Shuhei Wakamastu. It is difficult to achieve my research goal without your enormous contribution.

I am also deeply grateful to other excellent fellow numbers in Nozaki Lab: Atushi Saito, Kotaro Takehana, Tani-san (secretary), Firman Bagjia Juangsa, Yoshiki Muroya, Naoki Koda, Hironori Takastu, Yuma Tanabe, Munechika Ostuka, Shogo Shibata. Thanks for your help in my daily life in Japan.

I would like to express my gratitude to my thesis examination committee: Prof Tomohiro Nozaki, Prof Tetsuya Suekane, Prof Feng Xiao, Prof Hiroki Akasaka, Prof Ichiro Yamanaka for reviewing this thesis.

I cannot neglect to mention that I was fortunate to get financial support from China Scholarship Council (CSC) for living fee and TokyoTech for tuition fee exemption, which make me throw myself into research.

Last, but not least, my deep and sincere gratitude to my family. Dear Mom and Dad: Thanks for your love without any thought of rewarding. I would never be the person I am without your continuous support and encouragement. Ms. Wenzhu Wu: Thanks for your accompanying, thousands miles away. It is nice to have you with me when I'm lonely.

June 2020

Zunrong Sheng

Tokyo Institute of Technology

Nomenclature

DBD	Dielectric barrier discharge
DRIFTS	Diffuse reflectance infrared Fourier transform spectroscopy
GHSV	Gaseous hourly space velocity (h^{-1})
MDR	Methane dry reforming
QMS	Quadrupole mass spectrometer
SEI	Special energy input ($\text{eV}/\text{molecule}$)
TPD	Temperature programmed desorption
TPR	Temperature programmed reduction

Table of content

Chapter 1: Introduction.....	1
1.1 Overview	3
1.2 Methane dry reforming	3
1.2.1 Opportunities	3
1.2.2 Challenges	4
1.3 Nonthermal plasma	5
1.3.1 Classification of plasma	7
1.3.2 Dielectric barrier discharge (DBD)	9
1.3.3 Other nonthermal plasma	11
1.4 Thermodynamics.....	14
1.4.1 Thermodynamic analysis for low-temperature operation.....	14
1.4.2 Thermodynamic equilibrium	17
1.5 Kinetic research.....	18
1.5.1 Power-law kinetics and activation energy	18
1.5.2 Kinetics-related surface reactions.....	20
1.6 Scope of this thesis.....	23
1.7 References	26
Chapter 2: Oxidation behavior of Ni/Al ₂ O ₃ catalyst	40
2.1 Abstract	40
2.2 Introduction.....	40
2.3 Experiment methods	43
2.4 Mixed oxidation route	46
2.5 Plasma-enhanced direct oxidation route	50
2.5.1 Raman spectroscopy	50

2.5.2 Plasma species generation and penetration	51
2.5.3 H ₂ -TPR	53
2.6 Plasma-enabled new reaction pathway	55
2.7 Conclusions	57
2.8 References	58
Chapter 3: CO ₂ activation behavior over La-Ni/Al ₂ O ₃ catalyst	64
3.2 Introduction	65
3.3 Experimental section	67
3.3.1 In situ DRIFTS	67
3.3.2 Ex situ CO ₂ -TPD	68
3.4 Catalyst characterization	69
3.5 Enhanced carbonate formation by nonthermal plasma	71
3.5.1 In situ plasma-DFIFTS study	71
3.5.2 Ex situ CO ₂ -TPD study	75
3.6 Carbonate-induced reaction pathway	77
3.6.1 In situ high-temperature DRIFTS study	77
3.6.2 Relationship between carbonate formation and CH ₄ conversion	80
3.6.3 Reaction mechanism of plasm-enhanced MDR	81
3.7 Oxidation-reduction behavior of La-Ni/Al ₂ O ₃	83
3.8 Conclusion	86
3.9 Reference	86
Chapter 4: Electrical properties of dielectric barrier discharge	92
4.1 Abstract	92
4.2 Introduction	93
4.3 Experimental section	94

4.3.1 Experimental system	94
4.3.2 Parameter definition	96
4.3.3 Experimental condition	97
4.4 General reforming behavior	98
4.4.1 Pulsed reforming spectrometry.....	98
4.4.2 Conversion and selectivity	99
4.5 Discharge characteristics.....	101
4.5.1 Discharge power and controlling parameters	101
4.5.2 Voltage-Current characteristics.....	104
4.5.3 Other properties	105
4.6 Electron collision kinetics	108
4.7 Conclusion	112
4.8 Reference	114
Chapter 5: Kinetic study on methane dry reforming	119
5.1 Abstract	119
5.2 Introduction.....	119
5.3 Experimental section.....	122
5.3.1 Experimental system	122
5.3.2 Temperature measurement.....	122
5.4 Kinetic analysis	123
5.4.1 Reaction order for thermal reaction.....	123
5.4.2 Surface coverage	126
5.4.3 Reaction order for plasma hybrid reaction	127
5.4.4 Arrhenius curve	130
5.5 State-specific CH ₄ activation	135

5.6 Correlation between kinetic and plasma parameters.....	138
5.7 Conclusion	143
5.8 References.....	144
Chapter 6: Conclusion and future work.....	149
6.1 Conslusion.....	149
6.2 Future work.....	152
6.3 References.....	154

Table of figures

Figure 1.1 Coke formation in Ni catalyst: (a) Ni-C-H-O phase diagram (900 K and 1 atm) [57]. (b) the NiC formation mechanism [58], (c) carbon distribution in Ni/Al ₂ O ₃ pellet after reforming [59].	5
Figure 1.2 The time-scales of plasma and catalytic reaction [63].	6
Figure 1.3 Classification of atmospheric pressure plasma sources [72]. (Color region is modified by Ref.[76]. APPJ: atmospheric pressure plasma jet; DBD: dielectric barrier discharge; MPJ: microwave plasma jet; MPT: microwave plasma torch; MTD: microwave torch discharge; TIA: plasma torch with axial plasma injection.	8
Figure 1.4 Schematic diagram of catalyst-packed DBD reactor.	9
Figure 1.5 Surface streamers propagating over the surface of Al ₂ O ₃ by ICCD camera [90]. ...	9
Figure 1.6 Equivalent electrical circuit of DBD reactor: (a) empty-DBD and (b) packed-bed DBD. The subscript d, g, and c is abbreviation for dielectric material, gas, and catalyst respectively.	11
Figure 1.7 Schematic structure of high frequency plasma: (a) RF plasma and (b) MW plasma.	13
Figure 1.8 Energy diagram of methane dry reforming [135].	15
Figure 1.9 Conversion of CH ₄ (red symbol) and CO ₂ (green symbol) as a function of <i>SEI</i> at room temperature with different catalysts [136-145]. 1 eV/molecule \approx 4 kJ/L.	16
Figure 1.10 Thermodynamic equilibrium composite of MDR: initial input of CH ₄ and CO ₂ are 1 mol respectively; pressure = 5 kPa; Coke formation is omitted.....	17
Figure 1.11 Activation energy (<i>E_a</i>) in of methane dry reforming according to (a-i) thermal	

catalysis and (j-k) plasma catalysis over different catalyst: (a) Ni/SiO₂ [157]; (b) Ni/SiO₂ [158]; (c) Ni/MgO [158]; (d) Ni/TiO₂ [158]; (e) Ni/La/Al₂O₃ [159]; (f) Ni/CaO-Al₂O₃ [160]; (g) Ni-K/CeO₂-Al₂O₃ [161]; (h) LaNiO₃ [162]; (i) LaSrNiO₄ [163]; (j) Ni/La₂O₃@SiO₂ [164]; (k) Ni/La₂O₃-MgAl₂O₃ [153]. 19

Figure 1.12 Reaction coordinate diagram for working principle of (a) catalyst [69] and (b) nonthermal plasma with vibrational excitation [169]..... 21

Figure 1.13 CO₂-derived oxygen fixation: (a) lattice oxygen formation mechanism over photocatalytic material [176]; (b) adsorbed oxygen formation mechanism over basic material. 22

Figure 2.1 Experimental system: (a) overview; (b) cross-sectional view..... 44

Figure 2.2 Temperature programmed plasma oxidation of Ni catalyst (Run *a*): CO signal is multiplied by 10..... 46

Figure 2.3 CO₂ conversion as a function of *SEI* in DBD without catalys. Cited literatures from □Aerts [41]; ○Butterworth [42]; ΔBrehmer [43]. 47

Figure 2.4 Temperature programmed thermal oxidation of Ni catalysts by CO₂ (Run *b*)..... 48

Figure 2.5 Ni oxidation pathways: (a) Thermal oxidation with direct oxidation route including CO₂ adsorption near the perimeter of Ni catalysts. (b) DBD-enhanced mixed oxidation route. Inset pictures show hemispherical catalyst pellets after plasma and thermal oxidation. 49

Figure 2.6 NiO distribution over the cross-section of catalyst pellets: (a) Plasma oxidation (Run *c*); and (b) Thermal oxidation (Run *d*) with optical microscope images..... 51

Figure 2.7 The morphology of Ni/Al₂O₃ catalyst by SEM..... 52

Figure 2.8 The TPR profiles after (a) thermal oxidation and (b) DBD oxidation; (c) and (d)

schematic diagrams of oxidation behavior of Ni catalyst.....	54
Figure 2.9 (a) NiO formation by DBD-excited CO ₂ , (b) Nonthermal plasma heating mechanism, (c) CH ₄ conversion within NiO shell having no coke in the internal pores, (d) Thermal catalysis with significant coke formation in the internal pores. Carbon mapping is cited from ref. [25].	57
Figure 3.1 In situ plasma-DRIFTS cell: (a) schematic diagram; (b) overall view; (c) top-view; and (d) and (e) emissions from plasma.....	68
Figure 3.2 XRD patterns of (a) Ni/Al ₂ O ₃ , (b) La-Ni/Al ₂ O ₃ , and (c) LaNiAl ₁₁ O ₁₉ , where ○ Ni; LaNiAl ₁₁ O ₁₉ ; ◇ Al ₂ O ₃ ; and * MgAl ₂ O ₄	70
Figure 3.3 HAADF images and elemental maps: (a & b) Ni/Al ₂ O ₃ ; (c-f) La-Ni/Al ₂ O ₃	71
Figure 3.4 In situ plasma-DRIFTS spectra of CO ₂ activation at 200 °C. (a) Ni/Al ₂ O ₃ : (a1) 30 min treatment with CO ₂ /He (9 vol%, 110 mL/min), (a2) 30 min plasma treatment with CO ₂ /He, and (a3) plasma halt under He flow. (b) La- Ni/Al ₂ O ₃ : (b1) 40 min treatment with CO ₂ /He, (b2) 30 min plasma treatment with CO ₂ /He, and (b3) plasma halt under CO ₂ /He flow. (c) shows the vibrationally excited CO ₂ -enhanced mechanism of carbonate formation accompanied by magnified spectra (c1 and c2).....	72
Figure 3.5 CO ₂ -TPD patterns of (A) La-Ni/Al ₂ O ₃ and (B) Ni/Al ₂ O ₃ after 500 °C treatment: (a) thermally activated CO ₂ and (b) plasma-activated CO ₂ . The CO ₂ flow rate was 500 mL/min at 10 kPa. The heating rate was 10 °C/min.	77
Figure 3.6 DRIFTS spectra for CO ₂ /CH ₄ /He (8.3 vol%, 120 mL/min) activation over La-Ni/Al ₂ O ₃ at 200 °C in plasma-DRIFTS cell: (a) plasma-off; (b) plasma-on.....	78
Figure 3.7 In situ DRIFTS spectra of CH ₄ flows to carbonate-containing La-Ni/Al ₂ O ₃ at 600 °C	

in high-temperature cell (plasma-off). 1 min: CO ₂ /He=14 vol %, 70 mL/min; 2-7 min: CH ₄ /He=14 vol %, 70 mL/min; 8 min: He=60 mL/min.....	79
Figure 3.8 Plasma enhanced mechanism over La-Ni/Al ₂ O ₃ . Plasma induced reaction pathways (R3.1) is defined in section 3.5.1.....	82
Figure 3.9 Transmittance (I) and absorbance (II) spectrum of (a) La-Ni/Al ₂ O ₃ and (b) La-NiO/Al ₂ O ₃ under He flow (100 mL/min) at 600 °C in high-temperature cell.	84
Figure 3.10 DRIFT spectra of oxidation-reduction behavior on La-Ni/Al ₂ O ₃ at 600 °C in high-temperature cell: 1 min: oxidized catalyst with CO ₂ /He (9 vol.%, 110 mL/min) treatment; 5-15 min: reduced catalyst with H ₂ /He (9 vol.%, 110 mL/min) treatment; 30 min: re-oxidized catalyst with CO ₂ /He (9 vol.%, 110 mL/min) treatment.	85
Figure 4.1 Schematic diagram of PB-DBD reactor. Inset pictures show DBD generated by 12 kHz high-voltage power source (Logy Electric) and a thermo-image of the packed-bed.....	95
Figure 4.2 Voltage and current waveforms of packed-bed DBD: (a) 12 kHz and (b) 100 kHz. CH ₄ fraction was 0.5, and power was 85 W.	96
Figure 4.3 Time dependent change in gas composition and catalyst temperature. Φ = CH ₄ /CO ₂ ratio (= 0.5, 0.6, 0.7, 0.8, 0.9, 1.0, 1.1, 1.2, 1.3, 1.5). f = 12 kHz. Other conditions: see Table 4.1 (a).....	99
Figure 4.4 Conversion and selectivity at fixed catalyst temperature (600°C). Input power was also kept unchanged: see Table 4.1 (a) for experimental conditions. (a) CH ₄ conversion; (b) CO ₂ conversion; (c) H ₂ selectivity; (d) CO and coke selectivity. ● Thermal catalysis; ■ Plasma catalysis (12 kHz); ▲ Plasma catalysis (100 kHz).	100
Figure 4.5 Lissajous plot (CH ₄ fraction = 0.44, P_L = 90 W, catalyst temperature = 600 °C). Green curve: 12 kHz DBD; Red curve: 100 kHz DBD.....	103

Figure 4.6 The relationship between P_M and P_L . □ 100 kHz Empty-DBD; ■ 100 kHz PB-DBD; ○ 12 kHz Empty-DBD; ● 12 kHz PB-DBD. Conditions: Table 4.1 (b).	103
Figure 4.7 Power-determining parameters (Eq 4.13) v.s. Initial CH_4 fraction. ● 12 kHz PB-DBD; ■ 100 kHz PB-DB. Conditions: Table 4.1 (a).	104
Figure 4.8 Power-determining parameters (Eq 4.13) v.s. Applied voltage at fixed CH_4/CO_2 ratio. ○ 12 kHz Empty-DBD; ● 12 kHz PB-DBD; □ 100 kHz Empty-DBD; ■ 100 kHz PB-DBD. Conditions: Table 4.1 (b).	107
Figure 4.9 Electron collision rate coefficients estimated by BOLSIG+ (version 03/2016) at $CH_4/CO_2 = 1$ and 873 K. Momentum transfer and electron attachment are not shown. See Table 4.3 for elementary reactions.	110
Figure 5.1 Thermal images of catalyst bed in thermal reforming, 12 kHz and 100 kHz DBD hybrid reforming. Average catalyst temperature = 600 °C; Input power in 12 kHz and 100 kHz DBD is 90 W.	123
Figure 5.2 Reaction order in thermal reaction for CH_4 (α) and CO_2 (β), respectively. A hollow symbol represents stoichiometric condition ($CH_4/CO_2 = 1$).	125
Figure 5.3 Modified reaction orders: (a) α' for CH_4 and (b) β' for CO_2 . Catalyst temperature was fixed at 600 °C for all cases. $SEI = 1.37$ eV/molecules for 12 kHz and 100 kHz DBD hybrid reaction. Total flow rate = 1,000 cm^3/min (STP); GHSV = 5144 h^{-1} (STP); Pressure = 5 kPa. Δ represents CH_4 rich condition.	128
Figure 5.4 Arrhenius plot for thermal (●), mixed (■), and plasma catalysis (▲). The deviation due to the reverse reaction is highlighted by the shaded area.	132
Figure 5.5 Reaction coordinate for dissociative CH_4 chemisorption on metal surface. Solid curve; ground state CH_4 , Dotted curves; vibrationally excited CH_4 with different efficacy.	136

Figure 5.6 Activation energy of vibrationally excited CH ₄ reacting over Ni [45], Pt [34, 49], and Ir [50] surfaces. <i>A–B</i> ; this work, <i>C–E</i> ; ν_1 and ν_3 on Ni, <i>F–I</i> ; overtone on Ni, <i>J–L</i> ; other metal surface (Pt, Ir).	138
Figure 5.7 Arrhenius plot: (a) <i>SEI</i> = 2.0, <i>Run D</i> (Red circle), (b) <i>SEI</i> = 2.0, <i>Run E</i> (Red circle). <i>Run A</i> : Blue square (12 kHz, <i>SEI</i> = 1.37 eV/molecule), <i>Run B</i> : Green triangle (100 kHz, <i>SEI</i> = 1.37 eV/molecule) in all Figures. The number in parenthesis indicates CH ₄ conversion (%) for Red circle. The deviation due to reverse reaction is highlighted by the shades.	139
Figure 5.8 Streamer discharges on Ag/Al ₂ O ₃ catalyst pellets in air generated by nanosecond high-voltage to the needle electrode [52] (room temperature and atmospheric pressure). The image shows 50 times accumulation of 10 ns exposure imaging, showing multiple streamers (<i>n₁–n₅</i>).....	141

The list of achievement

Peer-reviewed journal articles

1. **Zunrong Sheng**, Hyun-Ha Kim, Shuiliang Yao, Tomohiro Nozaki, Plasma-chemical promotion of catalysis for CH₄ dry reforming: unveiling plasma-enabled reaction mechanisms. *Physical Chemistry Chemical Physics*, in press, DOI: 10.1039/d0cp03127e.
2. **Zunrong Sheng**, Yoshiki Watanabe, Hyun-Ha Kim, Shuiliang Yao, Tomohiro Nozaki, Plasma-enabled mode-selective activation of CH₄ for dry reforming: First touch on the kinetic analysis. *Chemical Engineering Journal*, 2020, 399: 125751, DOI: 10.1016/j.cej.2020.125751.
3. Adrianto Dimas, **Zunrong Sheng**, Tomohiro Nozaki, Mechanistic study on nonthermal plasma conversion of CO₂. *International Journal of Plasma Environmental Science and Technology*, 2020, 14: e01003 (9pp), DOI: 10.34343/ijpest.2020.14.e01003.
4. **Zunrong Sheng**, Kenta Sakata, Yoshiki Watanabe, Tomohiro Nozaki, Factors determining synergism in plasma catalysis of biogas at reduced pressure. *Journal of Physics D: Applied Physics*, 2019, 52(41): 414002, DOI: 10.1088/1361-6463/ab2d36.
5. Kenta Sakata, Seigo Kamashima, **Zunrong Sheng**, Yoshiki Watanabe, Tomohiro Nozaki, *Journal the Institute of Electrostatics Japan*, 2019, 43 (1): 2-7.
6. **Zunrong Sheng**, Seigo Kamashima, Shuiliang Yao, Tomohiro Nozaki, Oxidation behavior of Ni/Al₂O₃ catalyst in nonthermal plasma-enabled catalysis. *Journal of Physics D: Applied Physics*, 2018, 51(44): 445205, DOI: 10.1088/1361-6463/aae17d.

Book chapter

1. Tomohiro Nozaki, Seigo Kamashima, **Zunrong Sheng**, Keishiro Tamura, Takumi Yamazaki, Plasma-catalytic conversion of methane in *Plasma Catalysis: Fundamentals and*

Applications, Tu X, Whitehead J C, Nozaki T, Eds., Springer International Publishing, Cham, 2019, pp 231-269, DOI: 10.1007/978-3-030-05189-1.

2. **Zunrong Sheng**, Seigo Kamashima, Kenta Sakata, Tomohiro Nozaki, Plasma-enabled dry methane reforming in Plasma Chemistry and Gas Conversion; Britum N, Silva T, Eds., IntechOpen, London, 2018, pp 37-57, DOI: 10.5772/intechopen.80523.

Award

1. Best Student Presentation Award, The 7th East Asia Joint Symposium on Plasma and Electrostatics technologies for Environmental Applications (EAPETEA-7) (2019.11)
2. Best Presentation Award, 13th Japan-Korea-China Student Symposium (2019.5)
3. The Institute of Electrostatics Japan: HRSB Award (2018.11)
4. Best Student Presentation Award, The 6th East Asia Joint Symposium on Plasma and Electrostatics technologies for Environmental Applications (EAPETEA-6) (2018.11)
5. The Best Presentation Award, 12th Japan-Korea-China Student Symposium (2018.3)
6. China Scholarship Council (CSC) scholarship (2017.9~2020.9)

Chapter 1: Introduction

This chapter is partly adapted from the following publications in section 1.4.1 and 1.5.1:

- (1) Zunrong Sheng, Seigo Kameshima, Kenta Sakata and Tomohiro Nozaki, Plasma-enabled dry methane reforming in Plasma Chemistry and Gas Conversion, IntechOpen, 2018, DOI: 10.5772/intechopen.80523.
- (2) Zunrong Sheng, Yoshiki Watanabe, Hyun-Ha Kim, Shuiliang Yao, Tomohiro Nozaki, Chemical Engineering Journal 399 (2020) 125751, DOI: 10.1016/j.cej.2020.125751.

1.1 Overview

The catalysis dominates about 80% of industrial processes nowadays [1], and the research of catalysis has become a hot issue. The investigation of new catalyst and new catalytic reaction /technology are two technical routes to achieve large-scale industrial upgrading and low-carbon scenario. Since Devins *et al* firstly reported that the plasma-catalysis with DC discharge and platinum catalyst for hydrazine synthesis by ammonia in 1954 [2], the emerging “plasma catalysis” technology opens perspectives to meet the requirements of environmental cleanup, hydrocarbon reforming, and fuel synthesis [3]. The research articles about “plasma catalysis” has a rapidly increased rate within nearly three decades, and related research is still active nowadays [4]. The plasma catalysis combines heterogeneous catalysis and nonthermal plasma, where the plasma-induced reactive species and catalyst create unique synergism for catalytic process, showing thermodynamic and kinetic advantages over the conventional thermal catalysis.

The productivity of chemical products is always limited by the slowest reaction step in chemical industry. For example, the catalyst deactivation is the main barrier for many chemical

processes [5]. Plasma could achieve reaction enhancement and create alternative reaction pathways by electric energy input, which is favorable for slowest reaction pathway to improve productivity [6]. Major greenhouse gases, or renewable biogas, to the hydrogen-rich chemical building block is possible via plasma-enhanced catalytic reaction. Moreover, chemical industry accompanied by plasma is an emerging “power-to-chemical” technology, which provides unique electro-chemical conversion pathways. The electric energy is widely available from fluctuating power from photovoltaics, wind power, as well as hydro energy to reduce the overall energy cost [7]. The switch of chemical reaction becomes more flexible since the plasma features rapid start-up and shut-down compared with conventional thermal process (e.g. heating by feedstocks). From this macroscopic perspective, the plasma catalysis seems to be a new catalytic technology in the chemical industry. Nonthermal plasma-assisted C1 chemistry enables renewable-to-chemical energy conversion, which provides an alternative and viable solution for the efficient renewable energy storage and transportation pathways.

From a microscopic perspective, a heterogeneous reaction always includes several reaction pathways, where the slowest reaction pathway controls the overall reaction rate, which is called rate determining step (RDS), e.g. the CH₄ dissociative chemisorption on Ni catalyst in methane dry reforming [8, 9]. The electron energy transfer by plasma could induce the ionization, dissociation, and excitation by the collision between electron and neutral gas molecule. Contributed by the synergistic effect, plasma is expected to accelerate the RDS to improve the overall reaction rate by energetic electron and reactive species, e.g., radicals, excited species, and ions *etc.* The generated species characterizes high reactive chemical property to enhance surface reaction with catalyst in the heterogeneous catalysis [10, 11]. The surface of metallic nanocrystal of catalyst plays a critical role for incident gas molecule adsorption and activation in heterogeneous catalysis, e.g. CH₄ adsorption at Ni (111) [12]. For plasma involved catalysis, the molecule in the gas phase is impacted by electron in advance,

and activation barrier for chemisorption is further decreased [11]. In this case, the plasma contributes to breaking chemical bonds for accelerating the reaction. Based on well-established heterogeneous catalysis, plasma catalysis could be investigated based on the Langmuir-Hinshelwood [13] or Eley-Rideal [14] mechanism.

1.2 Methane dry reforming

1.2.1 Opportunities

To mitigate the emerging global warming issue, the Paris Agreement and Kyoto Protocol set the target to limit the greenhouse gases emission to participant countries [15]. The emission of CO₂, primarily from thermal power plants and industrial activities, contributes the main source for greenhouse emission [16]. The CO₂ atmospheric concentration has increased to 409 ppm [17] in 2017 with approximately 2 ppm increase rate [18], primarily from emissions of the combustion of fossil fuels (90%) and cement production (10%) [19]. As for another main greenhouse gas, the concentration of CH₄ has increased to 1800 ppb nowadays [20, 21], with a 23 times global warming potential than that of CO₂ [22]. Methane dry reforming (MDR, R1.1) was firstly invented by Fisher and Tropsch in 1928 for CO₂ and CH₄ conversion simultaneously [23], and becomes an important technology for carbon source capture and utilization. MDR has received much attention nowadays, showing significant benefits to reduce greenhouse gases emission and produce value-added fuels and chemicals.



Biogas from waste and residues plays a critical role in the energy future [24], which mainly consists 55-70 vol% CH₄ and 30-45 vol% CO₂ [25]. Aiming to energy grade upgrade, MDR is a promising method for biogas upgrade to syngas, attributing to accessible and abundant feedstocks [26]. China is the world largest biogas producer, where the production of

biogas was above 8 Mega-Ton in 2013 [13], with a continued growth trend in following year as expected [27]. Biogas could be effectively utilized by MDR process without CO₂ separation processed, considering the practical reaction stoichiometry ($\text{CH}_4/\text{CO}_2 = 1$) [28]. Moreover, the product syngas is a key chemical feedstock for Fischer-Tropsch synthesis towards high-value products [29], including lower olefins and aromatics (C₂-C₄), gasoline (C₅-C₁₁), diesel fuel (C₁₀-C₂₀) and jet fuel (C₈-C₁₆) [30, 31]. The H₂/CO ratio from MDR is more suitable for a Fischer-Tropsch synthesis than other methane reforming reactions [32-34].

1.2.2 Challenges

The application of MDR is limited by economic benefit since it is an endothermic reaction that high thermal energy is necessary required to drive this reaction (cf. section 1.4.1). In conventional MDR, the catalyst is crucial to reduce the operating temperature and accelerate reaction, which has been investigated widely based on two categories: noble metal and transition metal. The noble metals, including Pd [35], Pt [35, 36], Ru [37-39], Rh [35, 40-43] and Ir [44], show good activities in MDR. Ref. [45] reported that noble metals show good reforming efficiency per loading weight. However, the high-cost limits the development of noble metal in the industry. Alternatively, some transition metal catalyst also shows good performance in MDR, including Ni [46-50], Co [51-53], and Zr [54]. References [55, 56] reported that Ni-based catalyst led to a high CH₄ conversion (80~90 %). The trade-off should be pointed out that due to high activity of CH₄ activation, Ni-based catalyst is inevitably prone to carbon formation, while noble metal catalysts may feature less carbon formation but less activity. Figure 1.1 (a) represents a typical phase diagram for Ni catalyst for equilibrium of the catalyst phase (Ni and NiO), coke phase (NiC and C) and gas phase (CH₄, CO₂, CO, H₂ and H₂O) at 900 K and 1 atm [57]. Three boundary lines separate the plot as three parts, where upper two boundaries are almost overlapped. For the MDR at normal condition of $\text{CH}_4/\text{CO}_2=1$,

it locates in the $\text{Ni}_x\text{C}+\text{C}$ region (red point in Figure 1.1 (a)), which means the coke formation is inevitable. Figure 1.1 (b) schematically presents the carbon deposition mechanism [58], where the CH_4 dehydrogenation leads to carbon precipitation, then nickel carbide (NiC) is generated. Figure 1.1 (c) shows carbon distribution over $\text{Ni}/\text{Al}_2\text{O}_3$ pellet cross-section after reforming where internal micropores shows the highest carbon level (as red color) [59]. Indeed, the deactivation of Ni catalyst limits its application and becomes one challenge for cyclic durability in industry. The researchers endeavor to suppress the coke by modification of catalyst. The most common modified methods are adding bimetallic catalyst [60, 61] and improvement of dispersion of active sites [60].

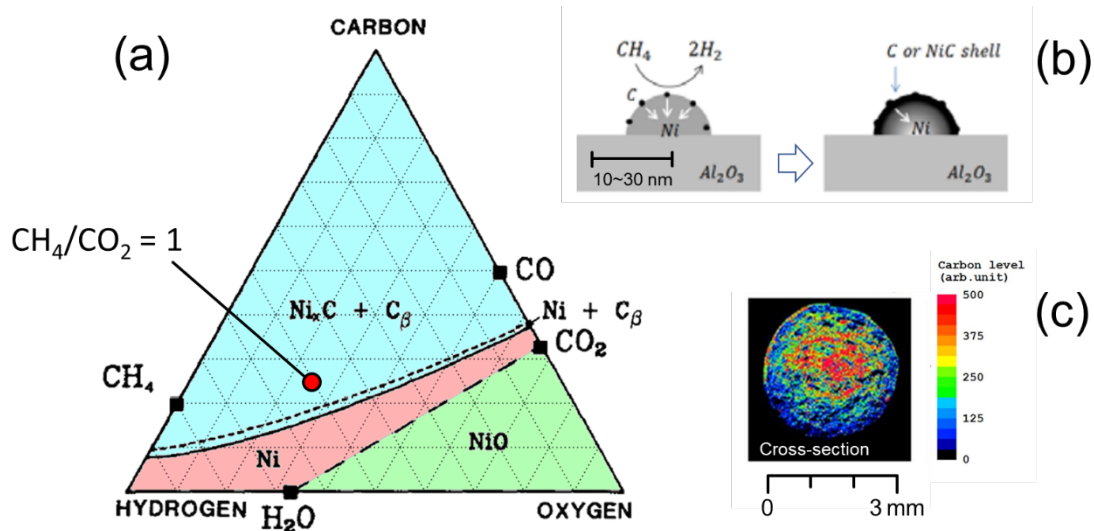


Figure 1.1 Coke formation in Ni catalyst: (a) Ni-C-H-O phase diagram (900 K and 1 atm) [57]. (b) the NiC formation mechanism [58], (c) carbon distribution in $\text{Ni}/\text{Al}_2\text{O}_3$ pellet after reforming [59].

1.3 Nonthermal plasma

Plasma, referred as “fourth state of matter”, which is first introduced by Irving Langmuir at 1927 [62]. The electron is accelerated by electrical field since it has much lighter mass than neutral gas molecule. Then the electron with high kinetic energy could induce the ionization,

dissociation and excitation. Expect for the charged particles (e.g. electron, and positive and negative ions), neutral species (e.g. molecules, atoms, radicals and excited species *etc.*) also play important roles in plasma application. Kim *et al* have summarized the time scales of plasma species compared with that of chemical reaction, which is schematically depicted in Figure 1.2 [63]. In the plasma, the reactive species induced by electron is in nanosecond scale, while the chemical reactions over catalyst surface is in a longer time scale (microsecond to millisecond and longer), suggesting that the rate determining step is the surface reaction rather than plasma involved reaction. For example, the OH radical only has a 20-100 μs life time [64, 65]. Moreover, only the plasma species in the thin layer ($\sim 50 \mu\text{m}$ [66]) above catalyst surface could contribute to the plasma-catalyst interaction. Generally, the mean free path of plasma species is typically less than 100 nm, and the collision time is shorter than 1 ns [67]. The synergism between plasma and catalyst becomes a hot topic to understand plasma catalysis, which has been introduced in some review articles [68-71] based on the effect of plasma on catalyst, and the effect of catalyst on plasma.

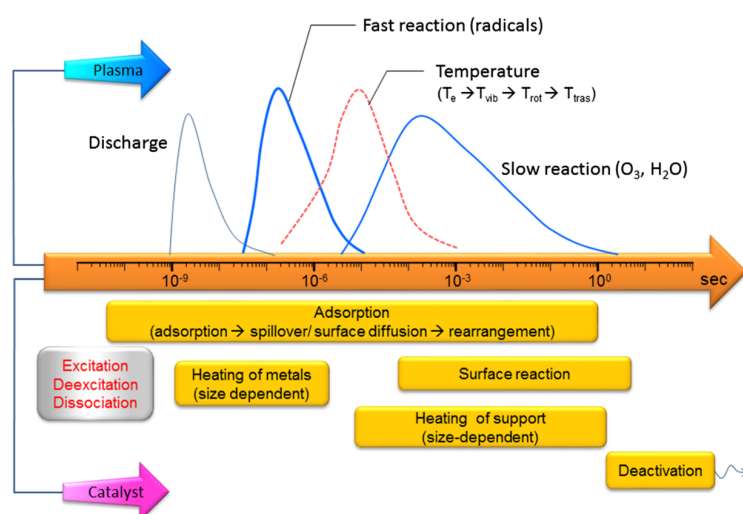


Figure 1.2 The time-scales of plasma and catalytic reaction [63].

1.3.1 Classification of plasma

According to the temperature of heavy particle, the plasma could be generally classified as thermal plasma and nonthermal plasma. In thermal plasma, electron density is very high (10^{21} - 10^{26} m⁻³ [72]) that the joule heating plays the key role in the equilibrium between electron and heavy particles. The temperature of electron and heavy particles are 10^4 ~ 10^5 and 10^3 ~ 10^4 °C respectively [45, 69]. Thermal plasma is favor for thermal treatment application, e.g. coating, welding, cutting [73] *etc.* Thermal arc plasma have been industrially applied in Hüls process for CH₄ coupling [74]. Obviously, it is impractical for heterogeneous catalysis since that the plasma will melt the packed catalyst so that some works reported non-packed thermal plasma could assist MDR [75].

In Figure 1.3, Tendero *et al* classified various discharge types based on temperature and density of electron [72], where the atmospheric pressure plasma is distinguished as low-pressure nonthermal plasma and high-temperature thermal plasma. Generally, glow discharge, microwave torch and dielectric barrier discharge are applied in low temperature process, while arc plasma is more suitable for high temperature process. Interestingly, few plasma sources are plotted in low electron temperature region (lower than 1 eV, red region in Figure 1.3), indicating that this unexplored regimes has a potential development for plasma catalysis, biomaterials treatment and atomic layer process [76].

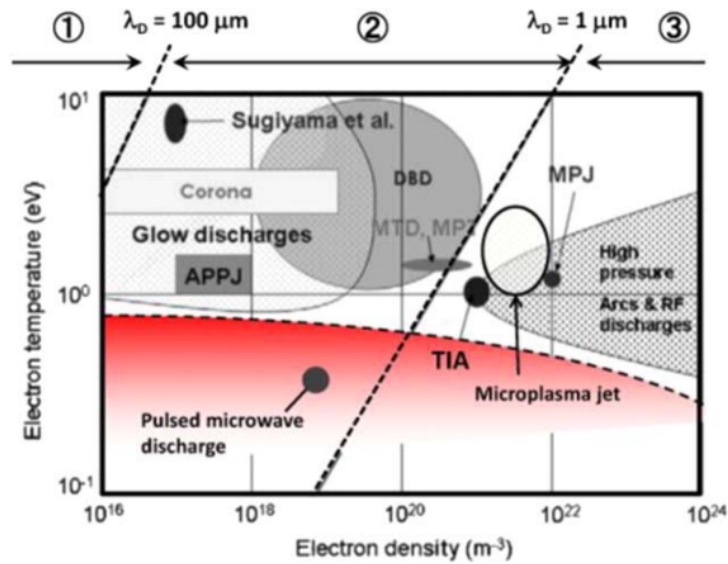


Figure 1.3 Classification of atmospheric pressure plasma sources [72]. (Color region is modified by Ref.[76]). APPJ: atmospheric pressure plasma jet; DBD: dielectric barrier discharge; MPJ: microwave plasma jet; MPT: microwave plasma torch; MTD: microwave torch discharge; TIA: plasma torch with axial plasma injection.

In nonthermal plasma, electron density is low ($<10^{19} \text{ m}^{-3}$ [72]). The heavy particles have much lower temperature ($10^2 \sim 10^3 \text{ }^\circ\text{C}$) than that of electron ($10^4 \sim 10^5 \text{ }^\circ\text{C}$) due to the few kinetic energy transfer. The thermalized electron follows the Maxwell-Boltzmann velocity distribution, whereas the velocity of gas molecule does not follow it [77]. Such inadequate transfer of momentum between electron and gas molecule [78] leads a fact that the inert gas molecule could be converted into “excited” or “reactive” state in nonthermal plasma even at room temperature. The same excitation state usually exists in arc discharge or flame at very high temperature [67]. Therefore, the nonthermal plasma also called non-equilibrium plasma. This section specially summarizes several nonthermal plasma discharge which are usually employed in gas treatment process, including dielectric barrier discharge, gliding arc, corona discharge, microwave discharge and radio frequency discharge.

1.3.2 Dielectric barrier discharge (DBD)

Dielectric barrier discharge (DBD) is the most successful atmospheric pressure nonthermal plasma sources in industry applications [79], e.g., ozone synthesis [80, 81], CO₂ conversion [82-84], methane reforming [8, 58, 85], and N₂ fixation [86, 87]. As Figure 1.4 depicts, DBD reactor normally consists of a high voltage electrode and a ground electrode, and dielectric barrier between two electrodes. The reactor plays the role of dielectric barrier, e.g., coaxial quartz reactor [88, 89]. When the catalyst is packed in DBD reactor (Figure 1.4), the charge is transferred through catalyst and quartz tube. DBD is characterized as a swarm of filamentary micro-discharges (known as streamers) with nanosecond duration (1–10 ns) [79]. Because the streamer has a nature of propagation along the interface between two adjacent dielectric materials, namely the catalyst pellet and the gas interface, excited species produced by DBD is transferred to the catalyst surface efficiently. The Figure 1.5 shows the surface streamers propagating over the surface of Al₂O₃ by ICCD (Intensified charge-coupled device) camera [90]. Table 1.1 summarizes the characteristics of DBD filament with air at atmospheric pressure [91].

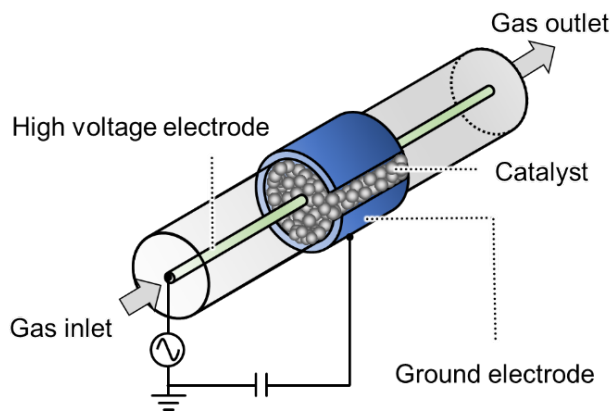


Figure 1.4 Schematic diagram of catalyst-packed DBD reactor.

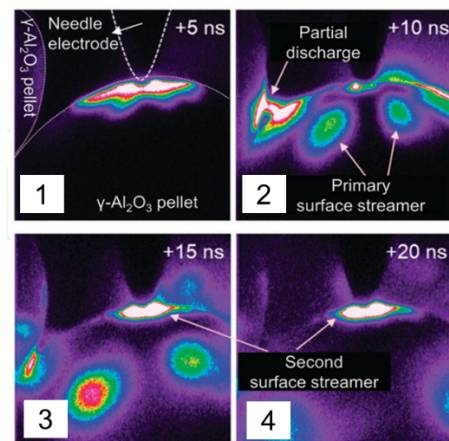


Figure 1.5 Surface streamers propagating over the surface of Al₂O₃ by ICCD camera [90].

Table 1.1 Characteristics of DBD filament with air at atmospheric pressure [91].

Duration	Filament	Peak	Current	Total	Electron	Mean	Filament
(s)	radius	current	density	charge	density	electron	temperature
	(m)	(A)	(A m ⁻²)	(C)	(m ⁻³)	energy	
						(eV)	
10 ⁻⁹ -10 ⁻⁸	~10 ⁻⁴	0.1	10 ⁶ -10 ⁷	10 ⁻¹⁰ -10 ⁻⁹	10 ²⁰ -10 ²¹	1-10	≈ gas temperature

The heat generated by DBD is transferred directly to the catalysts, overall energy transfer from nonthermal plasma to the catalyst bed is efficient. Different from corona discharge (section 1.3.3), the DBD could produce more homogenous discharge with low energy consumption [92]. The electrical equivalent circuits of DBD reactor is summarized by Kim *et al* [66], which are shown in Figure 1.6. As for empty-DBD (non-catalyst packed) in Figure 1.6 (a), when the voltage of the gap (gas) reaches the gas breakdown voltage (closed to the discharge sustain voltage), the gas turns to work as a bipolar Zener diode or a time-based resistance instead of a capacitor [79, 93]. As for the packed-bed DBD with catalyst (Figure 1.6 (b)), the unit circuit of gap is equivalent to connection between capacitance of gas and catalyst, and resistances of them in series. The Lissajous plot is normally employed to investigate the discharge behavior, i.e. time- and space-averaged properties of *streamer swarm*, providing plasma sustain voltage (U_{sus}) and mean discharge current ($I_{\text{p-p}}$) [79, 94], which will be discussed in Chapter 4. Generally, DBD has some advantages: the arc discharge could be avoided; the collision probability between heavy molecule and electron may be enhanced [81]; the scale-up is easily to be achieved by the simple structure and low-operational cost.

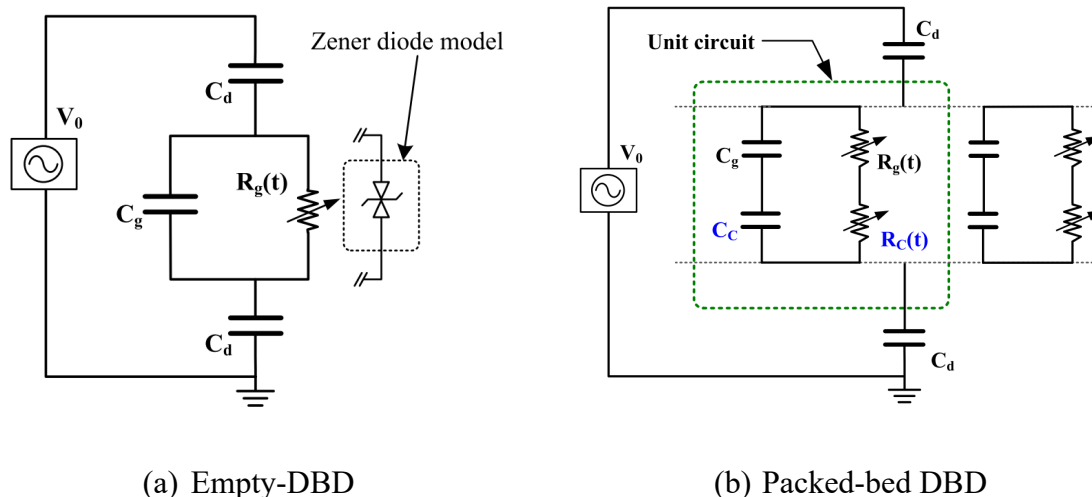
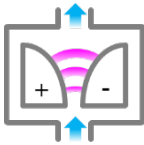
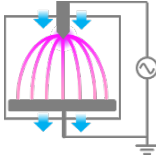


Figure 1.6 Equivalent electrical circuit of DBD reactor: (a) empty-DBD and (b) packed-bed DBD. The subscript d, g, and c is abbreviation for dielectric material (quartz tube), gas, and catalyst respectively.

1.3.3 Other nonthermal plasma

The gliding arc is normally equipped with two blade-shape electrodes with diverging discharge gap [95]. The schematic structure and the characteristics are summarized in Table 1.2. The arc is ignited at the shortest gap (several mm) and glides with widening gap until sustaining stops, then the new arc is formed within 10 millisecond [95]. Interesting, the arc plasma could be classified as an intermediate plasma that the bottom part works as thermal plasma, and gradually evolves into nonthermal plasma with power decrease. There are some upgraded gliding arc structures with 3D configuration, e.g., reverse vortex flow "tornado" type (3D) [96, 97], and rotating arc type [98, 99]. However, the filling catalyst is challenging in this configuration [67]. The gliding arc plasma is widely applied in gas treatment process, e.g., cracking of n-dodecane [100], reforming of mixed naphthalene [101] and toluene [101, 102], CH₄ reforming [103-105]. Besides, it is also reported in applications of decomposition of water pollutants [106], and materials synthesis fields e.g. carbon nanotubes [107], boron nitride nanotubes [108], *etc.*

Table 1.2 Schematic structure and characteristics of gliding arc and corona discharge [109].

	Schematic structure	Electron energy (eV)	Electron density (cm ⁻³)	Current (A)	Gas temperature (K)	Breakdown voltage (kV)
Gliding arc discharge		1.4-2.1	10 ¹⁴ - 10 ¹⁵	0.1-50	1000-3000	0.5-4
Corona discharge		ca. 5	10 ⁹ -10 ¹³	ca. 10 ⁻⁵	ca. 400	10-50

The corona discharge works in needle-to-plate mode (as the structure in Table 1.2) at atmospheric or high pressure, creating a crown streamer micro discharge [72]. The streamer produced in narrow channels contributes to gas dissociation or ionization by energetic electron [95] in non-uniform electric field [92]. The high electric field is usually located around one of electrode and electron moves by drift of charge particles in low electric field [110]. It could be classified as positive corona, negative corona and pulsed streamer corona [95]. The need-to-plate discharge is flexible in discharge gap change (10 cm and more [92]), which is favorable for material treatment and gas processing in laboratory studies [95, 111]. For the large scale application, the popular upgraded structure is the wire-cylinder and saw-blade [112, 113]. In addition, the pulsed corona discharge could work with large flowrate [114, 115], which was employed in NO_x removal [114, 116]. Recently, Gao *et al* reported a similar non-packed needle-to-plate discharge for CH₄ pyrolysis where the highest conversion of CH₄ and H₂ yield were 91.2% and 38.4% respectively with an energy conversion efficiency of 44.3% [117].

Radio-frequency (RF) plasma is driven by high-frequency electromagnetic fields within 0.1-100 MHz [95]. The typical frequency in Ref. [118] is reported as 14 MHz. The capacitive

coupling (CCPs) RF plasma is driven by oscillating magnetic field to generate non-thermal plasma. The inductive coupling (ICPs) RF plasma is driven by oscillating electric field. The simplified structure of RF plasma reactor for surface treatment is depicted in Figure 1.7 (a). The plasma chamber is manufactured by stainless steel or quartz, which is surrounded by RF coils or electrodes [70, 119]. The CCPs is normally work in low-pressure ($1-10^3$ Pa) to sustain the discharge otherwise the arc discharge will generate at higher pressure. The electrode-less configuration of RF supplies operational feasibility for the combination plasma with catalyst for gas treatment e.g., NO_x removal [120], ammonia synthesis [121], CH_4 reforming [122, 123], *etc.* The ICPs is usually employed to generate ions and excited species for material analysis, e.g., ICPs coupled mass spectrometry (ICP-MS) and ICPs coupled atomic emission spectroscopy (ICP-AES). These setups often require complex power supplies to deliver optimal power to the working gas [70].



Figure 1.7 Schematic structure of high frequency plasma: (a) RF plasma and (b) MW plasma.

Microwave (MW) plasma is well-known experimental technique to generate nonthermal plasma discharge, which directs microwaves to discharge zone from plasma source with an applicator (Figure 1.7 (b)). The operational frequency of MW is in the range of 300 MHz-10 GHz [95], which is much higher than that of RF plasma. The MW plasma also has the

characteristics of electrode-less configuration, which is feasible to pack catalyst in the discharge area for gas treatment. The MW plasma usually provides a higher energy efficiency (~40%) in CO₂ conversion than DBD (<15%) [124], which is contributed by the ladder-climbing CO₂ dissociation mechanism [125-127]. The thermal dissociation mechanism could be predominant in MW plasma [128]. However, the gas temperature in MW plasma is difficult to be controlled, which detracts energy efficiency by vibrational-to-translation (V-T) relaxation [124]. Except CO₂ dissociation, the MW reactors are also employed in the fields of waste decomposition [129, 130], CH₄ pyrolysis [131], and CH₄ reforming [132-134].

1.4 Thermodynamics

1.4.1 Thermodynamic analysis for low-temperature operation

MDR is categorized as uphill (endothermic) reaction where energy input (ΔH) is indispensable in order to satisfy the conservation of energy. Figure 1.8 shows the reaction enthalpy and Gibbs free energy of MDR with respect to temperature. According to the Eq 1.1, reaction enthalpy consists of two terms:

$$\Delta H = \Delta G + T\Delta S \quad \text{Eq 1.1}$$

The reaction does not occur spontaneously by the low-temperature thermal energy due to the large positive value of ΔG at low temperature. Figure 1.8 shows that at least 900 K is required to have a negative value of ΔG and all energy is supplied via high-temperature thermal energy. Such high-temperature heat is supplied by the combustion of initial feed that produces CO₂ as well as NO_x. Net CO₂ utilization is partly canceled unless combustion-generated CO₂ is utilized which is economically quite difficult. Moreover, heat transfer from the combustion gas flowing outside of the reactor to the catalyst bed governs the overall material throughput which is known as a *heat-transfer-limiting* regime. Because the heat transport property of a fixed bed reactor is poor, excessively high-temperature operation beyond thermodynamic limitation (i.e.

900 K) is necessary.

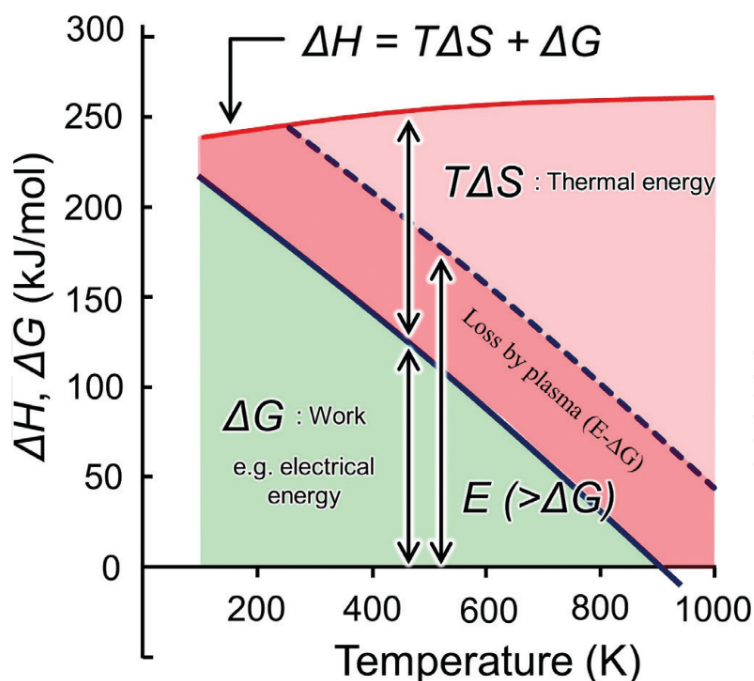


Figure 1.8 Energy diagram of methane dry reforming [135].

To overcome the aforementioned problem, low-temperature MDR is demanded, which is pursuing a new technology and potential use of nonthermal plasma is highlighted. Assume MDR is operated at a lower temperature than the thermodynamic limitation as schematically depicted in Figure 1.8. A part of the energy is supplied by a low-temperature thermal energy ($T\Delta S$), while the rest of energy is supplied by the electricity (ΔG) under the nonthermal plasma environment so that $T\Delta S + \Delta G$ satisfies reaction enthalpy (ΔH). Electrical energy is used to accelerate electrons; subsequently, the electron energy is transferred to the molecules to initiate MDR at much lower temperature than thermal catalysis. Electronic collision process is independent of reaction temperature if gas density does not change significantly. Meanwhile, a part of the electrical energy is converted to heat: electrical energy consumed by nonthermal plasma (E) is depicted in the dashed line in Figure 1.8: inevitably, E is greater than ΔG at a fixed temperature. Although heat generated by nonthermal plasma is considered as energy loss

(i.e. $E - \Delta G$), both excited species, as well as heat, are utilized via endothermic MDR, which enables efficient use of electrical energy without *heat-transfer-limitation*: electrification of reforming reaction, or chemical processes in general, has the greatest advantage that the energy transfer and the control is independent of temperature gradient.

Thermodynamic analysis implies that the temperature-benign and low-emission chemical processes are possible with the appropriate combination of nonthermal plasma and the heterogeneous catalysts. Figure 1.9 shows the conversion of CH_4 and CO_2 in MDR as a function of special energy input (SEI) operated at room temperature with different catalysts [136-145]. One common characteristic of these studies is the high SEI at a large input power or low gaseous hourly space velocity ($GHSV$).

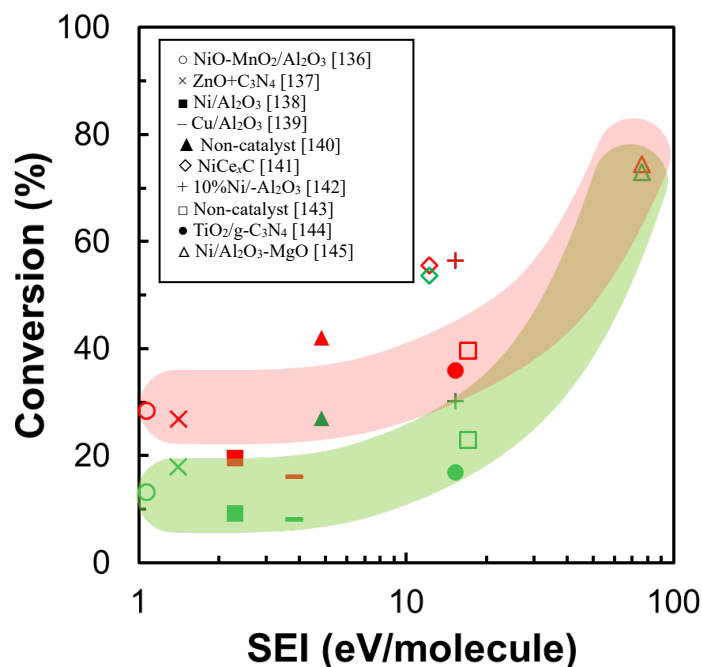


Figure 1.9 Conversion of CH_4 (red symbol) and CO_2 (green symbol) as a function of SEI at room temperature with different catalysts [136-145]. 1 eV/molecule \approx 4 kJ/L.

1.4.2 Thermodynamic equilibrium

Figure 1.10 represents the equilibrium conversion equilibrium composite of MDR as a

function of system temperature at 5 kPa by Gibbs free energy minimization. It should be pointed out that the depicted theoretical equilibrium is difficult to achieve in the industrial or laboratory application because the residence time is always short that the overall reaction rate is kinetically-controlled. The highlight of nonthermal plasma is to exceed this theoretical equilibrium by the electron energy input. Some studies have reported that the CH_4 and CO_2 conversion exceeded the equilibrium by large electron energy input with catalyst temperature of 150 ~ 400 °C [146-151].

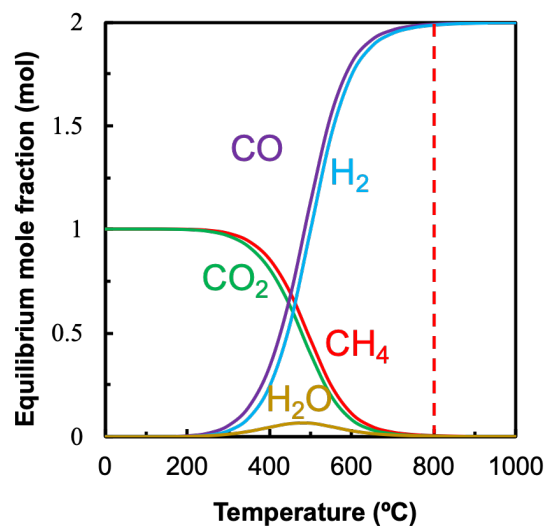


Figure 1.10 Thermodynamic equilibrium composite of MDR: initial input of CH_4 and CO_2 are 1 mol respectively; pressure = 5 kPa; coke formation is omitted.

On the other hand, the additional separation process is necessary since that the raw feedstocks (CH_4 and CO_2) are co-existed with syngas (CO and H_2) in the outlet when the temperature is lower than 800 °C as Figure 1.10 shown. Such separation of feedstocks from products may be driven by additional technologies of absorption, adsorption, and membrane separation [152], which decreases economic benefit inevitably. Then rest CH_4 and CO_2 backflows to the reactor with extra energy input, which decreases the energy efficiency of

overall system. Once the temperature exceeds 800 °C, above separation process is exempt. Therefore, plasma-assisted MDR operated at high-temperature is a potential way to enhance the CH₄ and CO₂ conversion as much as possible to avoid the unnecessary separation. In other word, although such plasma assisted MDR is still operated at high temperature rather than room temperature operation, the high CH₄ and CO₂ conversion towards complete conversion to the target product also shows a significant economic benefit.

1.5 Kinetic research

1.5.1 Power-law kinetics and activation energy

The interaction of multiple potential reactions involving energetic species, as well as the nonthermal behavior leads the kinetic study become difficult to be elucidated comprehensively in plasma catalysis [153]. As a simple and basic method, the power-law model is widely employed in heterogeneous catalysis to understand the underlying physicochemical mechanism by reaction order and activation energy. Figure 1.11 (a-i) shows the activation energy of methane dry reforming according to some Ni- and La-based catalysts. Except of some modified catalysts and reaction system with outstanding behavior, activation energy of CH₄ in thermal catalysis with the common metal-support catalyst is around 90 kJ/mol. Very few studies have been investigated about the power-law kinetics for plasma catalysis. Compared with thermal catalysts, plasma catalysis shows a much lower activation energy in Figure 1.11 (j) and (k). Molecular beam study revealed the vibrationally excited CH₄ enhances dissociative chemisorption over Ni clean surface [154, 155]. The investigation of mode selective reactivity shows a drastic decrease of the C-H activation energy barrier is possible via stretching vibration mode where the vibrational efficacy exceeds 100 % [11]. Similarly, vibrationally excited CO₂ is reported to enhance the surface reaction between adsorbed hydrogen in the Eley-Rideal mechanism [14, 156].

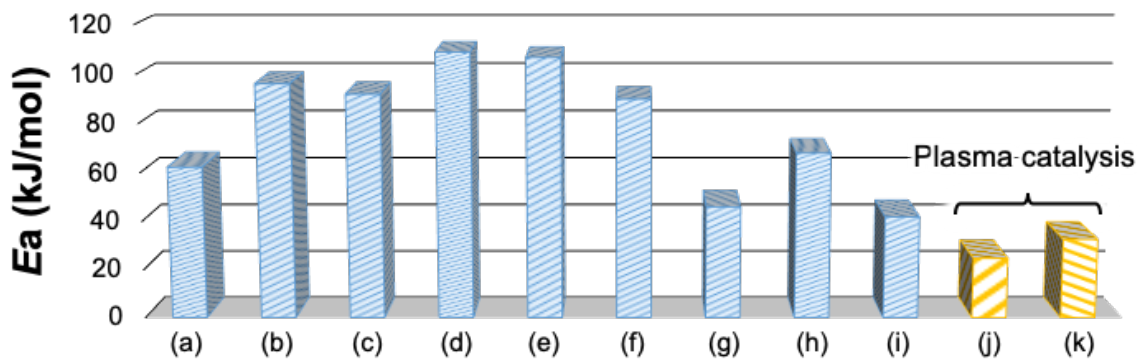


Figure 1.11 Activation energy (E_a) of methane dry reforming according to (a-i) thermal catalysis and (j-k) plasma catalysis over different catalyst: (a) Ni/SiO₂ [157]; (b) Ni/SiO₂ [158]; (c) Ni/MgO [158]; (d) Ni/TiO₂ [158]; (e) Ni/La/Al₂O₃ [159]; (f) Ni/CaO-Al₂O₃ [160]; (g) Ni-K/CeO₂-Al₂O₃ [161]; (h) LaNiO₃ [162]; (i) LaSrNiO₄ [163]; (j) Ni/La₂O₃@SiO₂ [164]; (k) Ni/La₂O₃-MgAl₂O₃ [153].

Kinetic model of plasma-assisted gas conversion chemistry have been studied in NO_x and VOC abatement [165, 166]. The power-law kinetic equation is modified by using specific energy input (SEI), assuming the reaction rate is proportional to the n^{th} power of SEI . Because plasma catalysis is operated at sufficiently low temperature where thermal reaction is not initiated. On the other hand, they observed temperature-dependent change of gas conversion behavior. Although the seeding radical species by DBD is proportional to the energy density (i.e. $\propto SEI^n$) and independent of temperature; subsequent reactions depend on the ambient temperature to some extent. Yan *et al* proposed the detailed model using both SEI and the temperature dependent rate equation for gas phase plasma conversion of VOC [113].

Similar approach has been reported in plasma catalysis of CH₄ and CO₂ reforming. Similar to previous work, the SEI was used as a key parameter. However, unlike VOC and NO_x treatment, catalyst temperature is higher than the light-off temperature (the lowest temperature limit where the catalytic reaction is onset), thereby a relationship between SEI and catalyst

temperature need to be clarified in a consistent manner. Zhu *et al* studied *SEI* in the range of 200 and 800 kJ/mol [167]. Comparing to the specific energy requirement (*SER*) of CH₄ and CO₂ reforming, there is a concern of significant plasma heating due to excessive energy input (*SEI* > *SER*). Moreover, temperature-dependent term is not included in the equation. Kim *et al* have studied both catalyst temperature and *SEI* [168]. Plasma heating seems to be avoided because *SEI* < *SER* was fulfilled. Meanwhile, gas conversion by plasma catalysis does not show temperature dependence, although thermal catalysis (plasma-off) exhibited clear dependence of catalyst temperature. They replaced the "RT" term by *SEI* and proposed non-Arrhenius model, showing the reaction rate is proportional to $e^{-\frac{E_{app}}{SEI}}$. The apparent activation energy (*E_{app}*) derived as small as < 20 kJ/mol. Direct comparison between these literatures is difficult due to a different formulation and assumption of the model. One common conclusion is the kinetic parameters of plasma catalysis can be evaluated by catalyst temperature and *SEI* basis.

1.5.2 Kinetics-related surface reactions

Working principle of catalyst is shown in Figure 1.12 (a), where blue curve presents that the energy barrier from reactant to product is high to overcome that reaction is impossible when catalyst is absent. Red curve in Figure 1.12 (a) schematically depicts the principle of heterogeneous reaction. The catalyst separates one reaction into several reaction elementary pathways (steps) towards energy barrier decrease [69]. The heterogeneous catalysis is normally explained by Langmuir-Hinshelwood (L-H) mechanism, mainly including adsorption, surface reaction, and desorption. The catalyst plays a role to “catch” the gas molecule from gas phase into the catalyst surface through the boundary layer. Different with gas phase collision between reagents directly to product (gas-phase reaction), catalyst supplies a platform for the trapped molecules to react with other trapped molecule towards products generation. The adsorption seems to be an essential prerequisite in conventional thermal catalysis [67], and the activity of

absorption is kinetically controlled by surface temperature of catalyst.

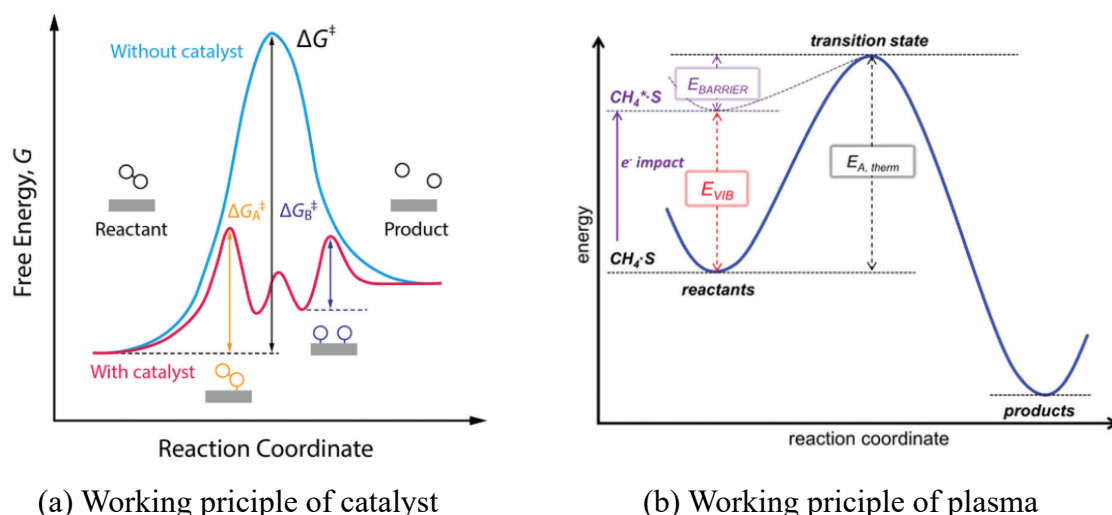


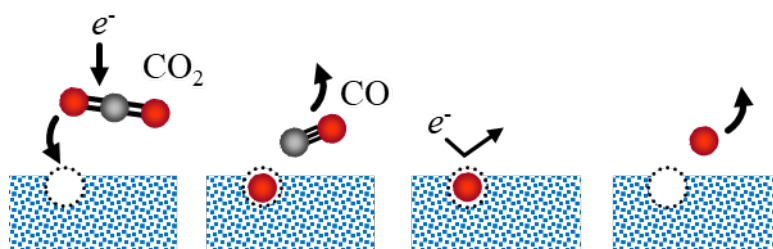
Figure 1.12 Reaction coordinate diagram for working principle of (a) catalyst [69] and (b) nonthermal plasma with vibrational excitation [169].

Some studies pointed out that nonthermal plasma could play an important role to reduce the activation barrier to enhance the surface adsorption/activation [13, 67, 68, 169-171]. The CH₄ dissociative chemisorption on nickel is considered to be the rate-determining step which controls the overall reaction rate. The CH₄ dissociative chemisorption on nickel which is schematically depicted in Figure 1.12 (b). In the thermal reaction, the ground state CH₄ molecule meets a high energy barrier ($E_{A, therm}$) to arrive the transition state for dissociative chemisorption on Ni, i.e., 0.52 eV on Ni (100) [172], 0.74 eV on Ni (111) [173]. In plasma-assisted reaction, a part of reaction barrier is impacted by vibrationally excited CH₄ (E_{VIB}) under the electron impact, contributing to a lower reaction barrier ($E_{BARRIER}$) than that for ground state CH₄. The related research about kinetic study of vibrationally excited CH₄ on Ni surfaces will be discussed in Chapter 5.

As for CO₂ uptake, two kinds of CO₂-driven oxygen are expected to supply oxygen species for surface reaction: lattice oxygen and adsorbed oxygen. As for the former, some

works reported that the electron-attached CO_2 molecule could be trapped into the oxygen vacancy on photocatalytic materials, e.g. BaTiO_3 , TiO_2 under plasma influence [174, 175], and dissociates to CO with a O^{2-} anion filling in the oxygen vacancy (Figure 1.13 (a)). The oxygen vacancy is regenerated by the impaction of electron colliding. However, surface reaction between derived adsorbed species from CH_4 (e.g. CH_3^* , CH_2^* , *etc.*) and lattice oxygen is still unclear. Based on the coke formation behavior (cf. Figure 1.1), we propose that lattice oxygen may contribute to coke suppression in Ni-based catalyst, which will be discussed in Chapter 2.

(a) Lattice oxygen



(b) Adsorbed oxygen

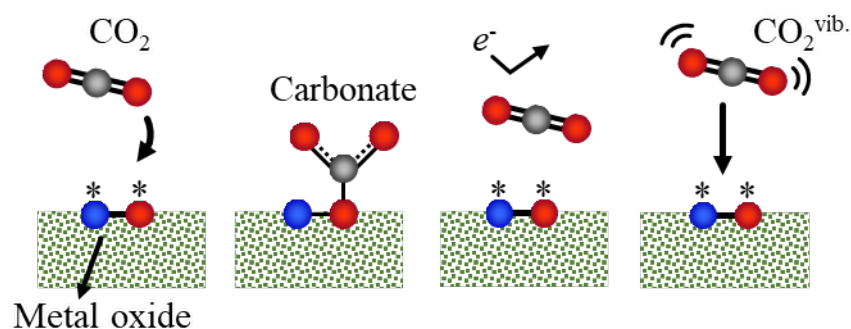


Figure 1.13 CO_2 -derived oxygen fixation: (a) lattice oxygen formation mechanism over photocatalytic material [176]; (b) adsorbed oxygen formation mechanism over basic material.

As for the CO_2 -derived adsorbed oxygen, basic site (e.g. lanthanum oxide) contributes an

anionic oxygen (O^{2-}) to adsorbed CO_2 for surface covalent carbonate species (CO_3^{2-}) formation (Figure 1.13 (b)). This adsorbed oxygen-obtained species may be more reactive than lattice oxygen in surface reaction with other adsorbed species. Some basic metallic oxides are reported as activate sites for carbonate formation, e.g., CaO [177], TiO_2 [178, 179], La_2O_3 [178, 180-184], ZrO_2 [185], CeO_2 [186], MgO [187]. However, the interaction between plasma-excited CO_2 and basic materials is still unclear (as Figure 1.13 (b) depicted), which becomes the main target for Chapter 3.

1.6 Scope of this thesis

This thesis presents the experimental study of nonthermal plasma-enabled methane dry reforming, aiming for providing deep insight into plasma-catalyst interfacial physicochemical phenomena. The DBD provides vibrationally excited species by low-energy electron impact. Two kinds of nickel-based catalysts were employed: non-lanthanum modified Ni/ Al_2O_3 in Chapter 2 and 3, and lanthanum modified Ni/ Al_2O_3 in Chapter 3, 4 and 5. The reason for employing two kinds of catalyst is to distinguish the contribution of lattice oxygen-contained species and adsorbed oxygen-contained species to reforming behaviors. The surface lattice oxygen-contained NiO formation behavior under DBD CO_2 treatment is related to coke formation behavior. Adsorbed oxygen-contained species (carbonate species) formation behavior is related with surface reaction with CH_4 . To understand the overall influence of DBD enhanced CH_4 and CO_2 activation on MDR, the electrical properties was analyzed by Lissajous analysis and electron-molecule collisions theory. Finally, kinetic analysis was carried out to reveal the contribution of vibrational excited CH_4 on DBD-enhanced reforming.

Chapter 1 provides an introduction to methane dry reforming and nonthermal plasma. The research motivation of this study is proposed based on the thermodynamics and kinetic aspects

Chapter 2 investigates the oxidation behavior of Ni/ Al_2O_3 catalyst by DBD-activated CO_2

compared with CO₂ thermal oxidation, aiming for providing new insight into oxidation-reduction cycle of nonthermal plasma-enabled MDR. *Temperature Programmed Reaction Spectrometry* was applied to enable a quantitative analysis of gas consumption which is related to the oxidation of Ni/Al₂O₃ catalysts. The nonthermal plasma oxidation mechanism was further analyzed by Raman spectroscopy, showing the cross-sectional distribution of NiO over the 3 mm spherical catalyst pellets. Nonthermal plasma-excited CO₂ oxidizes Ni only near the external surface of spherical pellets with 20 μm depth: both DBD-excited species generation and penetration into the internal pores are inhibited. The partially oxidized Ni catalyst in the external surface promotes DBD-enabled oxidation-reduction cycle, which was further correlated with coke formation behavior.

Chapter 3 elucidates the nonthermal plasma-enabled reaction enhancement mechanisms by in situ plasma-DRIFTS (Diffuse reflectance Infrared Fourier Transform Spectroscopy). Two catalysts were employed to investigate the role of lanthanum in reforming. Compared with thermal catalysis, DBD-activated CO₂ shows an enhancement for the bidentate and monodentate carbonates formation on La. Moreover, new peaks of bicarbonate and bridge carbonate were formed contributed by nonthermal plasma interaction. The ex situ CO₂-TPD study after DBD- and thermal-activated CO₂ treatment further confirmed that DBD-activated CO₂ enhances bidentate and monodentate carbonates generation at high temperature. XRD and EDS analysis suggest that the atomic-scale interaction between CO₂-La and CH_x-Ni is possible over the complex La-Ni-Al oxide.

The chapter 4 presents the clear evidence of nonthermal plasma-induced synergism of methane dry reforming. Reactant conversion and product yield were increased by superposing DBD to the La-modified Ni/Al₂O₃ catalyst at fixed temperature: reforming performance was further promoted by increasing the operating frequency from 12 kHz to 100 kHz, while maintaining the catalyst temperature as well as specific energy input. Reforming characteristics

were correlated with the electrical properties of packed-bed DBD, showing the increase in discharge current is critically important to strength plasma-induced synergism, while an increase in mean electron energy seems to be a minor effect. Moreover, discharge properties were correlated with electron collision kinetics: the vibrationally excited CH₄ and CO₂ play a key role in plasma catalysis of biogas reforming.

Chapter 5 provides a determination of kinetic parameters of methane dry reforming to elucidate the drastic reaction promotion mechanism enabled by plasma-catalyst interaction. Lanthanum-modified Ni/Al₂O₃ catalyst was combined with DBD at 5 kPa and 400–700 °C without dilution gas. Reaction order for CH₄ and CO₂ were determined respectively as 0.68 and –0.17, which were kept unchanged by DBD, indicating the surface coverage of CH₄ and CO₂ was not influenced by nonthermal plasma. The Arrhenius plot for forward CH₄ rate constant revealed that 12 kHz DBD hybrid reaction is characterized as *mixed catalysis* where plasma and thermal catalysis are not decoupled. The apparent activation energy was influenced only slightly by the specific energy input, because the electrical properties of streamer swarm are not influenced to a large extent by *SEI* at fixed frequency. In contrast, 100 kHz DBD yielded significant improvement of CH₄ and CO₂ conversion via vibrational excitation. Activation energy decreased from 91 kJ/mol to 44.7 kJ/mol which was well correlated with the state-specific gas-surface reactivity of vibrationally excited CH₄ on Ni surfaces.

Chapter 6 provides conclusion and outlook for future work.

1.7 References

- [1] J.J. Bravo-Suárez, R.V. Chaudhari, B. Subramaniam, Novel materials for catalysis and fuels processing, American Chemical Society, 2013, pp. 3-68.
- [2] B.M. Devins J C, Formation of Hydrazine in electric discharge decomposition of Ammonia, Journal of the American Chemical Society 76 (1954) 2618-2626.
- [3] S.T. Wismann, J.S. Engbæk, S.B. Vendelbo, F.B. Bendixen, W.L. Eriksen, K. Aasberg-Petersen, C. Frandsen, I. Chorkendorff, P.M. Mortensen, Electrified methane reforming: A compact approach to greener industrial hydrogen production, Science 364 (2019) 756.
- [4] J.C. Whitehead, in: X. Tu, J.C. Whitehead, T. Nozaki (Eds.), Plasma Catalysis: Fundamentals and Applications, Springer International Publishing, Cham, 2019, pp. 1-19.
- [5] M. Argyle, C. Bartholomew, Heterogeneous catalyst deactivation and regeneration: a review, Catalysts 5 (2015) 145-269.
- [6] D.H. Lee, Y.-H. Song, K.-T. Kim, S. Jo, H. Kang, Current state and perspectives of plasma applications for catalyst regeneration, Catalysis Today 337 (2019) 15-27.
- [7] E. Saracevic, S. Frühauf, A. Miltner, K. Karnpakdee, B. Munk, M. Lebuhn, B. Wlcek, J. Leber, J. Lizasoain, A. Friedl, A. Gronauer, A. Bauer, Utilization of food and agricultural residues for a flexible biogas production: process stability and effects on needed biogas storage capacities, Energies 12 (2019).
- [8] Z. Sheng, K. Sakata, Y. Watanabe, S. Kameshima, H.-H. Kim, S. Yao, T. Nozaki, Factors determining synergism in plasma catalysis of biogas at reduced pressure, Journal of Physics D: Applied Physics 52 (2019) 414002.
- [9] K. Yuan, J.-Q. Zhong, X. Zhou, L. Xu, S.L. Bergman, K. Wu, G.Q. Xu, S.L. Bernasek, H.X. Li, W. Chen, Dynamic oxygen on surface: catalytic intermediate and coking barrier in the Modeled CO₂ reforming of CH₄ on Ni (111), ACS Catalysis 6 (2016) 4330-4339.
- [10] P.R. Shirhatti, I. Rahinov, K. Golibrzuch, J. Werdecker, J. Geweke, J. Altschäffel, S. Kumar, D.J. Auerbach, C. Bartels, A.M. Wodtke, Observation of the adsorption and desorption of vibrationally excited molecules on a metal surface, Nature Chemistry 10 (2018) 592-598.
- [11] R.R. Smith, D.R. Killelea, D.F. DelSesto, A.L. Utz, Preference for vibrational over translational energy in a gas-surface reaction, Science 304 (2004) 992-995.
- [12] K. Li, F. He, H. Yu, Y. Wang, Z. Wu, Theoretical study on the reaction mechanism of carbon dioxide reforming of methane on La and La₂O₃ modified Ni(111) surface, Journal of Catalysis 364 (2018) 248-261.
- [13] H.L. Chen, H.M. Lee, S.H. Chen, Y. Chao, M.B. Chang, Review of plasma catalysis on hydrocarbon reforming for hydrogen production—Interaction, integration, and prospects, Applied Catalysis B: Environmental 85 (2008) 1-9.
- [14] J. Quan, T. Kondo, G. Wang, J. Nakamura, Energy transfer dynamics of formate

- decomposition on Cu(110), *Angewandte Chemie International Edition* 56 (2017) 3496-3500.
- [15] S.K. Bhatia, R.K. Bhatia, J.-M. Jeon, G. Kumar, Y.-H. Yang, Carbon dioxide capture and bioenergy production using biological system—A review, *Renewable and Sustainable Energy Reviews* 110 (2019) 143-158.
 - [16] A. Li, J. Wang, B. Bao, High-efficiency CO₂ capture and separation based on hydrate technology: A review, *Greenhouse Gases: Science and Technology* 9 (2019) 175-193.
 - [17] R.B. Vieira, P.A.S. Moura, E. Vilarrasa-García, D.C.S. Azevedo, H.O. Pastore, Polyamine-grafted magadiite: high CO₂ selectivity at capture from CO₂/N₂ and CO₂/CH₄ mixtures, *Journal of CO₂ Utilization* 23 (2018) 29-41.
 - [18] F.M. Baena-Moreno, M. Rodríguez-Galán, F. Vega, B. Alonso-Fariñas, L.F. Vilches Arenas, B. Navarrete, Carbon capture and utilization technologies: a literature review and recent advances, *Energy Sources, Part A: Recovery, Utilization, and Environmental Effects* 41 (2019) 1403-1433.
 - [19] L. Liu, P.P. Tans, L. Xia, L. Zhou, F. Zhang, Analysis of patterns in the concentrations of atmospheric greenhouse gases measured in two typical urban clusters in China, *Atmospheric Environment* 173 (2018) 343-354.
 - [20] A.H. Kalhapure, D.D. Gaikwad, D. Sah, A. Tripathi, Climate change: Causes, impacts and combat with special reference to agriculture-A review, *Current Advances in Agricultural Sciences (An International Journal)* 11 (2019) 1-10.
 - [21] D. Allen, Attributing atmospheric methane to anthropogenic emission sources, *Accounts of Chemical Research* 49 (2016) 1344-1350.
 - [22] H. Chu, Y. Hosen, K. Yagi, NO, N₂O, CH₄ and CO₂ fluxes in winter barley field of Japanese andisol as affected by N fertilizer management, *Soil Biology and Biochemistry* 39 (2007) 330-339.
 - [23] F.T. Fisher, H. , Conversion of methane into hydrogen and carbon monoxide, *Brennst.-Chem.* 9 (1928).
 - [24] S. Achinas, V. Achinas, G.J.W. Euverink, A technological overview of biogas production from biowaste, *Engineering* 3 (2017) 299-307.
 - [25] H.J. Alves, C. Bley Junior, R.R. Niklevicz, E.P. Frigo, M.S. Frigo, C.H. Coimbra-Araújo, Overview of hydrogen production technologies from biogas and the applications in fuel cells, *International Journal of Hydrogen Energy* 38 (2013) 5215-5225.
 - [26] S.N.B. Villadsen, P.L. Fosbøl, I. Angelidaki, J.M. Woodley, L.P. Nielsen, P. Møller, The potential of biogas; the solution to energy storage, *ChemSusChem* 12 (2019) 2147-2153.
 - [27] L. Gu, Y.-X. Zhang, J.-Z. Wang, G. Chen, H. Batty, Where is the future of China's biogas? Review, forecast, and policy implications, *Petroleum Science* 13 (2016) 604-624.
 - [28] J. Juan-Juan, M.C. Román-Martínez, M.J. Illán-Gómez, Effect of potassium content in the activity of K-promoted Ni/Al₂O₃ catalysts for the dry reforming of methane, *Applied*

Catalysis A: General 301 (2006) 9-15.

- [29] R.G. Grim, A.T. To, C.A. Farberow, J.E. Hensley, D.A. Ruddy, J.A. Schaidle, Growing the bioeconomy through catalysis: a review of recent advancements in the production of fuels and chemicals from syngas-derived oxygenates, *ACS Catalysis* 9 (2019) 4145-4172.
- [30] W. Zhou, K. Cheng, J. Kang, C. Zhou, V. Subramanian, Q. Zhang, Y. Wang, New horizon in C1 chemistry: breaking the selectivity limitation in transformation of syngas and hydrogenation of CO₂ into hydrocarbon chemicals and fuels, *Chemical Society reviews* 48 (2019) 3193-3228.
- [31] Y. Wu, H. Xie, S. Tian, N. Tsubaki, Y. Han, Y. Tan, Isobutanol synthesis from syngas over K–Cu/ZrO₂–La₂O₃ (x) catalysts: Effect of La-loading, *Journal of Molecular Catalysis A: Chemical* 396 (2015) 254-260.
- [32] M.S. Fan, A.Z. Abdullah, S. Bhatia, Catalytic technology for carbon dioxide reforming of methane to synthesis gas, *ChemCatChem* 1 (2009) 192-208.
- [33] A.P.E. York, T.c. Xiao, M.L.H. Green, J.B. Claridge, Methane oxyforming for synthesis gas production, *Catalysis Reviews* 49 (2007) 511-560.
- [34] J.R. Rostrup-Nielsen, New aspects of syngas production and use, *Catalysis Today* 63 (2000) 159-164.
- [35] Y.-g. Chen, K. Tomishige, K. Yokoyama, K. Fujimoto, Promoting effect of Pt, Pd and Rh noble metals to the Ni_{0.03}Mg_{0.97}O solid solution catalysts for the reforming of CH₄ with CO₂, *Applied Catalysis A: General* 165 (1997) 335-347.
- [36] A.D. Ballarini, S.R. de Miguel, E.L. Jablonski, O.A. Scelza, A.A. Castro, Reforming of CH₄ with CO₂ on Pt-supported catalysts: Effect of the support on the catalytic behaviour, *Catalysis Today* 107-108 (2005) 481-486.
- [37] U.L. Portugal, C.M.P. Marques, E.C.C. Araujo, E.V. Morales, M.V. Giotto, J.M.C. Bueno, CO₂ reforming of methane over zeolite-Y supported ruthenium catalysts, *Applied Catalysis A: General* 193 (2000) 173-183.
- [38] S.M. Gheno, S. Damyanova, B.A. Riguetto, C.M.P. Marques, C.A.P. Leite, J.M.C. Bueno, CO₂ reforming of CH₄ over Ru/zeolite catalysts modified with Ti, *Journal of Molecular Catalysis A: Chemical* 198 (2003) 263-275.
- [39] M. Safariamin, L.H. Tidahy, E. Abi-Aad, S. Siffert, A. Aboukaïs, Dry reforming of methane in the presence of ruthenium-based catalysts, *Comptes Rendus Chimie* 12 (2009) 748-753.
- [40] H.Y. Wang, E. Ruckenstein, Carbon dioxide reforming of methane to synthesis gas over supported rhodium catalysts: the effect of support, *Applied Catalysis A: General* 204 (2000) 143-152.
- [41] F. Basile, G. Fornasari, F. Trifirò, A. Vaccari, Rh–Ni synergy in the catalytic partial oxidation of methane: surface phenomena and catalyst stability, *Catalysis Today* 77 (2002) 215-223.

- [42] U.L. Portugal, A.C.S.F. Santos, S. Damyanova, C.M.P. Marques, J.M.C. Bueno, CO₂ reforming of CH₄ over Rh-containing catalysts, *Journal of Molecular Catalysis A: Chemical* 184 (2002) 311-322.
- [43] M.E. Rivas, J.L.G. Fierro, M.R. Goldwasser, E. Pietri, M.J. Pérez-Zurita, A. Griboval-Constant, G. Leclercq, Structural features and performance of LaNi_{1-x}Rh_xO₃ system for the dry reforming of methane, *Applied Catalysis A: General* 344 (2008) 10-19.
- [44] M. Wisniewski, A. Boréave, P. Gélin, Catalytic CO₂ reforming of methane over Ir/Ce_{0.9}Gd_{0.1}O_{2-x}, *Catalysis Communications* 6 (2005) 596-600.
- [45] W.-C. Chung, M.-B. Chang, Review of catalysis and plasma performance on dry reforming of CH₄ and possible synergistic effects, *Renewable and Sustainable Energy Reviews* 62 (2016) 13-31.
- [46] S. Wang, G.Q.M. Lu, CO₂ reforming of methane on Ni catalysts: Effects of the support phase and preparation technique, *Applied Catalysis B: Environmental* 16 (1998) 269-277.
- [47] J. Juan-Juan, M.C. Román-Martínez, M.J. Illán-Gómez, Catalytic activity and characterization of Ni/Al₂O₃ and NiK/Al₂O₃ catalysts for CO₂ methane reforming, *Applied Catalysis A: General* 264 (2004) 169-174.
- [48] J. Guo, H. Lou, H. Zhao, D. Chai, X. Zheng, Dry reforming of methane over nickel catalysts supported on magnesium aluminate spinels, *Applied Catalysis A: General* 273 (2004) 75-82.
- [49] F. Pompeo, N.N. Nichio, M.G. González, M. Montes, Characterization of Ni/SiO₂ and Ni/Li-SiO₂ catalysts for methane dry reforming, *Catalysis Today* 107-108 (2005) 856-862.
- [50] Y.-J. Su, K.-L. Pan, M.-B. Chang, Modifying perovskite-type oxide catalyst LaNiO₃ with Ce for carbon dioxide reforming of methane, *International Journal of Hydrogen Energy* 39 (2014) 4917-4925.
- [51] L. Ji, S. Tang, H.C. Zeng, J. Lin, K.L. Tan, CO₂ reforming of methane to synthesis gas over sol-gel-made Co/ γ -Al₂O₃ catalysts from organometallic precursors, *Applied Catalysis A: General* 207 (2001) 247-255.
- [52] R. Bouarab, O. Akdim, A. Auroux, O. Cherifi, C. Mirodatos, Effect of MgO additive on catalytic properties of Co/SiO₂ in the dry reforming of methane, *Applied Catalysis A: General* 264 (2004) 161-168.
- [53] Z. Hao, Q. Zhu, Z. Jiang, H. Li, Fluidization characteristics of aerogel Co/Al₂O₃ catalyst in a magnetic fluidized bed and its application to CH₄-CO₂ reforming, *Powder Technology* 183 (2008) 46-52.
- [54] X. Tian, Y. Zeng, T. Xiao, C. Yang, Y. Wang, S. Zhang, Fabrication and stabilization of nanocrystalline ordered mesoporous MgO-ZrO₂ solid solution, *Microporous and Mesoporous Materials* 143 (2011) 357-361.

- [55] S. Wang, G.Q. Lu, G.J. Millar, Carbon dioxide reforming of methane to produce synthesis gas over metal-supported catalysts: State of the Art, *Energy & Fuels* 10 (1996) 896-904.
- [56] V.R. Choudhary, B.S. Uphade, A.S. Mamman, Large enhancement in methane-to-syngas conversion activity of supported Ni catalysts due to precoating of catalyst supports with MgO, CaO or rare-earth oxide, *Catalysis Letters* 32 (1995) 387-390.
- [57] A. Sacco, F.W.A.H. Geurts, G.A. Jablonski, S. Lee, R.A. Gately, Carbon deposition and filament growth on Fe, Co, and Ni foils using CH₄-H₂-H₂O-CO-CO₂ gas mixtures, *Journal of Catalysis* 119 (1989) 322-341.
- [58] S. Kameshima, K. Tamura, Y. Ishibashi, T. Nozaki, Pulsed dry methane reforming in plasma-enhanced catalytic reaction, *Catalysis Today* 256 (2015) 67-75.
- [59] S. Kameshima, R. Mizukami, T. Yamazaki, L.A. Prananto, T. Nozaki, Interfacial reactions between DBD and porous catalyst in dry methane reforming, *Journal of Physics D: Applied Physics* 51 (2018) 114006.
- [60] M. Németh, G. Sáfrán, A. Horváth, F. Somodi, Hindered methane decomposition on a coke-resistant Ni-In/SiO₂ dry reforming catalyst, *Catalysis Communications* 118 (2019) 56-59.
- [61] H. Peng, Y. Ma, W. Liu, X. Xu, X. Fang, J. Lian, X. Wang, C. Li, W. Zhou, P. Yuan, Methane dry reforming on Ni/La₂Zr₂O₇ treated by plasma in different atmospheres, *Journal of Energy Chemistry* 24 (2015) 416-424.
- [62] H.M. Mott-Smith, History of “plasmas”, *Nature* 233 (1971) 219-219.
- [63] H.-H. Kim, Y. Teramoto, A. Ogata, H. Takagi, T. Nanba, Plasma catalysis for environmental treatment and energy applications, *Plasma Chemistry and Plasma Processing* 36 (2016) 45-72.
- [64] C. Hibert, I. Gaurand, O. Motret, J.M. Pouvesle, [OH(X)] measurements by resonant absorption spectroscopy in a pulsed dielectric barrier discharge, *Journal of Applied Physics* 85 (1999) 7070-7075.
- [65] R. Rudolph, K.P. Francke, H. Miessner, OH radicals as oxidizing agent for the abatement of organic pollutants in gas flows by dielectric barrier discharges, *Plasmas and Polymers* 8 (2003) 153-161.
- [66] H.-H. Kim, Y. Teramoto, N. Negishi, A. Ogata, A multidisciplinary approach to understand the interactions of nonthermal plasma and catalyst: A review, *Catalysis Today* 256 (2015) 13-22.
- [67] J.C. Whitehead, Plasma-catalysis: the known knowns, the known unknowns and the unknown unknowns, *Journal of Physics D: Applied Physics* 49 (2016) 243001.
- [68] E.C. Neyts, A. Bogaerts, Understanding plasma catalysis through modelling and simulation—a review, *Journal of Physics D: Applied Physics* 47 (2014) 224010.
- [69] R. Snoeckx, A. Bogaerts, Plasma technology – a novel solution for CO₂ conversion?,

Chemical Society reviews 46 (2017) 5805-5863.

- [70] M.L. Carreon, Plasma catalysis: a brief tutorial, *Plasma Research Express* 1 (2019) 043001.
- [71] R. Döbek, F. Azzolina-Jury, A. Travert, F. Maugé, A review on plasma-catalytic methanation of carbon dioxide – Looking for an efficient catalyst, *Renewable and Sustainable Energy Reviews* 116 (2019) 109427.
- [72] C. Tendero, C. Tixier, P. Tristant, J. Desmaison, P. Leprince, Atmospheric pressure plasmas: A review, *Spectrochimica Acta Part B: Atomic Spectroscopy* 61 (2006) 2-30.
- [73] E. Gomez, D.A. Rani, C.R. Cheeseman, D. Deegan, M. Wise, A.R. Boccaccini, Thermal plasma technology for the treatment of wastes: A critical review, *Journal of Hazardous Materials* 161 (2009) 614-626.
- [74] J.R. Fincke, R.P. Anderson, T. Hyde, B.A. Detering, R. Wright, R.L. Bewley, D.C. Haggard, W.D. Swank, Plasma thermal conversion of methane to acetylene, *Plasma Chemistry and Plasma Processing* 22 (2002) 105-136.
- [75] X. Tao, F. Qi, Y. Yin, X. Dai, CO₂ reforming of CH₄ by combination of thermal plasma and catalyst, *International Journal of Hydrogen Energy* 33 (2008) 1262-1265.
- [76] T. Iwase, Y. Kamaji, S.Y. Kang, K. Koga, N. Kuboi, M. Nakamura, N. Negishi, T. Nozaki, S. Nunomura, D. Ogawa, M. Omura, T. Shimizu, K. Shinoda, Y. Sonoda, H. Suzuki, K. Takahashi, T. Tsutsumi, K. Yoshikawa, T. Ishijima, K. Ishikawa, Progress and perspectives in dry processes for emerging multidisciplinary applications: how can we improve our use of dry processes?, *Japanese Journal of Applied Physics* 58 (2019) SE0803.
- [77] B.-B. Hwang, Y.-K. Yeo, B.-K. Na, Conversion of CH₄ and CO₂ to syngas and higher hydrocarbons using dielectric barrier discharge, *Korean Journal of Chemical Engineering* 20 (2003) 631-634.
- [78] A.H. Khoja, M. Tahir, N.A.S. Amin, Recent developments in non-thermal catalytic DBD plasma reactor for dry reforming of methane, *Energy Conversion and Management* 183 (2019) 529-560.
- [79] U. Kogelschatz, Dielectric-barrier discharges: Their history, discharge physics, and industrial applications, *Plasma Chemistry and Plasma Processing* 23 (2003) 1-46.
- [80] E.A. Firoozabadi, S.M.H. Hosseini, Comparison of distinct discharge modes for ozone production in a novel DBD configuration with three flat electrodes, *IEEE Transactions on Plasma Science* 47 (2019) 1562-1571.
- [81] B. Eliasson, M. Hirth, U. Kogelschatz, Ozone synthesis from oxygen in dielectric barrier discharges, *Journal of Physics D: Applied Physics* 20 (1987) 1421-1437.
- [82] G. Niu, Y. Qin, W. Li, Y. Duan, Investigation of CO₂ splitting process under atmospheric pressure using multi-electrode cylindrical DBD plasma reactor, *Plasma Chemistry and Plasma Processing* 39 (2019) 809-824.

- [83] D. Mei, X. Tu, Conversion of CO₂ in a cylindrical dielectric barrier discharge reactor: Effects of plasma processing parameters and reactor design, *Journal of CO₂ Utilization* 19 (2017) 68-78.
- [84] A. Ozkan, T. Dufour, T. Silva, N. Britun, R. Snyders, A. Bogaerts, F. Reniers, The influence of power and frequency on the filamentary behavior of a flowing DBD—application to the splitting of CO₂, *Plasma Sources Science and Technology* 25 (2016) 025013.
- [85] D. Ray, D. Nepak, S. Janampelli, P. Goshal, C. Subrahmanyam, Dry reforming of methane in DBD plasma over Ni-Based catalysts: Influence of process conditions and support on performance and durability, *Energy Technology* 7 (2019) 1801008.
- [86] K.H.R. Rouwenhorst, H.-H. Kim, L. Lefferts, Vibrationally excited activation of N₂ in plasma-enhanced catalytic ammonia synthesis: A kinetic analysis, *ACS Sustainable Chemistry & Engineering* 7 (2019) 17515-17522.
- [87] B.S. Patil, Q. Wang, V. Hessel, J. Lang, Plasma N₂-fixation: 1900–2014, *Catalysis Today* 256 (2015) 49-66.
- [88] D. Mei, X. Zhu, Y.-L. He, J.D. Yan, X. Tu, Plasma-assisted conversion of CO₂ in a dielectric barrier discharge reactor: understanding the effect of packing materials, *Plasma Sources Science and Technology* 24 (2014) 015011.
- [89] Y. Uytdenhouten, S. Van Alphen, I. Michiels, V. Meynen, P. Cool, A. Bogaerts, A packed-bed DBD micro plasma reactor for CO₂ dissociation: Does size matter?, *Chemical Engineering Journal* 348 (2018) 557-568.
- [90] H.-H. Kim, Y. Teramoto, A. Ogata, Time-resolved imaging of positive pulsed corona-induced surface streamers on TiO₂ and γ -Al₂O₃-supported Ag catalysts, *Journal of Physics D: Applied Physics* 49 (2016) 415204.
- [91] A. Khacef, P. Da Costa, in: X. Tu, J.C. Whitehead, T. Nozaki (Eds.), *Plasma catalysis: Fundamentals and applications*, Springer International Publishing, Cham, 2019, pp. 115-144.
- [92] P. Talebizadeh, M. Babaie, R. Brown, H. Rahimzadeh, Z. Ristovski, M. Arai, The role of non-thermal plasma technique in NO_x treatment: A review, *Renewable and Sustainable Energy Reviews* 40 (2014) 886-901.
- [93] K.P. Francke, R. Rudolph, H. Miessner, Design and operating characteristics of a simple and reliable DBD reactor for use with atmospheric air, *Plasma Chemistry and Plasma Processing* 23 (2003) 47-57.
- [94] T. Nozaki, S. Kameshima, Z. Sheng, K. Tamura, T. Yamazaki, in: X. Tu, J.C. Whitehead, T. Nozaki (Eds.), *Plasma catalysis: Fundamentals and applications*, Springer International Publishing, Cham, 2019, pp. 231-269.
- [95] A. Mizuno, M. Craven, in: X. Tu, J.C. Whitehead, T. Nozaki (Eds.), *Plasma catalysis: fundamentals and applications*, Springer International Publishing, Cham, 2019, pp. 21-

- [96] C.S. Kalra, A.F. Gutsol, A.A. Fridman, Gliding arc discharges as a source of intermediate plasma for methane partial oxidation, *IEEE Transactions on Plasma Science* 33 (2005) 32-41.
- [97] S.M.A. Mousavi, W. Piavis, S. Turn, Reforming of biogas using a non-thermal, gliding-arc, plasma in reverse vortex flow and fate of hydrogen sulfide contaminants, *Fuel Processing Technology* 193 (2019) 378-391.
- [98] D.H. Lee, K.T. Kim, M.S. Cha, Y.H. Song, Optimization scheme of a rotating gliding arc reactor for partial oxidation of methane, *Proceedings of the Combustion Institute* 31 (2007) 3343-3351.
- [99] L. Song, T. Liang, C. Liu, X. Li, Experimental investigation of hydrogen production by $\text{CH}_4 - \text{CO}_2$ reforming using rotating gliding arc discharge plasma, *International Journal of Hydrogen Energy* 44 (2019) 29450-29459.
- [100] Y. Ma, J.D. Harding, X. Tu, Catalyst-free low temperature conversion of n-dodecane for co-generation of CO_x -free hydrogen and C_2 hydrocarbons using a gliding arc plasma, *International Journal of Hydrogen Energy* 44 (2019) 26158-26168.
- [101] D. Mei, S. Liu, Y. Wang, H. Yang, Z. Bo, X. Tu, Enhanced reforming of mixed biomass tar model compounds using a hybrid gliding arc plasma catalytic process, *Catalysis Today* 337 (2019) 225-233.
- [102] W. Baowei, L. Shize, P. Yeping, W. Chengyu, Gliding arc plasma reforming of toluene for on-board hydrogen production, *International Journal of Hydrogen Energy* 45 (2020) 6138-6147.
- [103] A. Indarto, J.-W. Choi, H. Lee, H.K. Song, Effect of additive gases on methane conversion using gliding arc discharge, *Energy* 31 (2006) 2986-2995.
- [104] D.H. Lee, K.-T. Kim, M.S. Cha, Y.-H. Song, Plasma-controlled chemistry in plasma reforming of methane, *International Journal of Hydrogen Energy* 35 (2010) 10967-10976.
- [105] Y. Xia, N. Lu, J. Li, N. Jiang, K. Shang, Y. Wu, Combined steam and CO_2 reforming of CH_4 for syngas production in a gliding arc discharge plasma, *Journal of CO_2 Utilization* 37 (2020) 248-259.
- [106] M.R. Ghezzar, F. Abdelmalek, M. Belhadj, N. Benderdouche, A. Addou, Enhancement of the bleaching and degradation of textile wastewaters by gliding arc discharge plasma in the presence of TiO_2 catalyst, *Journal of Hazardous Materials* 164 (2009) 1266-1274.
- [107] X. Zhao, M. Ohkohchi, M. Wang, S. Iijima, T. Ichihashi, Y. Ando, Preparation of high-grade carbon nanotubes by hydrogen arc discharge, *Carbon* 35 (1997) 775-781.
- [108] A. Loiseau, F. Willaime, N. Demoncey, G. Hug, H. Pascard, Boron nitride nanotubes with reduced numbers of layers synthesized by arc discharge, *Physical Review Letters* 76 (1996) 4737-4740.
- [109] H. Puliyalil, D. Lašič Jurković, V.D.B.C. Dasireddy, B. Likozar, A review of plasma-

- assisted catalytic conversion of gaseous carbon dioxide and methane into value-added platform chemicals and fuels, *RSC Advances* 8 (2018) 27481-27508.
- [110] A. Fridman, A. Chirokov, A. Gutsol, Non-thermal atmospheric pressure discharges, *Journal of Physics D: Applied Physics* 38 (2005) R1-R24.
- [111] H.-H. Kim, Nonthermal plasma processing for air-pollution control: A historical review, current issues, and future prospects, *Plasma Processes and Polymers* 1 (2004) 91-110.
- [112] J. Chang, P.A. Lawless, T. Yamamoto, Corona discharge processes, *IEEE Transactions on Plasma Science* 19 (1991) 1152-1166.
- [113] K. Yan, E.J.M. van Heesch, A.J.M. Pemen, P.A.H.J. Huijbrechts, From chemical kinetics to streamer corona reactor and voltage pulse generator, *Plasma Chemistry and Plasma Processing* 21 (2001) 107-137.
- [114] G. Dinelli, L. Civitano, M. Rea, Industrial experiments on pulse corona simultaneous removal of NO_x and SO₂ from flue gas, *IEEE Transactions on Industry Applications* 26 (1990) 535-541.
- [115] M. Young Sun, N. In-Sik, Positive pulsed corona discharge process for simultaneous removal of SO₂ and NO_x from iron-ore sintering flue gas, *IEEE Transactions on Plasma Science* 27 (1999) 1188-1196.
- [116] L. Sivachandiran, A. Khacef, In situ and ex situ NO oxidation assisted by sub-microsecond pulsed multi-pin-to-plane corona discharge: the effect of pin density, *RSC Advances* 6 (2016) 29983-29995.
- [117] Y. Gao, S. Zhang, H. Sun, R. Wang, X. Tu, T. Shao, Highly efficient conversion of methane using microsecond and nanosecond pulsed spark discharges, *Applied Energy* 226 (2018) 534-545.
- [118] J.R. Roth, *Industrial Plasma Engineering, Volume 1 Principles*, Institute of Physics publishing, London, 1995.
- [119] T. Desmet, R. Morent, N. De Geyter, C. Leys, E. Schacht, P. Dubruel, Nonthermal plasma technology as a versatile strategy for polymeric biomaterials surface modification: A review, *Biomacromolecules* 10 (2009) 2351-2378.
- [120] J. Niu, B. Peng, Q. Yang, Y. Cong, D. Liu, H. Fan, Spectroscopic diagnostics of plasma-assisted catalytic systems for NO removal from NO/N₂/O₂/C₂H₄ mixtures, *Catalysis Today* 211 (2013) 58-65.
- [121] J. Shah, W. Wang, A. Bogaerts, M.L. Carreon, Ammonia synthesis by radio frequency plasma catalysis: Revealing the underlying mechanisms, *ACS Applied Energy Materials* 1 (2018) 4824-4839.
- [122] J. Bae, M. Lee, S. Park, M.-G. Jeong, D.-Y. Hong, Y.D. Kim, Y.-K. Park, Y.K. Hwang, Investigation of intermediates in non-oxidative coupling of methane by non-thermal RF plasma, *Catalysis Today* 293-294 (2017) 105-112.
- [123] A.E.E. Putra, S. Nomura, S. Mukasa, H. Toyota, Hydrogen production by radio frequency

- plasma stimulation in methane hydrate at atmospheric pressure, *International Journal of Hydrogen Energy* 37 (2012) 16000-16005.
- [124] A. Bogaerts, T. Kozák, K. van Laer, R. Snoeckx, Plasma-based conversion of CO₂: current status and future challenges, *Faraday Discussions* 183 (2015) 217-232.
- [125] Y. Qin, G. Niu, X. Wang, D. Luo, Y. Duan, Status of CO₂ conversion using microwave plasma, *Journal of CO₂ Utilization* 28 (2018) 283-291.
- [126] V.D. Rusanov, A.A. Fridman, G.V. Sholin, The physics of a chemically active plasma with nonequilibrium vibrational excitation of molecules, *Soviet Physics Uspekhi* 24 (1981) 447-474.
- [127] A. Berthelot, A. Bogaerts, Modeling of CO₂ splitting in a microwave plasma: How to improve the conversion and energy efficiency, *The Journal of Physical Chemistry C* 121 (2017) 8236-8251.
- [128] W. Bongers, H. Bouwmeester, B. Wolf, F. Peeters, S. Welzel, D. van den Bekerom, N. den Harder, A. Goede, M. Graswinckel, P.W. Groen, J. Kopecki, M. Leins, G. van Rooij, A. Schulz, M. Walker, R. van de Sanden, Plasma-driven dissociation of CO₂ for fuel synthesis, *Plasma Processes and Polymers* 14 (2017) 1600126.
- [129] L.J. Bailin, B.L. Hertzler, D.A. Oberacker, Development of microwave plasma detoxification process for hazardous wastes. Part I, *Environmental Science & Technology* 12 (1978) 673-679.
- [130] J.-S. Chang, Recent development of plasma pollution control technology: a critical review, *Science and Technology of Advanced Materials* 2 (2001) 571-576.
- [131] M. Dors, H. Nowakowska, M. Jasiński, J. Mizeraczyk, Chemical kinetics of methane pyrolysis in microwave plasma at atmospheric pressure, *Plasma Chemistry and Plasma Processing* 34 (2014) 313-326.
- [132] M. Jasiński, D. Czyłkowski, B. Hrycak, M. Dors, J. Mizeraczyk, Atmospheric pressure microwave plasma source for hydrogen production, *International Journal of Hydrogen Energy* 38 (2013) 11473-11483.
- [133] I. Rahim, S. Nomura, S. Mukasa, H. Toyota, Decomposition of methane hydrate for hydrogen production using microwave and radio frequency in-liquid plasma methods, *Applied Thermal Engineering* 90 (2015) 120-126.
- [134] B. Hrycak, D. Czyłkowski, M. Jasiński, M. Dors, J. Mizeraczyk, Hydrogen production via synthetic biogas reforming in atmospheric-pressure microwave (915 MHz) plasma at high gas-flow output, *Plasma Chemistry and Plasma Processing* 39 (2019) 695-711.
- [135] Z. Sheng, S. Kameshima, K. Sakata, T. Nozaki, Plasma-enabled dry methane reforming, in: N. Britun, T. Silva (Eds.), *Plasma Chemistry and Gas Conversion*, IntechOpen, London, pp. 37-57.
- [136] D. Ray, P.M.K. Reddy, C. Subrahmanyam, Ni-Mn/ γ -Al₂O₃ assisted plasma dry reforming of methane, *Catalysis Today* 309 (2018) 212-218.

- [137] D. Ray, D. Nepak, T. Vinodkumar, C. Subrahmanyam, g-C₃N₄ promoted DBD plasma assisted dry reforming of methane, *Energy* 183 (2019) 630-638.
- [138] Y. Zeng, X. Zhu, D. Mei, B. Ashford, X. Tu, Plasma-catalytic dry reforming of methane over γ -Al₂O₃ supported metal catalysts, *Catalysis Today* 256 (2015) 80-87.
- [139] L. Wang, Y. Yi, C. Wu, H. Guo, X. Tu, One-step reforming of CO₂ and CH₄ into high-value liquid chemicals and fuels at room temperature by plasma-driven catalysis, *Angewandte Chemie International Edition* 56 (2017) 13679-13683.
- [140] D. Li, V. Rohani, F. Fabry, A. Parakkulam Ramaswamy, M. Sennour, L. Fulcheri, Direct conversion of CO₂ and CH₄ into liquid chemicals by plasma-catalysis, *Applied Catalysis B: Environmental* 261 (2020) 118228.
- [141] H. Wang, B. Zhao, L. Qin, Y. Wang, F. Yu, J. Han, Non-thermal plasma-enhanced dry reforming of methane and CO₂ over Ce-promoted Ni/C catalysts, *Molecular Catalysis* 485 (2020) 110821.
- [142] X. Tu, J.C. Whitehead, Plasma-catalytic dry reforming of methane in an atmospheric dielectric barrier discharge: Understanding the synergistic effect at low temperature, *Applied Catalysis B: Environmental* 125 (2012) 439-448.
- [143] X. Wang, Y. Gao, S. Zhang, H. Sun, J. Li, T. Shao, Nanosecond pulsed plasma assisted dry reforming of CH₄: The effect of plasma operating parameters, *Applied Energy* 243 (2019) 132-144.
- [144] N. Lu, X. Bao, N. Jiang, K. Shang, J. Li, Y. Wu, Non-thermal plasma-assisted catalytic dry reforming of methane and carbon dioxide over G-C₃N₄-based catalyst, *Topics in Catalysis* 60 (2017) 855-868.
- [145] A.H. Khoja, M. Tahir, N.A.S. Amin, Cold plasma dielectric barrier discharge reactor for dry reforming of methane over Ni/ γ -Al₂O₃-MgO nanocomposite, *Fuel Processing Technology* 178 (2018) 166-179.
- [146] D. Yap, J.-M. Tatibouët, C. Batiot-Dupeyrat, Catalyst assisted by non-thermal plasma in dry reforming of methane at low temperature, *Catalysis Today* 299 (2018) 263-271.
- [147] X. Zheng, S. Tan, L. Dong, S. Li, H. Chen, Plasma-assisted catalytic dry reforming of methane: Highly catalytic performance of nickel ferrite nanoparticles embedded in silica, *Journal of Power Sources* 274 (2015) 286-294.
- [148] N. Bouchoul, E. Fourré, J.-M. Tatibouët, C. Batiot-Dupeyrat, Plasma-catalytic dry reforming of CH₄ over calcium oxide: Catalyst structural and textural modifications, *Plasma Chemistry and Plasma Processing* 39 (2019) 713-727.
- [149] A.H. Khoja, M. Tahir, N.A. Saidina Amin, Evaluating the performance of a Ni catalyst supported on La₂O₃-MgAl₂O₄ for dry reforming of methane in a packed bed dielectric barrier discharge plasma reactor, *Energy & Fuels* 33 (2019) 11630-11647.
- [150] R. Vakili, R. Gholami, C.E. Stere, S. Chansai, H. Chen, S.M. Holmes, Y. Jiao, C. Hardacre, X. Fan, Plasma-assisted catalytic dry reforming of methane (DRM) over

- metal-organic frameworks (MOFs)-based catalysts, *Applied Catalysis B: Environmental* 260 (2020) 118195.
- [151] H. Wang, J. Han, Z. Bo, L. Qin, Y. Wang, F. Yu, Non-thermal plasma enhanced dry reforming of CH₄ with CO₂ over activated carbon supported Ni catalysts, *Molecular Catalysis* 475 (2019) 110486.
- [152] J.C. Solarte-Toro, Y. Chacón-Pérez, C.A. Cardona-Alzate, Evaluation of biogas and syngas as energy vectors for heat and power generation using lignocellulosic biomass as raw material, *Electronic Journal of Biotechnology* 33 (2018) 52-62.
- [153] A.H. Khoja, M. Tahir, N.A.S. Amin, A. Javed, M.T. Mehran, Kinetic study of dry reforming of methane using hybrid DBD plasma reactor over La₂O₃ co-supported Ni/MgAl₂O₄ catalyst, *International Journal of Hydrogen Energy* 45 (2020) 12256-12271.
- [154] B. Jackson, S. Nave, The dissociative chemisorption of methane on Ni(111): The effects of molecular vibration and lattice motion, *The Journal of Chemical Physics* 138 (2013) 174705.
- [155] A.L. Utz, Vibrations that live long and prosper, *Nature Chemistry* 10 (2018) 577-578.
- [156] J. Quan, F. Muttaqien, T. Kondo, T. Kozarashi, T. Mogi, T. Imabayashi, Y. Hamamoto, K. Inagaki, I. Hamada, Y. Morikawa, J. Nakamura, Vibration-driven reaction of CO₂ on Cu surfaces via Eley–Rideal-type mechanism, *Nature Chemistry* 11 (2019) 722-729.
- [157] L.M. Aparicio, Transient isotopic studies and microkinetic modeling of methane reforming over nickel catalysts, *Journal of Catalysis* 165 (1997) 262-274.
- [158] J. Wei, E. Iglesia, Isotopic and kinetic assessment of the mechanism of reactions of CH₄ with CO₂ or H₂O to form synthesis gas and carbon on nickel catalysts, *Journal of Catalysis* 224 (2004) 370-383.
- [159] U. Olsbye, T. Wurzel, L. Mleczko, Kinetic and reaction engineering studies of dry reforming of methane over a Ni/La/Al₂O₃ catalyst, *Industrial & Engineering Chemistry Research* 36 (1997) 5180-5188.
- [160] Y. Cui, H. Zhang, H. Xu, W. Li, Kinetic study of the catalytic reforming of CH₄ with CO₂ to syngas over Ni/ α -Al₂O₃ catalyst: The effect of temperature on the reforming mechanism, *Applied Catalysis A: General* 318 (2007) 79-88.
- [161] J.Z. Luo, Z.L. Yu, C.F. Ng, C.T. Au, CO₂/CH₄ reforming over Ni–La₂O₃/5A: An investigation on carbon deposition and reaction steps, *Journal of Catalysis* 194 (2000) 198-210.
- [162] G. Sierra Gallego, C. Batiot-Dupeyrat, J. Barrault, F. Mondragón, Dual active-site mechanism for dry methane reforming over Ni/La₂O₃ produced from LaNiO₃ perovskite, *Industrial & Engineering Chemistry Research* 47 (2008) 9272-9278.
- [163] C. Pichas, P. Pomonis, D. Petrakis, A. Ladavos, Kinetic study of the catalytic dry reforming of CH₄ with CO₂ over La_{2-x}Sr_xNiO₄ perovskite-type oxides, *Applied Catalysis A: General* 386 (2010) 116-123.

- [164] X. Zheng, S. Tan, L. Dong, S. Li, H. Chen, Silica-coated LaNiO₃ nanoparticles for non-thermal plasma assisted dry reforming of methane: Experimental and kinetic studies, *Chemical Engineering Journal* 265 (2015) 147-156.
- [165] H.H. Kim, G. Prieto, K. Takashima, S. Katsura, A. Mizuno, Performance evaluation of discharge plasma process for gaseous pollutant removal, *Journal of Electrostatics* 55 (2002) 25-41.
- [166] H.-H. Kim, S.-M. Oh, A. Ogata, S. Futamura, Decomposition of gas-phase benzene using plasma-driven catalyst (PDC) reactor packed with Ag/TiO₂ catalyst, *Applied Catalysis B: Environmental* 56 (2005) 213-220.
- [167] B. Zhu, X.-S. Li, J.-L. Liu, X. Zhu, A.-M. Zhu, Kinetics study on carbon dioxide reforming of methane in kilohertz spark-discharge plasma, *Chemical Engineering Journal* 264 (2015) 445-452.
- [168] J. Kim, D.B. Go, J.C. Hicks, Synergistic effects of plasma–catalyst interactions for CH₄ activation, *Physical Chemistry Chemical Physics* 19 (2017) 13010-13021.
- [169] J. Kim, D.B. Go, J.C. Hicks, Synergistic effects of plasma-catalyst interactions for CH₄ activation, *Physical chemistry chemical physics : PCCP* 19 (2017) 13010-13021.
- [170] S. K. P. Veerapandian, N. De Geyter, J.-M. Giraudon, J.-F. Lamonier, R. Morent, The use of zeolites for VOCs abatement by combining non-thermal plasma, adsorption, and/or catalysis: A review, *Catalysts* 9 (2019).
- [171] E.C. Neyts, K. Ostrikov, M.K. Sunkara, A. Bogaerts, Plasma catalysis: Synergistic effects at the nanoscale, *Chemical Reviews* 115 (2015) 13408-13446.
- [172] P.M. Holmblad, J. Wambach, I. Chorkendorff, Molecular beam study of dissociative sticking of methane on Ni(100), *The Journal of Chemical Physics* 102 (1995) 8255-8263.
- [173] H. Yang, J.L. Whitten, Dissociative chemisorption of CH₄ on Ni(111), *The Journal of Chemical Physics* 96 (1992) 5529-5537.
- [174] J. Lee, D.C. Sorescu, X. Deng, Electron-induced dissociation of CO₂ on TiO₂(110), *Journal of the American Chemical Society* 133 (2011) 10066-10069.
- [175] D. Mei, X. Zhu, C. Wu, B. Ashford, P.T. Williams, X. Tu, Plasma-photocatalytic conversion of CO₂ at low temperatures: Understanding the synergistic effect of plasma-catalysis, *Applied Catalysis B: Environmental* 182 (2016) 525-532.
- [176] B. Ashford, Y. Wang, L. Wang, X. Tu, in: X. Tu, J.C. Whitehead, T. Nozaki (Eds.), *Plasma Catalysis: Fundamentals and Applications*, Springer International Publishing, Cham, 2019, pp. 271-307.
- [177] D.A. Constantinou, A.M. Efstathiou, The steam reforming of phenol over natural calcite materials, *Catalysis Today* 143 (2009) 17-24.
- [178] M. Marwood, R. Doepper, M. Prairie, A. Renken, Transient drift spectroscopy for the determination of the surface reaction kinetics of CO₂ methanation, *Chemical Engineering Science* 49 (1994) 4801-4809.

- [179] M.C.J. Bradford, M. Albert Vannice, The role of metal–support interactions in CO₂ reforming of CH₄, *Catalysis Today* 50 (1999) 87-96.
- [180] S.C. Shen, X. Chen, S. Kawi, CO₂ adsorption over Si-MCM-41 materials having basic sites created by postmodification with La₂O₃, *Langmuir* 20 (2004) 9130-9137.
- [181] L. Qian, Z. Ma, Y. Ren, H. Shi, B. Yue, S. Feng, J. Shen, S. Xie, Investigation of La promotion mechanism on Ni/SBA-15 catalysts in CH₄ reforming with CO₂, *Fuel* 122 (2014) 47-53.
- [182] O.V. Manoilova, S.G. Podkolzin, B. Tope, J. Lercher, E.E. Stangland, J.-M. Goupil, B.M. Weckhuysen, Surface acidity and basicity of La₂O₃, LaOCl, and LaCl₃ characterized by IR spectroscopy, TPD, and DFT calculations, *The Journal of Physical Chemistry B* 108 (2004) 15770-15781.
- [183] X.E. Verykios, Catalytic dry reforming of natural gas for the production of chemicals and hydrogen, *International Journal of Hydrogen Energy* 28 (2003) 1045-1063.
- [184] J.F. Múnera, S. Irusta, L.M. Cornaglia, E.A. Lombardo, D. Vargas Cesar, M. Schmal, Kinetics and reaction pathway of the CO₂ reforming of methane on Rh supported on lanthanum-based solid, *Journal of Catalysis* 245 (2007) 25-34.
- [185] K. Pokrovski, K.T. Jung, A.T. Bell, Investigation of CO and CO₂ adsorption on tetragonal and monoclinic zirconia, *Langmuir* 17 (2001) 4297-4303.
- [186] T. Tabakova, F. Boccuzzi, M. Manzoli, D. Andreeva, FTIR study of low-temperature water-gas shift reaction on gold/ceria catalyst, *Applied Catalysis A: General* 252 (2003) 385-397.
- [187] D. Cornu, H. Guesmi, J.-M. Krafft, H. Lauron-Pernot, Lewis acido-basic interactions between CO₂ and MgO surface: DFT and DRIFT approaches, *The Journal of Physical Chemistry C* 116 (2012) 6645-6654.

Chapter 2: Oxidation behavior of Ni/Al₂O₃ catalyst

This chapter is adapted from the publication work:

Zunrong Sheng, Seigo Kameshima, Shuiliang Yao, Tomohiro Nozaki, Journal of Physics D: Applied Physics 51 (2018) 445205 (8pp), DOI: 10.1088/1361-6463/aae17d.

2.1 Abstract

The oxidation behavior of Ni/Al₂O₃ catalyst in CO₂ plasma was investigated compared with CO₂ thermal oxidation, aiming for providing new insight into oxidation-reduction cycle of plasma catalysis of methane dry reforming (MDR). *Temperature Programmed Reaction Spectrometry* was applied to enable a quantitative analysis of gas consumption which is related to the oxidation and reduction of Ni/Al₂O₃ catalysts. The nonthermal plasma oxidation mechanism was further analyzed by Raman spectroscopy, showing the cross-sectional distribution of NiO over the 3 mm spherical catalyst pellets. Nonthermal plasma-excited CO₂ oxidizes Ni only near the external surface of spherical pellets with 20 μm depth: both Dielectric Barrier Discharge (DBD) generation and plasma-excited species diffusion into the internal pores are inhibited. The lattice oxygen in partially oxidized Ni catalyst over the external surface promotes plasma-enabled oxidation-reduction cycle, which was further correlated with coke formation behavior in plasma catalysis of MDR.

2.2 Introduction

Methane dry reforming (R2.1) is one of the promising reactions which utilizes low-valued biogas to be upgraded, presenting important economic and environmental advantages. However, the demand for high-temperature thermal energy ($> 800\text{ }^{\circ}\text{C}$) of this endothermic reaction is the main limitation of application in industrial installation. Moreover, carbon

deposition by CH₄ dehydrogenation over the metallic catalysts will cause serious catalyst deactivation [1, 2]. Reaction R2.2 represents the coke formation on Ni-based catalyst.



The heterogeneous combination of nonthermal plasma and catalysts receives special attention to solve above problems. Nonthermal plasma contains various radicals, excited species, ions, and electrons *etc.*, which might interact with catalyst surface [3]. The reaction temperature could be decreased by the plasma-generated reactive species because those species initiate chemical reaction at lower temperature than thermal catalysis [4-6]. In plasma-catalytic reaction, the plasma could make changes or create new reaction pathway in the surface process over the catalyst. For example, the deposited carbon from Ni catalysts can be removed effectively by reverse-Boudouard reaction (R2.3) via plasma-excited CO₂ [1, 7], regenerating active sites for subsequent CH₄ adsorption [8]. Besides, plasma-assisted preparation of catalyst is a promising approach to modify the physicochemical properties of the catalyst [9-13], e.g., with plasma preparation, the catalyst obtains a higher adsorption capacity [14], higher surface area [10], and higher dispersion of the catalyst material [11, 15-17], contributing to a better performance of catalyst for subsequent catalytic reaction.



The catalyst most extensively used in the MDR reaction is Ni-based catalyst, due to their high activity [18, 19], high availability and low-cost (compared with noble metals) [20]. The activation energy of CH₄ activation on Ni is reported in some experimental and theoretical studies: 0.52 eV on Ni (100) [21], 0.74 eV on Ni (111) [22]. However, nickel catalysts are prone to carbon formation which results in fast deactivation (R2.2) [23]. A study reports that although the sticking probability of CH₄ on nickel is very low (10⁻⁹ at R.T.), while the rest of carbon

from CH₄ dissociative chemisorption converts into carbon filament over the catalyst, leading to deactivation by coke [24]. Kameshima *et al* [25] revealed that in plasma catalysis of MDR, carbon deposition in the internal pores of spherical catalyst pellets was remarkably decreased by dielectric barrier discharge (DBD), although the interaction between DBD and catalyst is confirmed only in the external surface of the pellets. Ref. [25] confirmed that DBD, or nonthermal plasma, creates a new reaction pathway on the surface of catalyst, which decreases carbon concentration from CH₄ dehydrogenation (R2.2) in the internal pores.

Different with the activation of CH₄ on nickel, CO₂ is demonstrated to be activated on basic support, such as CaO [26], TiO₂ [27], La₂O₃ [28-32], ZrO₂ [33], CeO₂ [34], MgO [35] to form adsorbed oxygen (e.g. carbonate species). But very few works report the interaction between Ni and CO₂ plasma in MDR. Interesting, this study found the significant oxidation of Ni catalyst (R2.4) was possible only when catalyst pellets were exposed to nonthermal plasma under CO₂ flow. Meanwhile, Ni catalyst is only slightly oxidized by CO₂ in the thermal catalysis regime [36, 37]. We hypothesize that Ni oxidation uptakes surface lattice oxygen beyond adsorption/desorption equilibrium, known as Langmuir isotherm, in plasma catalysis which promotes CH₄ dehydrogenation without solid carbon formation (R2.5):



This chapter describes oxidation behavior of Ni catalysts by CO₂ in plasma catalysis: DBD was employed as plasma oxidation compared with thermal oxidation. For the plasma oxidation process, it is necessary to be divided different oxidation conditions based on the *Specific Energy Input* (SEI in eV/molecule). Because the dominative reaction should be distinguished from oxidation by O₂ or CO₂. Moreover, the oxidation mechanism was analyzed by Raman spectroscopy which identifies NiO distribution over cross-section of 3 mm spherical catalyst pellets. The oxidation behavior was further correlated with carbon deposition behavior over the

pellets, which provides a deeper insight into nonthermal plasma-enabled reaction enhancement mechanism in MDR.

2.3 Experiment methods

Figure 2.1 shows the catalyst packed-bed DBD reactor in this study. Briefly, this reactor includes quartz tube (inner diameter; 20 mm), 3 mm diameter high voltage electrode at the center, and the ground electrode outside of quartz tube. Commercially available catalyst pellets (12wt%-Ni/Al₂O₃, spherical 3 mm mean diameter, Süd-Chemie) was packed for 40 mm length (mass of catalyst was ca. 14 g). A high voltage power source (12 kHz, 16 kV_{p-p}) was applied to generate DBD among the pellet spaces. Discharge power was measured by voltage-charge Lissajous analysis. Real-time gaseous components were analyzed by a quadruple mass spectrometer (QMS, Prisma-100; Pfeiffer Vacuum GmbH). Catalyst temperature was controlled by a furnace at constant heating rate of 10 °C/min during *Temperature Programmed Reaction Spectrometry* and the final temperature of catalyst was fixed at 600 °C. Meanwhile, the temperature distribution of the catalyst bed was measured by thermography (TH5104; NEC San-ei Instrument Ltd.) through the observation window. The emissivity of catalyst pellets was estimated to be 0.82 both in oxidation and reduction processes. The temperature measured by thermography and from optical emission spectroscopy [38] were matched within reasonable error range.

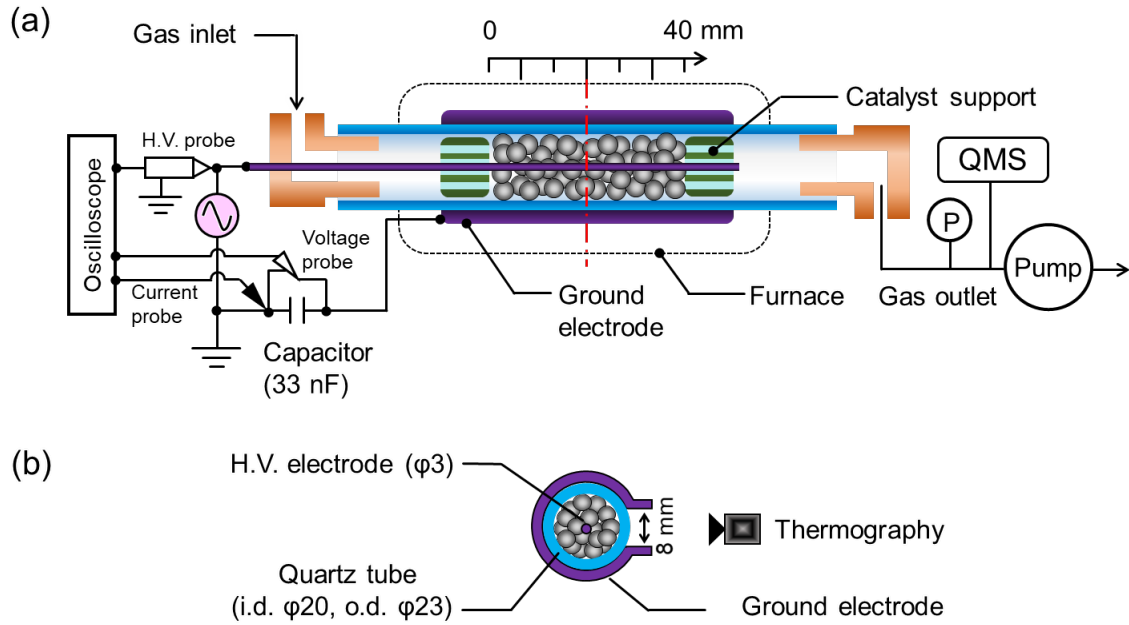


Figure 2.1 Experimental system: (a) overview; (b) cross-sectional view.

The *Specific Energy Input (SEI)* is a critical operational parameter in the CO₂ DBD treatment because the dominant reaction pathway changes dramatically with *SEI*, which is formulated in Eq 2.1.

$$\begin{aligned}
 SEI \left(\frac{\text{eV}}{\text{molecule}} \right) &= \frac{\text{Power (W)}}{e N_A \times \frac{Q_{\text{total}}^{\text{in}}}{60 \times 10^6} \times \frac{P}{RT}} \\
 &= C \times \frac{\text{Power (W)}}{Q_{\text{total}}^{\text{in}} (\text{cm}^3/\text{min})}
 \end{aligned}
 \tag{Eq 2.1}$$

SEI expresses discharge energy consumption per unit volume of feed gas, which is also interpreted as mean electrical energy put into a single molecule. The $Q_{\text{total}}^{\text{in}}$ represents total volumetric gas flow rate at the reactor inlet (cm³/min); $e = 1.602 \times 10^{-19}$ (C); $N_A = 6.02 \times 10^{23}$; $R = 8.314$ J/K/mol; C represents a conversion factor of the unit which is 15.26 ($\frac{\text{eV}}{\text{molecule}} \times \frac{\text{W}}{\text{cm}^3/\text{min}}$) [7]. Plasma oxidation of Ni catalysts was carried out in two contrasting conditions: One is small *SEI* where CO₂ dissociation to CO and 0.5 O₂ (R2.7) is minimized so that the effect of DBD-excited CO₂ is purely extracted: this process is designated as *direct*

oxidation route (R2.6). The other is large *SEI* where CO₂ and O₂ provide the key oxidation pathways: Ni oxidation by O₂ (R2.8), which is designated as *indirect oxidation route*, occurs in parallel: therefore, plasma oxidation with large *SEI* is expressed as *mixed oxidation route* as summarized in Table 2.1. The thermal oxidation of Ni catalysts was also investigated, providing the clear difference between plasma and thermal oxidation processes. The detailed operational parameters are presented in Table 2.1.

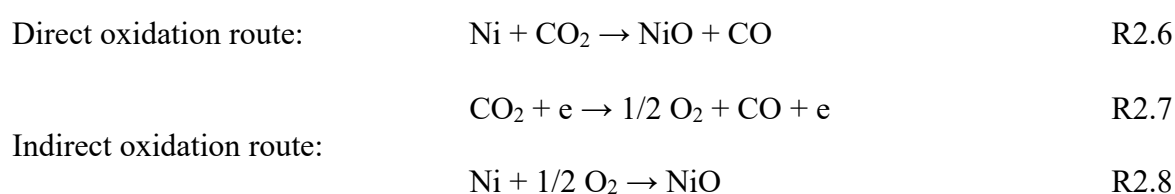


Table 2.1. The operational parameters

Run	Oxidation route	CO ₂ flow rate (cm ³ /min)	Power (W)	<i>SEI</i> (eV/molecule)	Pressure (kPa)	Time (min)
a.	<i>Plasma oxidation</i>	<i>Mixed</i> (<i>Direct and Indirect</i>)	34	47.4	5	70
b.	<i>Thermal oxidation</i>	<i>Direct</i>	—	—		
c.	<i>Plasma oxidation</i>	<i>Direct</i>	33	0.46		
d.	<i>Thermal oxidation</i>	<i>Direct</i>	—	—		

2.4 Mixed oxidation route

Figure 2.2 shows the result of plasma oxidation of Ni catalyst with sufficiently large *SEI* (Run *a*). The furnace temperature was increased at a constant heating rate of 10 °C/min; correspondingly, catalyst temperature was recorded by the thermo-camera. DBD was turned on from 20 min to 90 min.

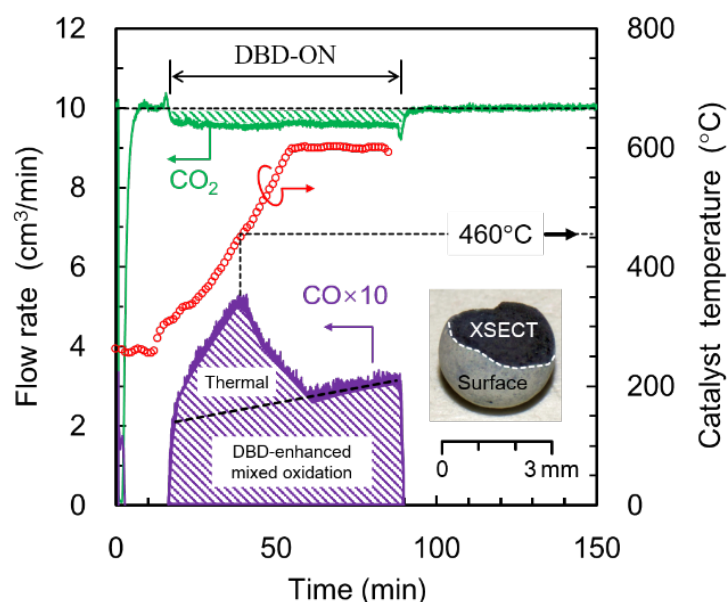


Figure 2.2 Temperature programmed plasma oxidation of Ni catalyst (Run *a*): CO signal is multiplied by 10.

CO₂ is dissociated into CO and O₂ without heterogeneous catalysts by electron impact [39, 40]. Relationship between *SEI* and CO₂ conversion was reproduced from the cited literatures [41-43] as shown in Figure 2.3. CO₂ conversion would reach on the order of 20% when *SEI* increases to ca. 50 eV/molecule, implying that gas composition during CO₂ DBD treatment is approximately CO₂: 73%, CO: 18% and O₂: 9%. The oxidation behavior considering both CO₂ (R2.6) and O₂ (R2.8) must be taken into account.

The consumption of CO₂ and the generation of CO profile was measured by mass spectrometer, which are shown in Figure 2.2. The CO profile is magnified 10 times to

distinguish different reaction routes. Inset picture in Figure 2.2 shows a catalyst pellet after DBD treatment, showing the external surface was selectively oxidized to whitish color change. Interestingly, the cross-section of the hemispherical pellet has been kept in black; the Ni in the internal pores was not oxidized. The integration of CO₂ and CO profile over the time of DBD treatment (20–90 min) deduces the net amount of CO₂ consumption (60.0 cm³) and the corresponding CO generation (49.9 cm³). Difference between CO₂ consumption and CO generation is due to measurement error because concentration change is too small to be measured accurately. We have confirmed that coke was not produced by CO₂ treatment in our previous study [25].

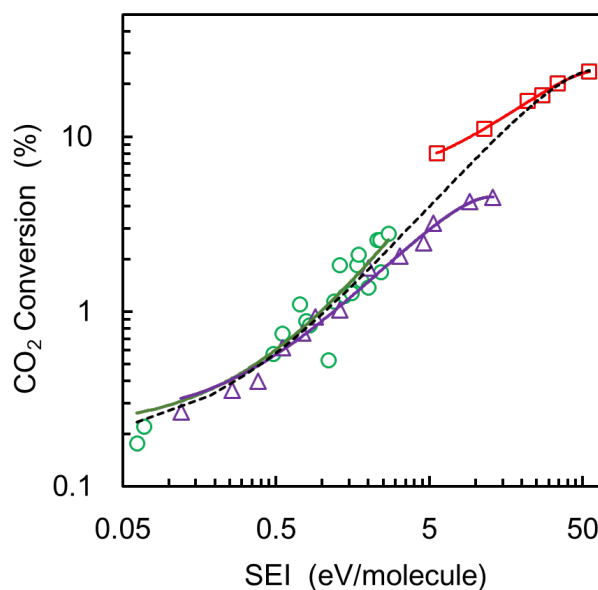


Figure 2.3 CO₂ conversion as a function of *SEI* in DBD without catalys. Cited literatures from □Aerts [41]; ○Butterworth [42]; ΔBrehmer [43].

Figure 2.4 shows the result of thermal oxidation. Unlike plasma oxidation, the homogeneous CO₂ dissociation did not occur; it was purely direct oxidation route in thermal catalysis regime. CO₂ consumption was too small to be detected with the given system; it was estimated from the integration of CO profile, leading to the net CO generation (proximity of net CO₂ conversion) of 4.1 cm³, which is close to the CO generation in thermal route in Figure

2.2. It is further validated that the external surface of catalyst pellets remained black at the end of oxidation from the inset picture; catalyst pellets were unoxidized stage. Moreover, DBD oxidation occurs selectively over the external surface of pellets, indicating both DBD generation and plasma-excited species diffusion into the internal pores are inhibited.

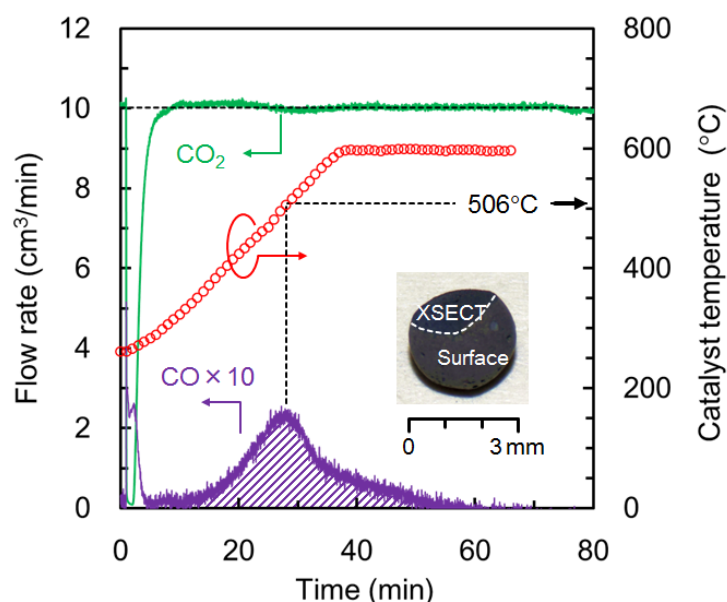


Figure 2.4 Temperature programmed thermal oxidation of Ni catalysts by CO₂ (Run *b*).

In the thermal oxidation, CO increased with catalyst temperature up to 506°C, and turned to decrease with further increase in the temperature. CO₂ is most likely adsorbed at the boundary between Ni nanocrystals and Al₂O₃ interfaces [44-46] (Figure 2.5 (a)). Subsequently, adsorbed CO₂ react with Ni to form NiO near the perimeter of Ni nanoparticles. Reaction sites for thermal oxidation would be quite limited which is proven by a small amount of CO production. When reaction sites are fully oxidized by adsorbed CO₂, Ni oxidation no longer takes place and CO signal decreases even at elevated temperature.

In the mixed oxidation route, CO profile also shows similar peak at 460°C with presumably the same oxidation mechanism by the thermal catalysis. Moreover, DBD-enhanced Ni oxidation occurs in parallel, which increases the net CO production. Unlike thermal

oxidation, CO_2 is primarily excited by electron impact [47, 48], such as vibrational states, which would enhance CO_2 adsorption followed by oxidation of Ni catalyst. Because Ni catalyst is oxidized extensively in DBD, we speculate that Ni nanoparticle oxidation occurs not only perimeter but also terrace, step, and kink as schematically illustrated in Figure 2.5 (b). Assume gas phase CO_2 dissociation by DBD is independent of catalyst temperature, while temperature-dependent thermal oxidation takes place in parallel; CO profile in the plasma oxidation would be divided into two parts as depicted in Figure 2.2; however, the individual contribution of O_2 and CO_2 on the Ni oxidation is not separated clearly. In the next section, additional temperature programmed reaction spectrometry was studied, focusing on DBD-enhanced CO_2 oxidation of Ni catalysts.

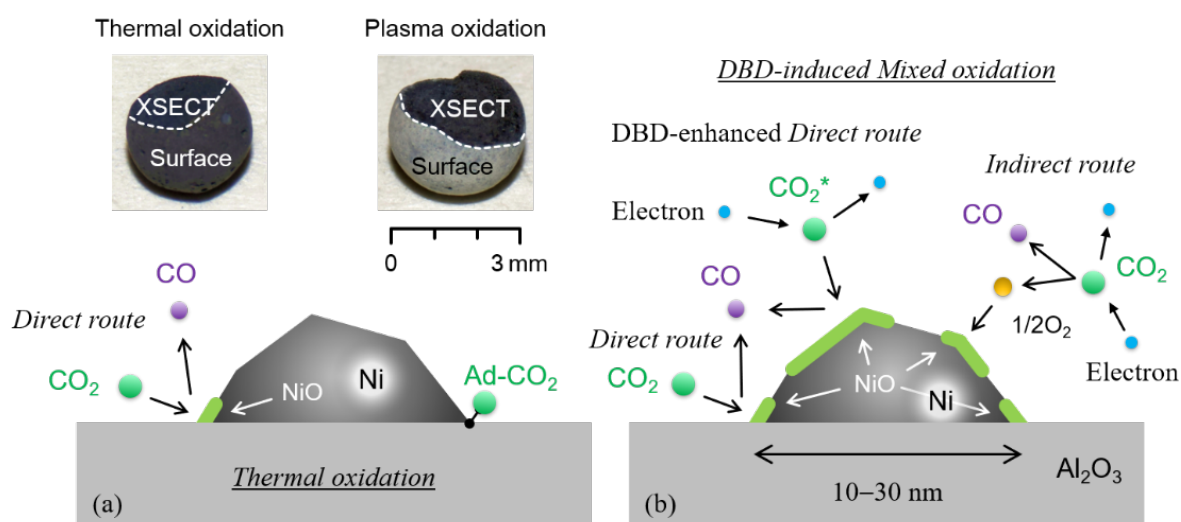


Figure 2.5 Ni oxidation pathways: (a) Thermal oxidation with direct oxidation route including CO_2 adsorption near the perimeter of Ni catalysts. (b) DBD-enhanced mixed oxidation route. Inset pictures show hemispherical catalyst pellets after plasma and thermal oxidation.

2.5 Plasma-enhanced direct oxidation route

In the previous section, it is confirmed that oxidation capability of mix plasma oxidation is stronger than that of thermal oxidation. Meanwhile, the individual contribution of O₂ and CO₂ on Ni oxidation was not separated clearly. In this section, DBD-enhanced direct oxidation route will be investigated, because plasma-induced synergistic effect was observed clearly without O₂ [1, 7, 25]. As shown in Figure 2.3, CO₂ conversion is far below 1 % when the *SEI* was smaller than 0.5 eV/molecule; therefore, Ni oxidation behavior without O₂ can be studied with small *SEI*.

2.5.1 Raman spectroscopy

Because the experiment was carried out at large CO₂ flow (Run *c* and *d*), the conversion of CO₂, as well as the generation of CO, were too small to detect. Instead of gas analysis, the formation of NiO and its distribution over the cross-section of 3 mm spherical pellets were investigated by Raman spectroscopy (NRS-4100, JASCO, 532 nm excitation). Figure 2.6 shows the Raman spectra from surface to center of pellets together with optical microscope images.

In Figure 2.6 (a), spectrum features NiO with one-phonon (560 cm⁻¹ modes), two-phonon (2TO at 740 cm⁻¹, TO + LO at 925 cm⁻¹ and 2LO at 1100 cm⁻¹ modes) excitations as well as two-magnon excitations (at ~1500 cm⁻¹) [49]. Two sharp peaks appearing at 375 cm⁻¹ and 412 cm⁻¹ are Al₂O₃ crystal [50]. NiO peaks were recognized clearly between the external surface and 20 μm depth. Although a weak signal of NiO was detected at 30 μm and 40 μm depth, the optical microscope image shows the thickness of NiO layer is ca. 20 μm. The formation of NiO layer is similar to *mixed oxidation* where Ni oxidation by O₂ occurs in parallel. In contrast, NiO spectrum was not appeared in any depth in Figure 2.6 (b) after thermal oxidation. It is further proved by microscope image that NiO layer was not identified. It is important to emphasize

that DBD-excited CO₂ has a strong oxidation capability of Ni catalysts.

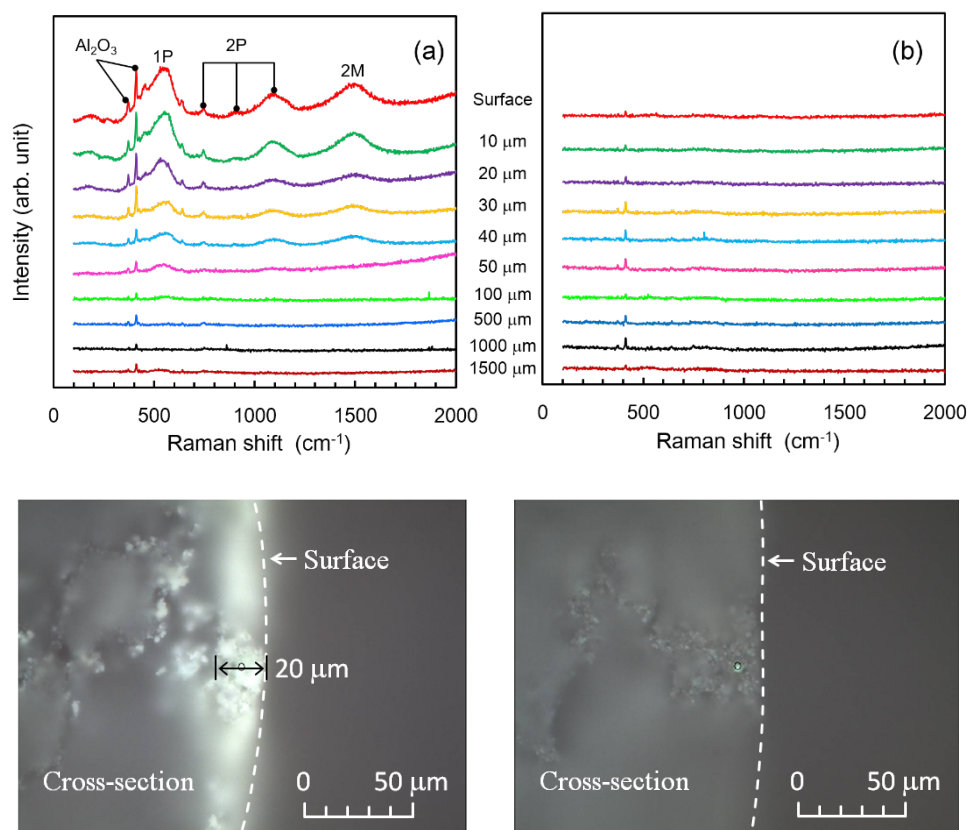


Figure 2.6 NiO distribution over the cross-section of catalyst pellets: (a) Plasma oxidation (Run *c*); and (b) Thermal oxidation (Run *d*) with optical microscope images.

2.5.2 Plasma species generation and penetration

The Figure 2.7 (a-c) shows the morphology of Ni/Al₂O₃ catalyst by scanning electron microscope (SEM). The pore size of catalyst is roughly estimated to be smaller than 1 μm since that the size of Al₂O₃ particles is about 200~600 nm, resulting in the pore size of this catalyst is near to this range. Paschen's law is formulated in Eq 2.2, where *A* and *B* represent empirical constants, and γ is Townsend's secondary ionization coefficient. Plasma onset voltage V_b is a function of the gap distance (*d*) and pressure (*p*), i.e. $V_b = f(pd)$, leading to a minimum value, called *Paschen minimum* [51]. Plasma cannot be generated in the internal pores which is

smaller than *Paschen minimum*. Based on reference [52], the *Paschen minimum* is estimated around 200 μm in this study. Moreover, it is necessary to consider the penetration of plasma-generated species based on the *Debye length* (λ_{de}) (Eq 2.3) [53, 54], where the ϵ_0 is the permittivity of free space, and the T_e , n_e , and e is electron temperature, plasma density in stream, and electronic charge respectively. The *Debye length* of DBD is estimated as 1~100 μm [55].

$$V_b = \frac{Bpd}{(Apd) - \ln \left[\ln \left(1 + \frac{1}{\gamma} \right) \right]} \quad \text{Eq 2.2}$$

$$\lambda_{de} \equiv \left(\frac{\epsilon_0 T_e}{n_e e} \right)^{\frac{1}{2}} = 7430 \left(\frac{T_e}{n_e} \right)^{\frac{1}{2}} \quad \text{Eq 2.3}$$

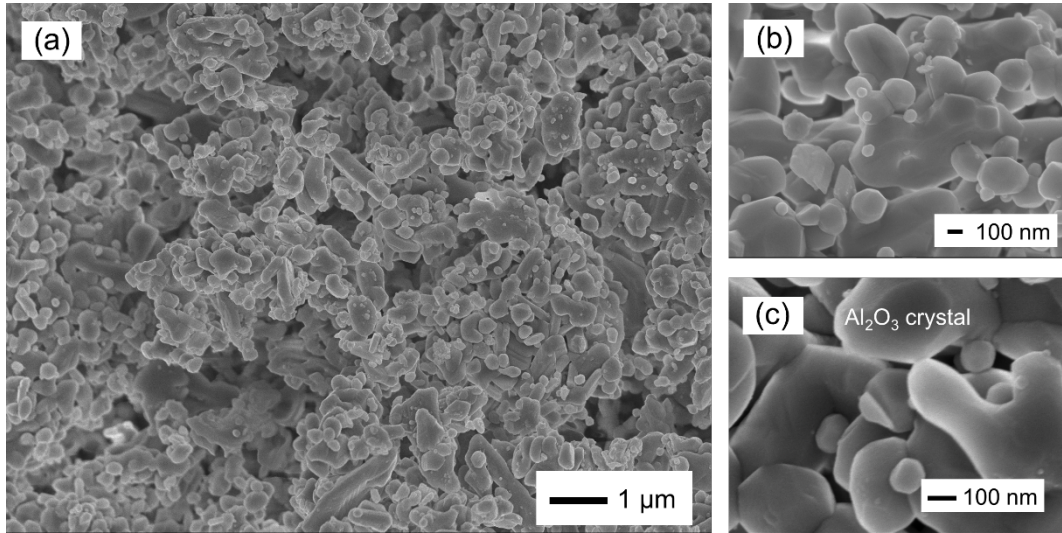


Figure 2.7 The morphology of Ni/Al₂O₃ catalyst by SEM.

It is clear that the pore size is much smaller than both *Paschen minimum* and *Debye length* at given condition, concluding that the effect of DBD is limited near the external surface of the pellets, which is also proved by the model prediction [53, 56] and literature reviews [6, 51]. For the deeper NiO layer with thickness of 20 μm after CO₂ plasma oxidation, we hypothesize that surface diffusion of electrons may play the key role to Ni oxidation by CO₂: because

activation energy of electrically charge catalyst may decrease [57]. The role of charged catalyst should not be discarded at this point, but a detailed discussion is beyond the scope of the present study.

2.5.3 H₂-TPR

The DBD-enhanced direct oxidation route was further investigated indirectly by temperature program reduction (TPR) to understand the oxidation behaviors. After the *run* (c) and (d), the TPR was carried out with 10 cm³/min H₂ at a heating rate of 10 °C /min. The consumption rate of H₂ and catalyst temperature were recorded as a function of time by QMS and thermography respectively. Figure 2.8 (a) shows the TPR profile after thermal oxidation, where the peak (I) and (II) between 200 and 350 °C are assigned to reduction of bulk NiO [58, 59], and the oxidation of the terrace, step and kink could not be separated clearly. The peak (III) at much higher temperature is assigned to the reaction of the NiO in the perimeter cooperated with Al₂O₃ [58, 59]. Figure 2.8 (b) shows the TPR profile after DBD oxidation where the peak (I) and (II) are much stronger than that in thermal oxidation, illustrating that the plasma CO₂ induces a much stronger bulk NiO oxidation than thermal CO₂. The oxidation amount (corresponds to H₂ consumption in unit of cm³) was integrated indirectly by H₂-TPR profile (flowrate vs. time), and the results are presented in the insert sheet in Figure 2.8. The oxidation capability of DBD CO₂ is approximately 3.7-fold stronger than that of thermal oxidation. Moreover, the most obvious enhancement is presented for peak (II) related with bulk NiO, revealing the DBD CO₂ could enhance the bulk Ni nanocrystal oxidation.

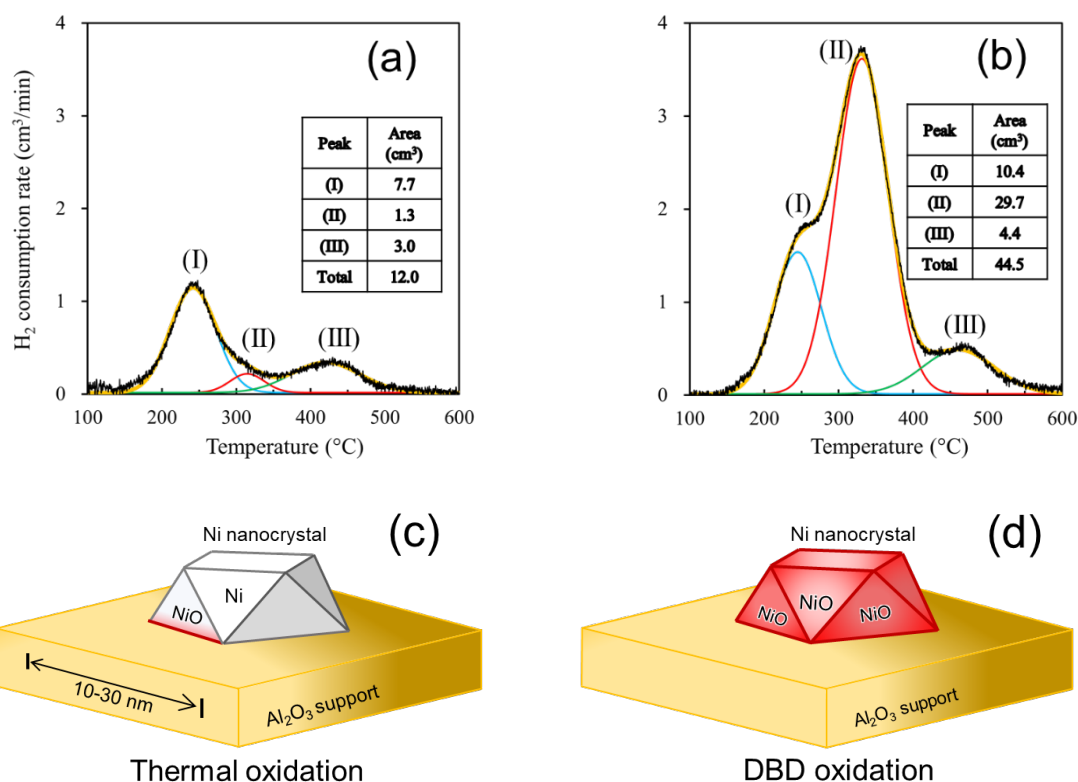


Figure 2.8 The TPR profiles after (a) thermal oxidation and (b) DBD oxidation; (c) and (d) schematic diagrams of oxidation behavior of Ni catalyst.

Above phenomena derived from H_2 -TPR is schematically depicted in Figure 2.8 (c) and (d) that overall bulk Ni crystal is oxidized by DBD CO_2 (shown in red color of terrace), while thermal CO_2 only leads to the partial oxidation (shown in red color of perimeter). Due to the limited area of the perimeter between Ni nanocrystal and Al_2O_3 , the DBD CO_2 could not further enhance Ni oxidation in the perimeter, which is confirmed by the fact that peak (III) in the Figure 2.8 (a) and (b) are almost same (3.0 vs. 4.4 cm^3). Interestingly, the overall oxidation of Ni nanocrystal contributes a new reaction pathway for inhibition of coke formation from CH_4 dehydrogenation, which will be discussed in the next section.

2.6 Plasma-enabled new reaction pathway

Previously, DBD-mediated reaction enhancement mechanism over porous Ni/Al₂O₃ catalysts in MDR was investigated. The total flow rate of CH₄ and CO₂ was 2000 cm³/min with the ratio of $0.5 < (\text{CH}_4/\text{CO}_2) < 2$; the temperature of catalyst and the discharge power were controlled as 600 °C and 85 W respectively [1]. For plasma catalysis, carbon deposition was detected only on the external surface of pellets, where DBD interacts with catalyst rather than internal pores. Such phenomenon proves that both DBD generation and plasma-excited species penetration into the internal pores are inhibited; moreover, carbon deposition in the internal pores could be remarkably prevented by DBD [25]. Similar trend was observed in this work that NiO was formed in the limited region over the external surface (20 μm depth) only when DBD was superimposed: NiO was not detected in the internal pores due to negligible interaction with DBD.

Molecular beam study revealed dissociative chemisorption of CH₄ on metal surface was enhanced by vibrational excitation [60]. The numerical simulation of 1-dimensional streamer propagation demonstrated that the vibrationally excited CH₄ is the most abundant and long-lived species generated by low energy electron impact [61]. Similarly, excited CO₂ and H₂O to the vibrational states are expected to promote heterogeneous catalytic reactions [1]. However, there is an insufficient understanding of the role of vibrationally excited species in plasma catalysis. For DBD, electron density in a narrow filamentary channel is of the order of 10¹⁴ cm⁻³ [62-64]; in contrast, molecule density at standard condition is approximately 10¹⁹ cm⁻³, indicating that a majority part of gas stream is neither ionized nor excited. Consequently, extremely low proportion of ionized and excited species is inadequate to explain the net increase of CH₄ and CO₂ conversion and selectivity change by DBD. In this regard, nonthermal plasma oxidation of Ni to NiO creates critically important step for plasma-enabled synergistic effect.

As schematically shown in Figure 2.9 (a), DBD-excited CO₂, most likely vibrational excitation, would induce Ni oxidation rather than simple adsorption; DBD-excited CO₂ would increase oxygen-containing surface species (i.e. NiO), leading to oxygen-rich surface beyond Langmuir isotherm. Incoming excited CO₂ would carry a few eV internal energy due to the gas phase vibration-to-vibration energy transfer [65, 66], which is the important source of energy for NiO formation. Excited CO₂ may increase adsorption flux; however, ad-CO₂ is eventually desorbed by the equilibrium limitation unless it forms NiO. Moreover, we hypothesize that the DBD-induced nonthermal heating mechanism would play another key role for the promotion of Ni oxidation (Figure 2.9 (b)). Charge recombination and association of radicals on catalyst surface can release energy corresponding to 1–10 eV/molecule. If this excess energy is transferred directly to the adsorbed CO₂, Ni oxidation may be promoted without increasing macroscopic catalyst temperature. This reaction scheme would be explained by nonthermal plasma-mediated Eley-Rideal mechanism, rather than precursor type adsorption enhancement. It is interesting to mention that Raman peaks of Al₂O₃ in Figure 2.6 (a) increased clearly near the surface, implying Al₂O₃ crystallization is promoted by DBD-induced molecular scale heating mechanism. Although nonthermal plasma-induced heating mechanism is commonly accepted in particle growth [67, 68], it has yet to be investigated within the scope of plasma catalysis. In addition, it is critically important issue because effect of DBD is not limited to "excited molecules": penetration of electric field and surface charges into the internal pores is also the important factor to enhance heterogeneous catalyst reactions.

As for MDR, NiO provides the lattice oxygen-rich surface beyond Langmuir isotherm, which has a capability of oxidizing a large flux of ground state CH₄ efficiently (Figure 2.9 (c)); in other words, CH₄ is not necessarily pre-excited. CH₄ is almost fully reacted in the NiO shell (20 μm thickness) and coke formation in the internal pores is prohibited [25]. In the thermal catalysis, however, formation of NiO is negligibly small; the ground state CH₄ can diffuse into

internal pores and deposit coke as previously confirmed [25] (Figure 2.9 (d)). In this reaction regime, primarily role of NiO is a surface lattice oxygen reservoir: meanwhile the catalyst activity of partially oxidized Ni-based catalyst, as well as nonthermal plasma heating mechanism, have not confirmed experimentally yet; these new research subjects are being organized towards the deeper insight into the plasma-mediated catalysis, particularly in MDR, including the identification of intermediate surface species and their reaction dynamics.

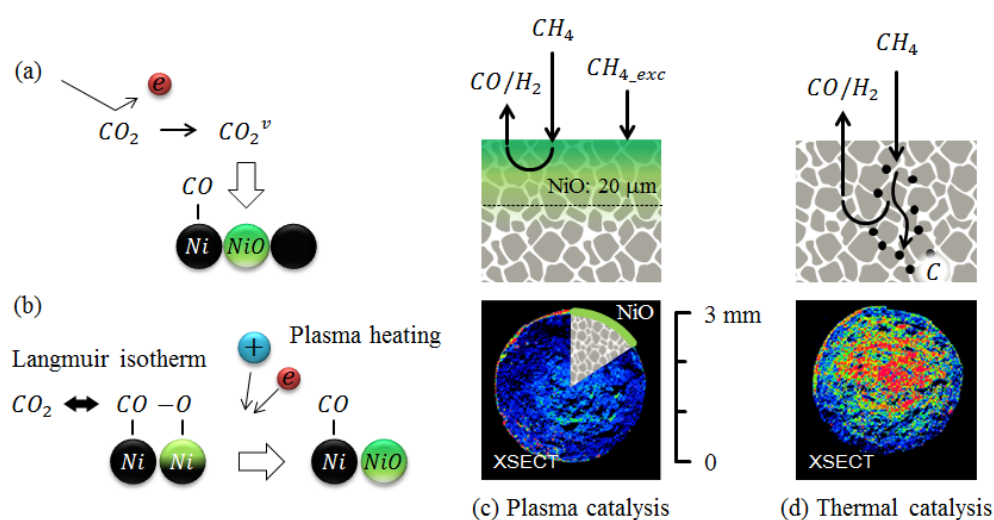


Figure 2.9 (a) NiO formation by DBD-excited CO_2 , (b) Nonthermal plasma heating mechanism, (c) CH_4 conversion within NiO shell having no coke in the internal pores, (d) Thermal catalysis with significant coke formation in the internal pores. Carbon mapping is cited from ref. [25].

2.7 Conclusions

The oxidation behavior of $\text{Ni}/\text{Al}_2\text{O}_3$ catalyst in CO_2 plasma was investigated compared with CO_2 thermal oxidation, aiming for providing new insight into oxidation-reduction cycle of plasma catalysis of methane dry reforming. In addition to temperature programmed reaction spectrometry, the distribution of NiO over the cross-section of catalyst pellets was analyzed by

Raman spectroscopy. Major conclusions were derived as follows:

- (1) In the mixed plasma oxidation with large *SEI*, there are two Ni oxidation pathways: One is the direct oxidation route induced by DBD-excited CO₂. The other is the indirect route due to O₂ which is produced by homogeneous CO₂ dissociation by electron impact. When *SEI* is sufficiently small (< 1 eV/molecule), DBD-enhanced direct oxidation becomes the main oxidation route which significantly oxidizes Ni to NiO.
- (2) Oxidation amount of Ni in the plasma oxidation was much higher than corresponding thermal oxidation within the same temperature range (up to 600°C).
- (3) NiO thin layer was formed in the external surface during plasma oxidation with the thickness of ca. 20 micrometers: both DBD generation and plasma-excited species penetration into the internal pores are inhibited.
- (4) Due to the formation of NiO, catalyst uptakes lattice oxygen beyond thermal equilibrium known as Langmuir isotherm, creating a new reaction pathway via NiO.
- (5) The NiO thin layer drives the oxidation-reduction cycle in the plasma catalysis of MDR, which is effective to CH₄ dehydrogenation, while coke formation is suppressed.
- (6) Formation of NiO in the external surface of spherical pellets was correlated with carbon deposition behavior [25]. Although the reactivity of partially oxidized Ni catalyst is not well understood at the moment, we hypothesize that ground state CH₄ is dehydrogenated almost fully within the 20 μm NiO shell before further diffusion into internal pores.

2.8 References

- [1] S. Kameshima, K. Tamura, R. Mizukami, T. Yamazaki, T. Nozaki, Parametric analysis of plasma-assisted pulsed dry methane reforming over Ni/Al₂O₃ catalyst, *Plasma Processes and Polymers* 14 (2017) 1600096.
- [2] Y.T. Shah, T.H. Gardner, Dry reforming of hydrocarbon feedstocks, *Catalysis Reviews* 56 (2014) 476-536.
- [3] A. Bogaerts, E. Neyts, in: X. Tu, J.C. Whitehead, T. Nozaki (Eds.), *Plasma catalysis: fundamentals and applications*, Springer International Publishing, Cham, 2019, pp. 69-

- [4] A. Rouso, S. Yang, J. Lefkowitz, W. Sun, Y. Ju, Low temperature oxidation and pyrolysis of n-heptane in nanosecond-pulsed plasma discharges, *Proceedings of the Combustion Institute* 36 (2017) 4105-4112.
- [5] S.M. Chun, Y.C. Hong, D.H. Choi, Reforming of methane to syngas in a microwave plasma torch at atmospheric pressure, *Journal of CO₂ Utilization* 19 (2017) 221-229.
- [6] E.C. Neyts, A. Bogaerts, Understanding plasma catalysis through modelling and simulation—a review, *Journal of Physics D: Applied Physics* 47 (2014) 224010.
- [7] S. Kameshima, K. Tamura, Y. Ishibashi, T. Nozaki, Pulsed dry methane reforming in plasma-enhanced catalytic reaction, *Catalysis Today* 256 (2015) 67-75.
- [8] T. Nozaki, K. Okazaki, Non-thermal plasma catalysis of methane: Principles, energy efficiency, and applications, *Catalysis Today* 211 (2013) 29-38.
- [9] Z. Wang, Y. Zhang, E.C. Neyts, X. Cao, X. Zhang, B.W.L. Jang, C.-j. Liu, Catalyst preparation with plasmas: How does it work?, *ACS Catalysis* 8 (2018) 2093-2110.
- [10] X. Fang, J. Lian, K. Nie, X. Zhang, Y. Dai, X. Xu, X. Wang, W. Liu, C. Li, W. Zhou, Dry reforming of methane on active and coke resistant Ni/Y₂Zr₂O₇ catalysts treated by dielectric barrier discharge plasma, *Journal of Energy Chemistry* 25 (2016) 825-831.
- [11] H. Peng, Y. Ma, W. Liu, X. Xu, X. Fang, J. Lian, X. Wang, C. Li, W. Zhou, P. Yuan, Methane dry reforming on Ni/La₂Zr₂O₇ treated by plasma in different atmospheres, *Journal of Energy Chemistry* 24 (2015) 416-424.
- [12] N. Rahemi, M. Haghighi, A.A. Babaluo, S. Allahyari, M.F. Jafari, Syngas production from reforming of greenhouse gases CH₄/CO₂ over Ni–Cu/Al₂O₃ nanocatalyst: Impregnated vs. plasma-treated catalyst, *Energy Conversion and Management* 84 (2014) 50-59.
- [13] L. Di, J. Zhang, X. Zhang, A review on the recent progress, challenges, and perspectives of atmospheric-pressure cold plasma for preparation of supported metal catalysts, *Plasma Processes and Polymers* 15 (2018) 1700234.
- [14] N. Blin-Simiand, P. Tardiveau, A. Risacher, F. Jorand, S. Pasquiers, Removal of 2-heptanone by dielectric barrier discharges – the effect of a catalyst support, *Plasma Processes and Polymers* 2 (2005) 256-262.
- [15] C.-j. Liu, J. Zou, K. Yu, D. Cheng, Y. Han, J. Zhan, C. Ratanatawanate, B.W.L. Jang, Plasma application for more environmentally friendly catalyst preparation, *Pure and Applied Chemistry* 78 (2006) 1227-1238.
- [16] J. Hong, W. Chu, P.A. Chernavskii, A.Y. Khodakov, Cobalt species and cobalt-support interaction in glow discharge plasma-assisted Fischer–Tropsch catalysts, *Journal of Catalysis* 273 (2010) 9-17.
- [17] S. Shang, G. Liu, X. Chai, X. Tao, X. Li, M. Bai, W. Chu, X. Dai, Y. Zhao, Y. Yin, Research on Ni/γ-Al₂O₃ catalyst for CO₂ reforming of CH₄ prepared by atmospheric

- pressure glow discharge plasma jet, *Catalysis Today* 148 (2009) 268-274.
- [18] S. Wang, G.Q. Lu, G.J. Millar, Carbon dioxide reforming of methane to produce synthesis gas over metal-supported catalysts: State of the art, *Energy & Fuels* 10 (1996) 896-904.
 - [19] V.R. Choudhary, B.S. Uphade, A.S. Mamman, Large enhancement in methane-to-syngas conversion activity of supported Ni catalysts due to precoating of catalyst supports with MgO, CaO or rare-earth oxide, *Catalysis Letters* 32 (1995) 387-390.
 - [20] M.G. Gonzalez, M.S. Leguizamon Aparicio, M.A. Ocsachoque, Effect of Rh addition to Ni/MgO-Al₂O₃ catalysts for dry reforming of methane, *Indian Journal of Science and Technology* 10 (2017) 1-9.
 - [21] P.M. Holmblad, J. Wambach, I. Chorkendorff, Molecular beam study of dissociative sticking of methane on Ni(100), *The Journal of Chemical Physics* 102 (1995) 8255-8263.
 - [22] H. Yang, J.L. Whitten, Dissociative chemisorption of CH₄ on Ni(111), *The Journal of Chemical Physics* 96 (1992) 5529-5537.
 - [23] V. Pawar, S. Appari, D.S. Monder, V.M. Janardhanan, Study of the combined deactivation due to sulfur poisoning and carbon deposition during biogas dry reforming on supported Ni catalyst, *Industrial & Engineering Chemistry Research* 56 (2017) 8448-8455.
 - [24] K. Yuan, J.-Q. Zhong, X. Zhou, L. Xu, S.L. Bergman, K. Wu, G.Q. Xu, S.L. Bernasek, H.X. Li, W. Chen, Dynamic oxygen on surface: Catalytic intermediate and coking barrier in the modeled CO₂ reforming of CH₄ on Ni (111), *ACS Catalysis* 6 (2016) 4330-4339.
 - [25] S. Kameshima, R. Mizukami, T. Yamazaki, L.A. Prananto, T. Nozaki, Interfacial reactions between DBD and porous catalyst in dry methane reforming, *Journal of Physics D: Applied Physics* 51 (2018) 114006.
 - [26] D.A. Constantinou, A.M. Efstathiou, The steam reforming of phenol over natural calcite materials, *Catalysis Today* 143 (2009) 17-24.
 - [27] M.C.J. Bradford, M. Albert Vannice, The role of metal-support interactions in CO₂ reforming of CH₄, *Catalysis Today* 50 (1999) 87-96.
 - [28] S.C. Shen, X. Chen, S. Kawi, CO₂ adsorption over Si-MCM-41 materials having basic sites created by postmodification with La₂O₃, *Langmuir* 20 (2004) 9130-9137.
 - [29] L. Qian, Z. Ma, Y. Ren, H. Shi, B. Yue, S. Feng, J. Shen, S. Xie, Investigation of La promotion mechanism on Ni/SBA-15 catalysts in CH₄ reforming with CO₂, *Fuel* 122 (2014) 47-53.
 - [30] O.V. Manoilova, S.G. Podkolzin, B. Tope, J. Lercher, E.E. Stangland, J.-M. Goupil, B.M. Weckhuysen, Surface acidity and basicity of La₂O₃, LaOCl, and LaCl₃ characterized by IR spectroscopy, TPD, and DFT calculations, *The Journal of Physical Chemistry B* 108 (2004) 15770-15781.
 - [31] X.E. Verykios, Catalytic dry reforming of natural gas for the production of chemicals

- and hydrogen, *International Journal of Hydrogen Energy* 28 (2003) 1045-1063.
- [32] J.F. Múnera, S. Irusta, L.M. Cornaglia, E.A. Lombardo, D. Vargas Cesar, M. Schmal, Kinetics and reaction pathway of the CO₂ reforming of methane on Rh supported on lanthanum-based solid, *Journal of Catalysis* 245 (2007) 25-34.
 - [33] K. Pokrovski, K.T. Jung, A.T. Bell, Investigation of CO and CO₂ adsorption on tetragonal and monoclinic zirconia, *Langmuir* 17 (2001) 4297-4303.
 - [34] T. Tabakova, F. Boccuzzi, M. Manzoli, D. Andreeva, FTIR study of low-temperature water-gas shift reaction on gold/ceria catalyst, *Applied Catalysis A: General* 252 (2003) 385-397.
 - [35] D. Cornu, H. Guesmi, J.-M. Krafft, H. Lauron-Pernot, Lewis acido-basic interactions between CO₂ and MgO surface: DFT and DRIFT approaches, *The Journal of Physical Chemistry C* 116 (2012) 6645-6654.
 - [36] B. Mutz, H.W.P. Carvalho, S. Mangold, W. Kleist, J.-D. Grunwaldt, Methanation of CO₂: Structural response of a Ni-based catalyst under fluctuating reaction conditions unraveled by operando spectroscopy, *Journal of Catalysis* 327 (2015) 48-53.
 - [37] B. Mutz, H.W.P. Carvalho, W. Kleist, J.D. Grunwaldt, Dynamic transformation of small Ni particles during methanation of CO₂ under fluctuating reaction conditions monitored by operando X-ray absorption spectroscopy, *Journal of Physics: Conference Series* 712 (2016) 012050.
 - [38] Y. Du, K. Tamura, S. Moore, Z. Peng, T. Nozaki, P.J. Bruggeman, CO(B¹Σ⁺→A¹Π) angstrom system for gas temperature measurements in CO₂ containing plasmas, *Plasma Chemistry and Plasma Processing* 37 (2017) 29-41.
 - [39] R. Snoeckx, A. Bogaerts, Plasma technology – a novel solution for CO₂ conversion?, *Chemical Society reviews* 46 (2017) 5805-5863.
 - [40] I. Belov, J. Vanneste, M. Aghaee, S. Paulussen, A. Bogaerts, Synthesis of micro- and nanomaterials in CO₂ and CO dielectric barrier discharges, *Plasma Processes and Polymers* 14 (2017) 1600065.
 - [41] R. Aerts, W. Somers, A. Bogaerts, Carbon dioxide splitting in a dielectric barrier discharge Plasma: A combined experimental and computational study, *ChemSusChem* 8 (2015) 702-716.
 - [42] T. Butterworth, R. Elder, R. Allen, Effects of particle size on CO₂ reduction and discharge characteristics in a packed bed plasma reactor, *Chemical Engineering Journal* 293 (2016) 55-67.
 - [43] F. Brehmer, S. Welzel, M.C.M. van de Sanden, R. Engeln, CO and byproduct formation during CO₂ reduction in dielectric barrier discharges, *Journal of Applied Physics* 116 (2014) 123303.
 - [44] B. Mutz, M.A. Gänzler, M. Nachtegaal, O. Müller, R. Frahm, W. Kleist, J.-D. Grunwaldt, Surface oxidation of supported Ni particles and its impact on the catalytic performance

- during dynamically operated methanation of CO₂, *Catalysts* 7 (2017) 279.
- [45] L. Foppa, T. Margossian, S.M. Kim, C. Müller, C. Copéret, K. Larmier, A. Comas-Vives, Contrasting the role of Ni/Al₂O₃ interfaces in water–gas shift and dry reforming of methane, *Journal of the American Chemical Society* 139 (2017) 17128-17139.
 - [46] M.-C. Silaghi, A. Comas-Vives, C. Copéret, CO₂ activation on Ni/γ-Al₂O₃ catalysts by first-principles calculations: From ideal surfaces to supported nanoparticles, *ACS Catalysis* 6 (2016) 4501-4505.
 - [47] L.D. Pietanza, G. Colonna, G. D’Ammando, A. Laricchiuta, M. Capitelli, Non equilibrium vibrational assisted dissociation and ionization mechanisms in cold CO₂ plasmas, *Chemical Physics* 468 (2016) 44-52.
 - [48] L.D. Pietanza, G. Colonna, G. D’Ammando, A. Laricchiuta, M. Capitelli, Vibrational excitation and dissociation mechanisms of CO₂ under non-equilibrium discharge and post-discharge conditions, *Plasma Sources Science and Technology* 24 (2015) 042002.
 - [49] N. Mironova-Ulmane, A. Kuzmin, I. Sildos, M. Pärs, Polarisation dependent Raman study of single-crystal nickel oxide, *Central European Journal of Physics* 9 (2011) 1096-1099.
 - [50] A. Aminzadeh, H. Sarikhani-fard, Raman spectroscopic study of Ni/Al₂O₃ catalyst, *Spectrochimica Acta Part A: Molecular and Biomolecular Spectroscopy* 55 (1999) 1421-1425.
 - [51] H.-H. Kim, Y. Teramoto, N. Negishi, A. Ogata, A multidisciplinary approach to understand the interactions of nonthermal plasma and catalyst: A review, *Catalysis Today* 256 (2015) 13-22.
 - [52] J.R. Roth, *Industrial Plasma Engineering, Volume 1 Principles*, Institute of Physics publishing, London, 1995.
 - [53] Q.-Z. Zhang, A. Bogaerts, Propagation of a plasma streamer in catalyst pores, *Plasma Sources Science and Technology* 27 (2018) 035009.
 - [54] Y.-R. Zhang, K. Van Laer, E.C. Neyts, A. Bogaerts, Can plasma be formed in catalyst pores? A modeling investigation, *Applied Catalysis B: Environmental* 185 (2016) 56-67.
 - [55] C. Tendero, C. Tixier, P. Tristant, J. Desmaison, P. Leprince, Atmospheric pressure plasmas: A review, *Spectrochimica Acta Part B: Atomic Spectroscopy* 61 (2006) 2-30.
 - [56] D.B. Go, D.A. Pohlman, A mathematical model of the modified Paschen’s curve for breakdown in microscale gaps, *Journal of Applied Physics* 107 (2010) 103303.
 - [57] K.M. Bal, E.C. Neyts, Modelling molecular adsorption on charged or polarized surfaces: a critical flaw in common approaches, *Physical Chemistry Chemical Physics* 20 (2018) 8456-8459.
 - [58] S. Jiang, Y. Lu, S. Wang, Y. Zhao, X. Ma, Insight into the reaction mechanism of CO₂ activation for CH₄ reforming over NiO-MgO: A combination of DRIFTS and DFT study, *Applied Surface Science* 416 (2017) 59-68.

- [59] K. Sutthiumporn, S. Kawi, Promotional effect of alkaline earth over Ni–La₂O₃ catalyst for CO₂ reforming of CH₄: Role of surface oxygen species on H₂ production and carbon suppression, *International Journal of Hydrogen Energy* 36 (2011) 14435-14446.
- [60] E. Dombrowski, E. Peterson, D. Del Sesto, A.L. Utz, Precursor-mediated reactivity of vibrationally hot molecules: Methane activation on Ir(111), *Catalysis Today* 244 (2015) 10-18.
- [61] T. Nozaki, N. Muto, S. Kado, K. Okazaki, Dissociation of vibrationally excited methane on Ni catalyst: Part 1. Application to methane steam reforming, *Catalysis Today* 89 (2004) 57-65.
- [62] U. Kogelschatz, Dielectric-barrier discharges: Their history, discharge physics, and industrial applications, *Plasma Chemistry and Plasma Processing* 23 (2003) 1-46.
- [63] T. Nozaki, Y. Miyazaki, Y. Unno, K. Okazaki, Energy distribution and heat transfer mechanisms in atmospheric pressure non-equilibrium plasmas, *Journal of Physics D: Applied Physics* 34 (2001) 3383-3390.
- [64] T. Nozaki, Y. Unno, K. Okazaki, Thermal structure of atmospheric pressure non-equilibrium plasmas, *Plasma Sources Science and Technology* 11 (2002) 431-438.
- [65] A. Bogaerts, T. Kozák, K. van Laer, R. Snoeckx, Plasma-based conversion of CO₂: current status and future challenges, *Faraday Discussions* 183 (2015) 217-232.
- [66] G.J. van Rooij, D.C.M. van den Bekerom, N. den Harder, T. Minea, G. Berden, W.A. Bongers, R. Engeln, M.F. Graswinckel, E. Zoethout, M.C.M. van de Sanden, Taming microwave plasma to beat thermodynamics in CO₂ dissociation, *Faraday Discussions* 183 (2015) 233-248.
- [67] H.R. Maurer, H. Kersten, On the heating of nano- and microparticles in process plasmas, *Journal of Physics D: Applied Physics* 44 (2011) 174029.
- [68] N.J. Kramer, R.J. Anthony, M. Mamunuru, E.S. Aydil, U.R. Kortshagen, Plasma-induced crystallization of silicon nanoparticles, *Journal of Physics D: Applied Physics* 47 (2014) 075202.

Chapter 3: CO₂ activation behavior over La-Ni/Al₂O₃ catalyst

This chapter is adapted from an unpublished work:

Zunrong Sheng, Hyun-Ha Kim, Shuiliang Yao, Tomohiro Nozaki, Physical Chemistry Chemical Physics, in press, DOI: 10.1039/d0cp03127e.

3.1 Abstract

For a better fundamental understanding of the plasma and catalyst interfacial phenomena, we employed in situ diffuse reflectance infrared Fourier transform spectroscopy (DRIFTS) under plasma-on conditions to elucidate the nonthermal plasma-enabled reaction enhancement mechanisms. Compared with thermal catalysis, plasma-activated CO₂ shows a 1.7-fold enhancement for bidentate (1560 and 1290 cm⁻¹) and monodentate carbonate (1425 and 1345 cm⁻¹) formation on La. Moreover, new peaks of bicarbonate (1655 cm⁻¹) and bridge carbonate (1720 cm⁻¹) were formed due to nonthermal plasma interactions. Ex situ CO₂-TPD study after plasma- and thermal-activated CO₂ treatment further confirmed that plasma-activated CO₂ enhances bidentate and monodentate carbonate generation with a 1.5-fold promotion at high temperature (500 °C). XRD and EDS analyses suggest that atomic-scale interaction between CO₂-La and CH_x-Ni is possible over the complex La-Ni-Al oxide; vibrationally excited CO₂ (CO₂^{vib.})-induced carbonates provide the key to enhancing the overall performance of CH₄ dry reforming at low temperature.

3.2 Introduction

Methane dry reforming (MDR) shows significant benefits regarding biogas upgrading to syngas and reducing greenhouse gas emissions because of accessible and abundant feedstocks [1]. The product syngas is a key chemical feedstock for Fischer-Tropsch upgrading towards high-value products [2, 3]. However, MDR is an intensive endothermic reaction that requires high-temperature thermal energy [4]. From the perspective of thermodynamics study, spontaneous reaction could not occur at low temperature because a negative Gibbs free energy is required to meet the reaction entropy [5]. To reduce the light-off temperature, nonthermal plasma-assisted reforming is practical with additional electron energy input, which has been demonstrated in some studies [6-8].

From the perspective of kinetic studies, nonthermal plasma-assisted catalysis could reduce the energy barrier by plasma-derived excited species [9-15]. The CH_4 dissociative chemisorption on nickel is considered to be the rate-determining step that controls the overall reaction rate. Our previous study demonstrated that dissociative CH_4 activation on La-modified $\text{Ni}/\text{Al}_2\text{O}_3$ catalyst was clearly promoted under the influence of nonthermal plasma [16], which is explained by a decrease in the apparent activation energy via vibrationally excited CH_4 [17]. However, very few works on plasma-assisted in situ surface reactions have been reported.

Regarding the metal-support catalyst (e.g., $\text{Ni}/\text{Al}_2\text{O}_3$) for MDR, metal nanocrystals are the active sites for CH_4 activation. The interface between the metal and metal oxide is commonly considered the active site for CO_2 activation [18, 19], which inevitably leads to limited active sites for CO_2 activation. Due to the lack of efficient activation sites for plasma-activated CO_2 uptake, a synergistic effect with plasma was not observed clearly in the $\text{Ni}/\text{Al}_2\text{O}_3$ system [20]. To solve this problem, a promoter and high basic support are expected to improve the performance of CO_2 uptake on the catalyst. The principle is that the basic metal oxide contributes an oxygen anion (O^{2-}) to CO_2 to form a surface carbonate species (CO_3^{2-}), which

has been investigated by diffuse reflectance infrared Fourier transform spectroscopy (DRIFTS) on various promoters or supports in thermal catalytic reactions, e.g., CaO [21], TiO₂ [22], La₂O₃ [23-27], ZrO₂ [28], CeO₂ [29], and MgO [30]. Regarding the plasma-assisted reaction, Ref. [31] demonstrates that the Ni-La₂O₃/MgAl₂O₄ catalyst increases the basicity of the catalyst to enhance the chemisorption of CO₂ and further enhance CH₄ activation. However, evidence for an in situ plasma-assisted reaction was not provided. Recently, Xu *et al* reported nonthermal plasma-induced promotion of carbonate, bicarbonate and formate species over a Ru-Mg-Al catalyst surface by in situ DRIFTS-MS study of CO₂ hydrogenation [32]. Other analogical works also presented clear surface activation by plasmas of carbonate and formate species over metal-organic frameworks [33, 34]. A different principle for CO₂ uptake on a catalyst is that surface oxygen vacancies enhance dissociative electron attachment, where CO₂ adsorption becomes easier than that at defect-free sites [35, 36]. In this case, plasma enhances the splitting of CO₂ into CO and O anions, and then oxygen is fixed in vacancies as “lattice oxygen” [37]. However, regarding CH₄ and CO₂ involved in plasma-catalyst studies, such a surface mechanism has only been found in CO₂ splitting [35, 38] and CH₄ dissociative chemisorption [39] until now. In this case, the plasma-enhanced interaction mechanism between multiple adsorbed species is still unclear.

To understand the surface intermediates induced by plasma-activated CO₂ on La-modified Ni/Al₂O₃ catalyst, in situ DRIFTS study, under the presence of nonthermal plasma (hereafter in situ plasma-DRIFTS), was employed to reveal CO₂ activation at 200 °C. The ex situ CO₂-TPD study was carried out after plasma-activated CO₂ treatment at 500 °C to investigate the amount of adsorbed species compared with that of thermal-activated CO₂ treatment. XRD and EDS were employed to analyze the detailed structure of the catalyst. To reveal the surface reaction between CO₂- and CH₄-derived species, high-temperature in situ DRIFTS without plasma was carried out for a more in-depth mechanistic study.

3.3 Experimental section

3.3.1 In situ DRIFTS

In situ DRIFTS (PerkinElmer Frontier) was employed with a liquid nitrogen-cooled mercury cadmium telluride (MCT) detector. Helium was introduced into the cell as a balance gas with a flow rate of 60 or 100 mL/min. CH₄/CO₂ was introduced into the cell at 10 mL/min. Two DRIFTS cells were employed: (I) a custom-built plasma-DRIFTS cell (Figure 3) and (II) a high-temperature regular cell without plasma. Figure 3.1 (a) schematically depicts (I) where a high-voltage needle electrode was located above the catalyst powder (ca. 1 mm gap) to generate a DBD (dielectric barrier discharge)-type nonthermal plasma between the needle and catalyst powder. A ground electrode was located at the periphery of the ceramic catalyst holder, which worked as a dielectric barrier. The plasma was generated at a 50 Hz sinusoidal high voltage of 5.5 kV. Figure 3.1 (b) shows the overall view of the plasma-DRIFTS cell without a catalyst. The top view in Figure 3.1 (c) shows details of the cell with a 0.1 gram mashed catalyst pellet with a mean diameter of ca. 1 mm. Figure 3.1 (d) and (e) shows the emission from the plasma in the visible spectrum. The temperature of the catalyst was maintained at 200 °C during the experiment. The temperature cannot be further increased due to the limitation of heat tolerance: the sealing materials around electrodes could not work more than 200 °C. At high temperatures, the gas leakage will occur due to the disorder of sealing materials.

The high-temperature cell (II) has a structure similar to that of the plasma-DRIFTS cell without electrodes, and the temperature of the catalyst can be increased up to 600 °C. Ca. 0.03 g of the powder catalyst filled the holder. Before the experiment, all the catalysts were pretreated by H₂/Ar (100/1000 mL/min) for 60 min at 600 °C in the experimental setup shown in Chapter 2, the same conditions used in our previous works [16, 20]. All the measurements were taken at atmospheric pressure. The 26-scan accumulation was carried out with a resolution of 4 cm⁻¹ for all the spectral recordings.

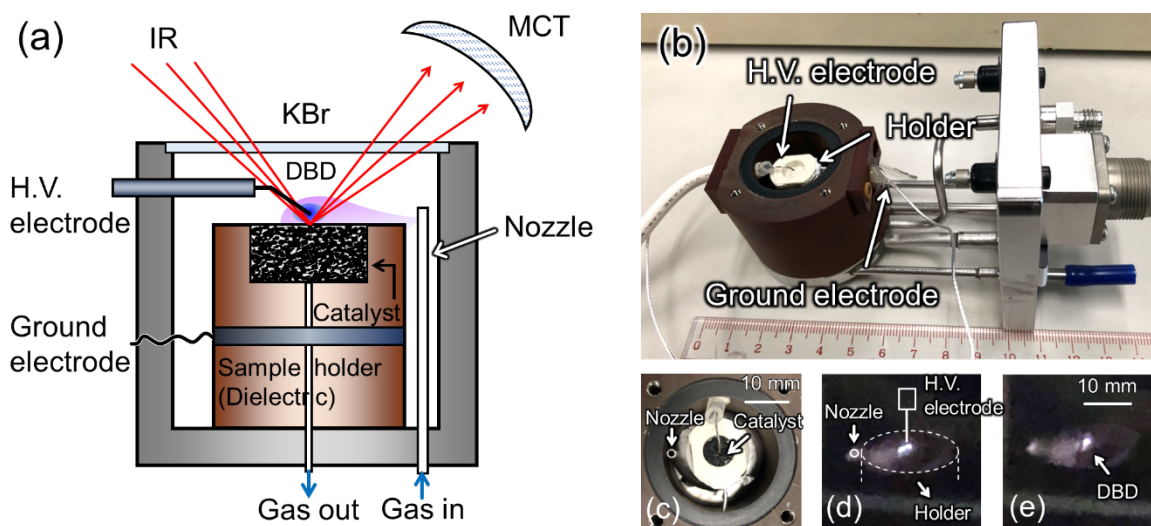


Figure 3.1 In situ plasma-DRIFTS cell: (a) schematic diagram; (b) overall view; (c) top-view; and (d) and (e) emissions from plasma.

3.3.2 Ex situ CO₂-TPD

CO₂-TPD (temperature programmed desorption) was performed in a quartz tube reactor, a temperature controllable furnace and a quadrupole mass spectrometer (QMS, Prisma-100; Pfeiffer Vacuum GmbH), which are depicted in Chapter 2 [16, 40]. The catalyst pellet of Ni/Al₂O₃ or La-Ni/Al₂O₃ (ca. 11 g) was pretreated by H₂/Ar flow (100/1000 mL/min) at 600 °C for 60 min. CO₂-TPD was carried out based on two control groups at 500 °C with 500 cm³/min CO₂ flow: plasma CO₂ treatment ($SEI = 2.7$ eV/molecule) and thermal CO₂ treatment. After 60 min of thermal/plasma CO₂ treatment, a rapid cooling program was carried out with a rate of ca. 50 °C/min in an argon atmosphere to avoid surface species desorption during rapid cooling. After the catalyst temperature reached 25 °C, the CO₂-TPD started with 1000 cm³/min Ar at a heating rate of 10 °C/min.

3.4 Catalyst characterization

La-modified Ni/Al₂O₃ catalyst was employed in this study, with the main components of Ni (11 wt%), La (3 wt%) and an Al₂O₃ support, referred to herein as “La-Ni/Al₂O₃”. Another catalyst of 12 wt% Ni/Al₂O₃ was employed in this study as a control group without La modification, referred to herein as “Ni/Al₂O₃”. A schematic model of Ni/Al₂O₃ is given in another reference [5]. The X-Ray Diffraction (XRD, Mini Flex 600) was employed with Cu-K α X-ray source (40 kV and 15 mA) at a step width of 0.02° (2 θ) and scan speed of 5° min⁻¹. The XRD analysis of the Ni/Al₂O₃ and La-Ni/Al₂O₃ after thermal H₂ reduction is presented in Figure 3.2 (a) and (b). The peaks of 44.6 and 51.9 corresponded to Ni(111) and Ni(200), respectively. The mean size (L) of the Ni nanocrystals in Ni/Al₂O₃ was estimated to be 29.0 nm by Scherrer's equation (Eq 3.1) based on the average of 8 measurements, where $K=0.94$, $\lambda=1.54$ Å, and the FWHM is the full width at half maximum. Other peaks were assigned to Al₂O₃. In the XRD pattern of La-Ni/Al₂O₃, La₂O₃ was not identified, which has been reported for some La-added catalysts [24, 41-43]. In Figure 3.2 (b), LaNiAl₁₁O₁₉ was identified based on 2 θ of 32.1, 34.0, 36.1, 39.3, 42.7, 44.9, 58.5, 60.0 and 67.2° (cf. Figure 3.2 (c)), illustrating that Ni and La were located on the atomic scale as a complex La-Ni-Al oxide. The structure of LaNiAl₁₁O₁₉ is presented in ref [44, 45]. Similarly, the mean size of the Ni crystal of La-Ni/Al₂O₃ was estimated to be 10.8 nm by Scherrer's equation. In this case, Ni nanocrystals and Ni in the La-Ni-al oxide complex coexisted. Moreover, Figure 3.2 (b) shows peaks of MgAl₂O₄ with negligible intensity (0.7 wt% Mg) because Mg-containing dispersing agent was used during the catalyst preparation.

$$L = \frac{K\lambda}{FWHM \cos \theta} \quad \text{Eq 3.1}$$

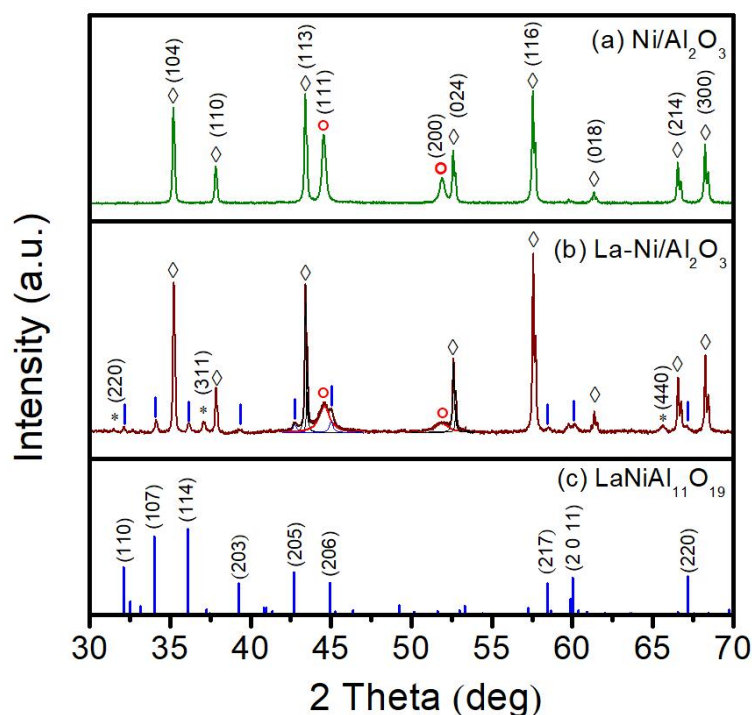


Figure 3.2 XRD patterns of (a) Ni/Al₂O₃, (b) La-Ni/Al₂O₃, and (c) LaNiAl₁₁O₁₉,

where ○ Ni; | LaNiAl₁₁O₁₉; ◇ Al₂O₃; and * MgAl₂O₄.

High-angle annular dark-field STEM (HAADF-STEM) and energy-dispersive X-ray spectroscopy (EDS) (Bruker Nano GmbH) were employed to obtain the nanoparticle images and element distributions. Catalyst pellets were crushed by mechanical milling. Figure 3.3 (a) and (b) shows HAADF images and Ni mapping of Ni/Al₂O₃, where Ni is identified as distributed nanocrystals in the observation field. The results for La-Ni/Al₂O₃ are shown in Figure 3.3 (c-f), which presents a different distribution behavior than Ni/Al₂O₃. First, both Ni nanocrystals and fine Ni (in LaNiAl₁₁O₁₉) are detectable in Figure 3.3 (e), showing a higher and more uniform Ni dispersion than Figure 3.3 (b). Second and more importantly, Ni and La overlap in Figure 3.3 (f) due to the combination of (d) and (e). For bimetallic or polymetallic catalysts, the proximity of components is critical for determining the cooperative effect [46]. Synergistic interaction between the active species on Ni and La is highly likely over the La-Ni-Al oxide complex.

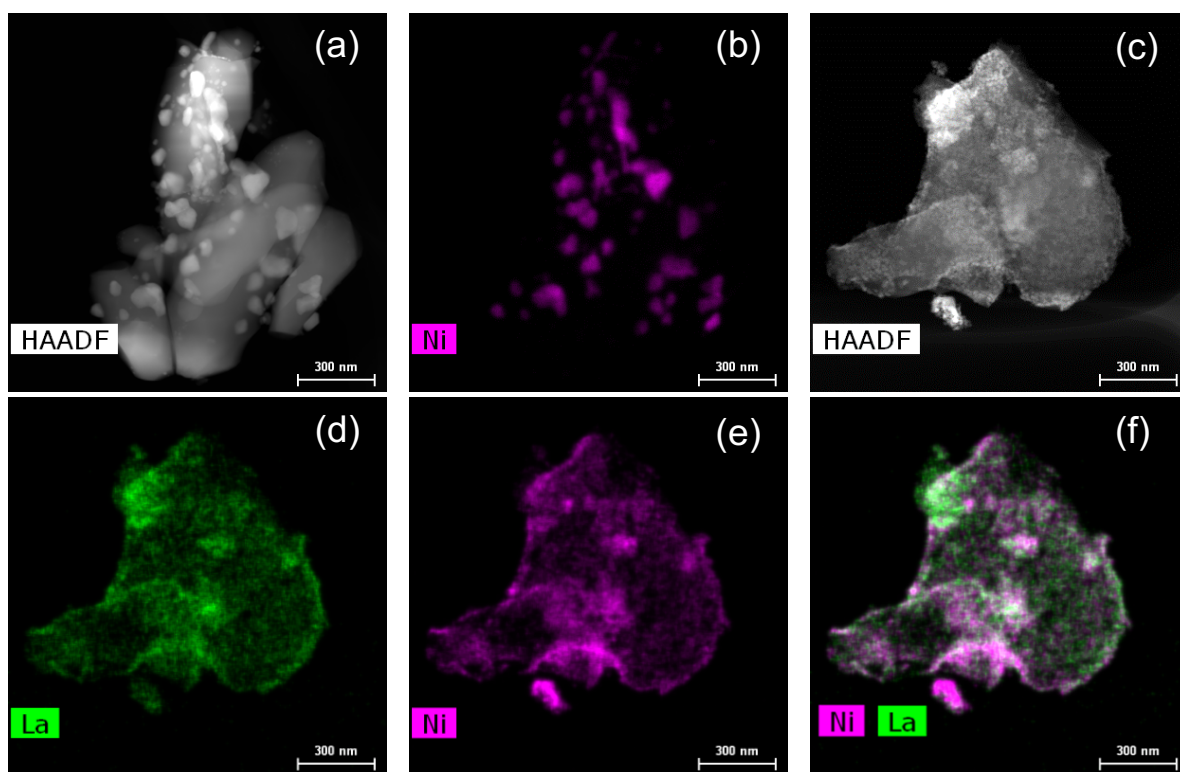


Figure 3.3 HAADF images and elemental maps: (a & b) Ni/Al₂O₃; (c-f) La-Ni/Al₂O₃.

3.5 Enhanced carbonate formation by nonthermal plasma

3.5.1 In situ plasma-DFITS study

Figure 3.4 (a) and (b) shows the spectra from the in situ plasma-DRIFTS cell operated at 200 °C with Ni/Al₂O₃ and La-Ni/Al₂O₃, respectively. Spectrum (a1) in Figure 3.4 (a) shows the CO₂ activation on Ni/Al₂O₃. The peak in the range of 2260 to 2400 cm⁻¹ is assigned to gas phase CO₂. The broad peaks centered at 1340 and 1600 cm⁻¹ are assigned to the generated carbonate species [47, 48], which is presumably on the interface between the Ni nanocrystals and Al₂O₃ [40, 41, 49, 50], where adsorption sites are limited due to the small area of the interface. As a result, the absorbance intensity of the peaks of carbonate species is not too strong in the spectrum (a1), showing clear evidence that the interface between Ni and Al₂O₃ supplies weak active sites for CO₂ activation. Spectrum (a2) is obtained after 30 min of treatment with plasma-activated CO₂. Except for the plasma-induced electromagnetic noise, the intensity of the carbonate peaks is not enhanced. Spectrum (a3) is taken when the CO₂ flow and plasma are

turned off simultaneously, showing that plasma does not enhance the surface species on Ni/Al₂O₃.

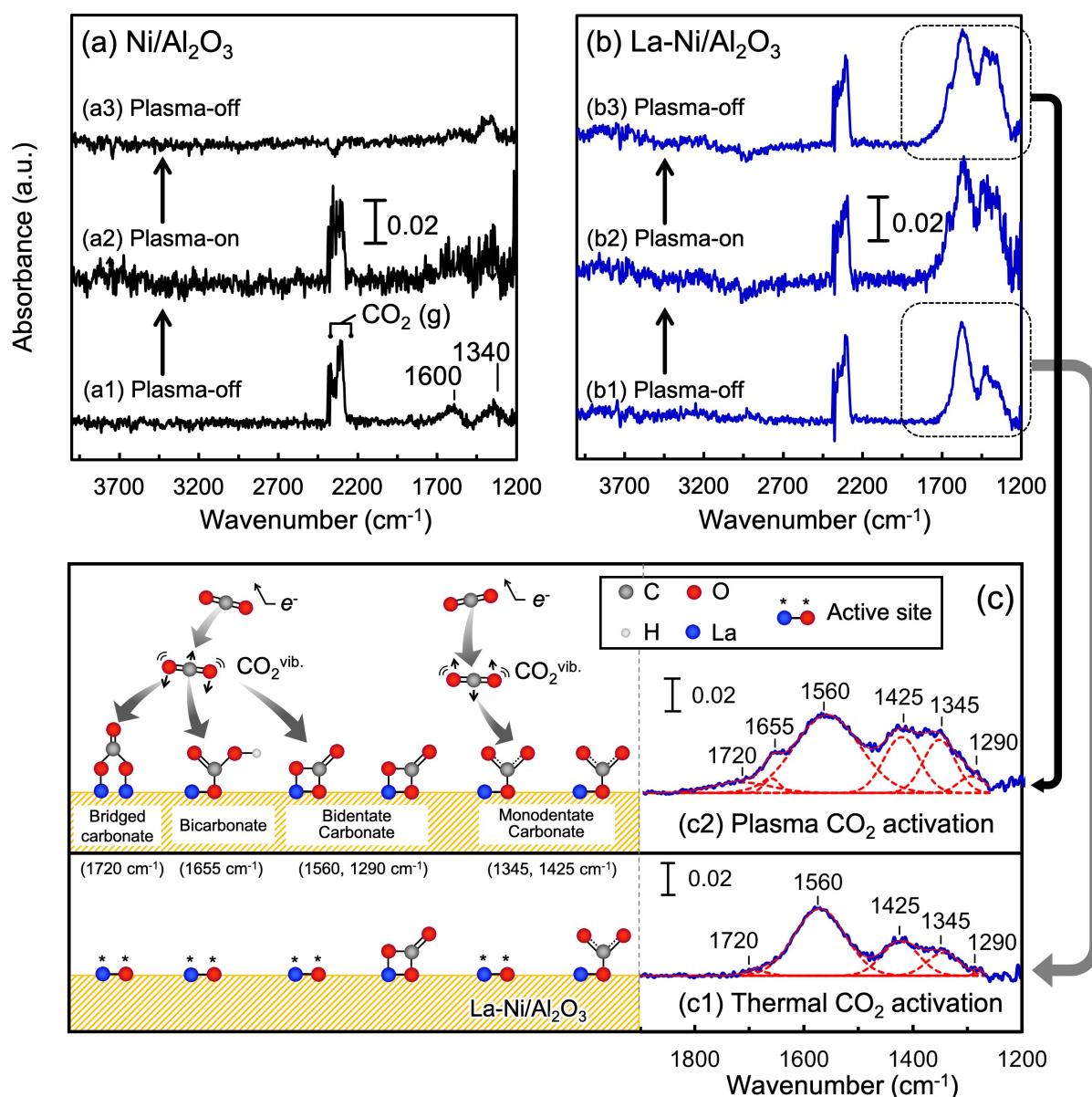
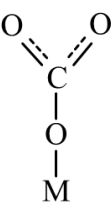
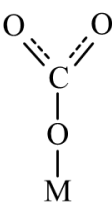
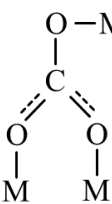
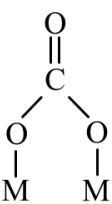
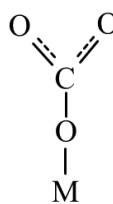


Figure 3.4 In situ plasma-DRIFTS spectra of CO₂ activation at 200 °C. (a) Ni/Al₂O₃: (a1) 30 min treatment with CO₂/He (9 vol%, 110 mL/min), (a2) 30 min plasma treatment with CO₂/He, and (a3) plasma halt under He flow. (b) La- Ni/Al₂O₃: (b1) 40 min treatment with CO₂/He, (b2) 30 min plasma treatment with CO₂/He, and (b3) plasma halt under CO₂/He flow. (c) shows the vibrationally excited CO₂-enhanced mechanism of carbonate formation accompanied by magnified spectra (c1 and c2).

The spectra in Figure 3.4 (b) represent La-Ni/Al₂O₃. The overlapping peaks between 1200 and 1800 cm⁻¹ are assigned to several carbonate species [50, 51]. The details of all the carbonate species coordinated with La are summarized in Table 3.1. Spectrum (b1) is obtained when the CO₂ activation reaches steady state with 40 min of treatment. Figure 4 (c1) shows magnified carbonate peaks, which are deconvoluted to several peaks as the red dashed curves. The peaks centered at 1560 cm⁻¹ and 1290 cm⁻¹ are assigned to bidentate carbonate [41]. The peaks at 1425 and 1345 cm⁻¹ are assigned to monodentate carbonate [41, 52, 53]. A broad peak at 1720 cm⁻¹ is assigned to bridged carbonate [21] at a negligible intensity. The intensity of the carbonate peaks is much stronger than that of Ni/Al₂O₃ in spectrum (a1), illustrating that complex La-Ni-Al oxide works as the active site for CO₂ activation.

Table 3.1 Carbonate structure over the La-Ni/Al₂O₃ catalyst and vibration assignments of the DRIFTS peaks (*M represents the coordination metal, lanthanum in this study).

Species	Monodentate carbonate	Bidentate carbonate	Polydentate carbonate	Bridged carbonate	Bicarbonate
Schematic structure*					
Vibration mode and wavenumber (cm ⁻¹)	$\nu_{as} \text{OCO}$ at 1425 cm ⁻¹ $\nu_s \text{OCO}$, at 1345 cm ⁻¹	$\nu_{as} \text{OCO}$ at 1560 cm ⁻¹ $\nu_s \text{OCO}$, at 1290 cm ⁻¹	$\nu_{as} \text{CO}_3$ at 1500 cm ⁻¹	$\nu \text{C=O}$ at 1720 cm ⁻¹	$\nu_{as} \text{OCO}$ at 1655 cm ⁻¹ νOH at 3600-3800 cm ⁻¹
Reference	[41, 52, 53]	[41]	[23, 25]	[21, 25]	[23, 26, 30, 53-55]

The spectrum (b2) in Figure 3.4 (b) is obtained under plasma treatment. The intensity of carbonate peaks increases significantly in the presence of nonthermal plasma. Spectrum (b3) is obtained after plasma treatment and is magnified in Figure (c2). The bidentate and monodentate carbonate contents are clearly increased by plasma: the total areas of peaks of bidentate carbonate (1560 and 1290 cm^{-1}) and monodentate carbonate (1425 and 1345 cm^{-1}) in plasma-activated CO_2 activation (Figure (c2)) show an approximately 1.7-fold enhancement compared to those of thermal-activated CO_2 (Figure (c1)). In addition, bridged carbonate (1720 cm^{-1}) [21] and bicarbonate (also called hydrogen carbonate) (1655 cm^{-1}) [23, 53, 54] are generated. The broad peak centered at 3800 cm^{-1} may be attributed to the OH band of bicarbonate [26, 30, 55]. The surface hydrogen species from catalyst pretreatment (thermal H_2 reduction) may contribute the hydrogen species for generating bicarbonate with plasma.

Electron collision kinetic analysis reveals that the production of vibrationally excited species in nonthermal plasma is the dominant reaction pathway rather than dissociation and ionization when the reduced electric field (E/N) is lower than 700 Td [16]. R3.1 shows that vibrationally excited molecules are produced due to low energy electron impact with a rate constant k_v . Here, A represents a neutral molecule such as CO_2 or CH_4 . The rate expression for the production of vibrationally excited species is formulated in Eq 3.2, where N_A and N_e represent the number densities of neutral molecules and electrons, respectively. Our previous study demonstrated that the production of vibrationally excited CO_2 and CH_4 is 40-150 times greater than the electron number density, as shown in Eq 3.3 [16, 56]. In other words, a single electron produces 40 to 150 times more vibrationally excited molecules. Therefore, the vibrationally excited species is the most abundant species in the nonthermal plasma environment. A molecular beam study revealed that vibrational excitation is effective at promoting the reaction between the incident molecule and catalyst surface [57], contributing to the enhanced surface coverage of adsorbed species by vibrational energy redistribution [58,

59]. The vital role of vibrational excitation is also indicated in homogeneous plasma-induced CO₂ splitting studies [38, 60]. Based on the above experimental and theoretical works, we highlight that plasma-induced vibrationally excited CO₂ plays a key role in enhanced carbonate formation over La-Ni/Al₂O₃, which is schematically depicted in Figure 3.4 (c): (c1) shows that active sites in complex La-Ni-Al oxide are occupied by carbonates in thermal-activated CO₂ activation. When plasma-activated CO₂ treatment starts, electron-induced vibrationally excited CO₂ has a stronger interaction with unoccupied active sites. Consequently, bridged carbonate and bicarbonate are generated, and the formation of monodentate and bidentate carbonate is enhanced, as shown in Figure (c2).



$$r_v = \frac{dN_A^v}{dt} = k_v N_A N_e \quad \text{Eq 3.2}$$

$$N_A^v = (40 - 150) N_e \quad \text{Eq 3.3}$$

3.5.2 Ex situ CO₂-TPD study

The above DRIFTS experiments present carbonate generation behavior at 200 °C due to the limitation of the heat tolerance of the plasma-DRIFTS chamber. To investigate carbonate generation at high temperatures, CO₂-TPD (temperature programmed desorption) was carried out after CO₂ treatment with and without plasma. The results for La-Ni/Al₂O₃ are shown in Figure 3.5 (A). All the curves between 300 and 600 °C are deconvoluted into several peaks, and the fitting curve (an orange dotted line) overlaps with the original spectrum. The curve (a) in Figure 3.5 is the CO₂-TPD pattern after thermal CO₂ treatment. The assignment of peaks I-IV are summarized in Table 3.2. Peaks I and II are attributed to the desorption of the bidentate

carbonate adsorbed on the interface between Ni and Al₂O₃ (hereafter Al₂O₃) and the La in the La-Ni-Al oxide complex (hereafter La) [41], respectively. The desorption temperature of carbonate at different sites can be distinguished based on the premise that La oxide is more basic than Al₂O₃ [61-63], which leads to a higher desorption temperature. Peaks III and IV at higher temperatures correspond to the desorption of monodentate carbonate adsorbed on Al₂O₃ and La, respectively [41].

The TPD patterns of Ni/Al₂O₃ are shown in Figure 3.5 (B), where the CO₂ desorption (signal of m/e=44) is very weak in patterns (a) and (b), illustrating that the carbonate generation over Ni/Al₂O₃ is intrinsically weak. Plasma-enhanced synergism is not observed clearly for Ni/Al₂O₃ catalysts, which correlates well with the DRIFTS experiments shown in Figure 3.4 (a). A comparison between the TPD peaks of La-Ni/Al₂O₃ and Ni/Al₂O₃ shows that peaks I (I') and III (III') are common features of these two catalysts, which are related to Al₂O₃. However, peaks II and IV are unique features of La-Ni/Al₂O₃.

Compared with thermal CO₂ treatment, peaks II, III and IV of La-Ni/Al₂O₃ are enhanced after plasma CO₂ treatment in Figure 3.5 (A), which corresponds well with the DRIFTS results at low temperature. Here, we conclude that plasma CO₂ at high and low temperatures can enhance carbonate generation over La-Ni/Al₂O₃.

Table 3.2. The assignment of peaks I–IV for La-Ni/Al₂O₃.

Peak	I	II	III	IV
Temperature (°C)	375	400	460	500
Carbonate type	Bidentate	Bidentate	Monodentate	Monodentate
Active site	Al ₂ O ₃	La	Al ₂ O ₃	La

Remarks: Al₂O₃ represents the interface between Ni and Al₂O₃, and La represents complex La-Ni-Al oxide.

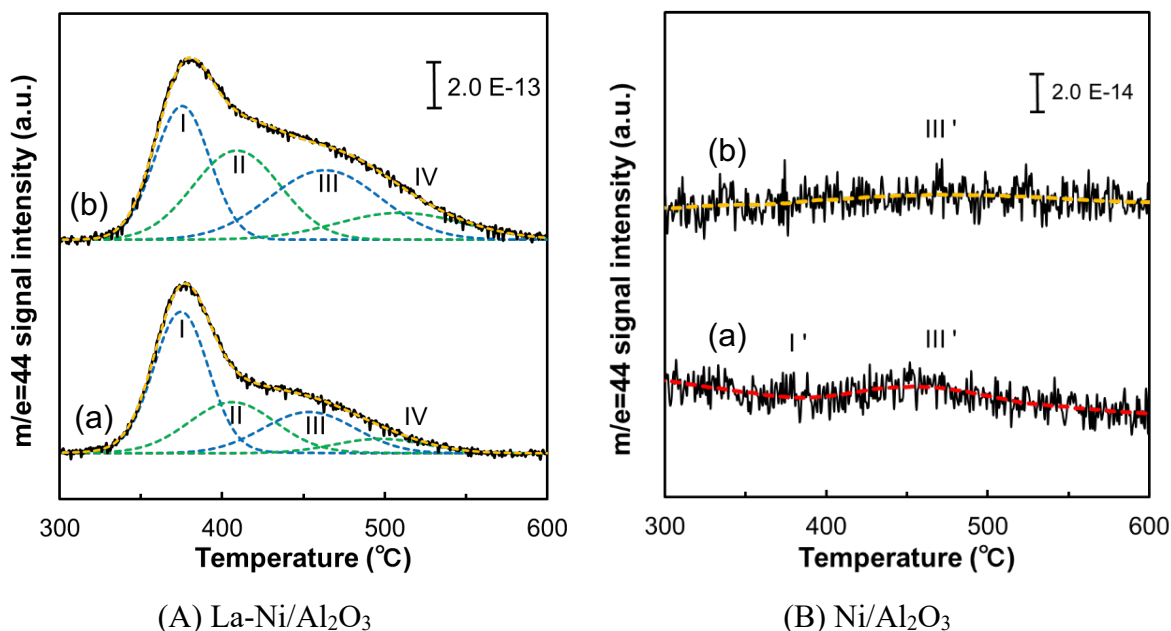


Figure 3.5 CO₂-TPD patterns of (A) La-Ni/Al₂O₃ and (B) Ni/Al₂O₃ after 500 °C treatment: (a) thermally activated CO₂ and (b) plasma-activated CO₂. The CO₂ flow rate was 500 mL/min at 10 kPa. The heating rate was 10 °C/min.

3.6 Carbonate-induced reaction pathway

3.6.1 In situ DRIFTS study

The carbonate generation over La-Ni/Al₂O₃ is clearly enhanced by CO₂ plasma. Moreover, Ni/Al₂O₃ without La is inert for carbonate generation. In this section, only La-Ni/Al₂O₃ is studied to reveal the reaction enhancement mechanism via carbonates for methane dry reforming.

First, low-temperature DRIFTS cell was employed where the CH₄ was introduced with CO₂ over the carbonate containing La-Ni/Al₂O₃. In spectrum (a) in Figure 3.6, the gas phase CH₄ was detected as the peaks at 1304 cm⁻¹ and 3015 cm⁻¹. The product CO (g), the intermediate species CH_x^{*} (in the range of 2800 to 3000 cm⁻¹ [64, 65]) and CH_xO^{*} (1750 cm⁻¹ [66-68]) were not detected, illustrating that CH₄ dehydrogenation did not occur at 200 °C. In spectrum (b), plasma was employed. The peak at 1560 cm⁻¹ (bidentate carbonate) was enhanced

slightly by plasma. However, the missing CH_x^* ($x=1-3$), CH_xO^* and CO (g) imply that plasma at 200 °C could not induce CH_4 chemisorption and dehydrogenation. Besides, the intensity of bidentate carbonate peak at 1560 cm^{-1} was enhanced with plasma-on (spectrum (b)) refers to the scale bar (red color), which corresponds with the results in section 3.5.1.

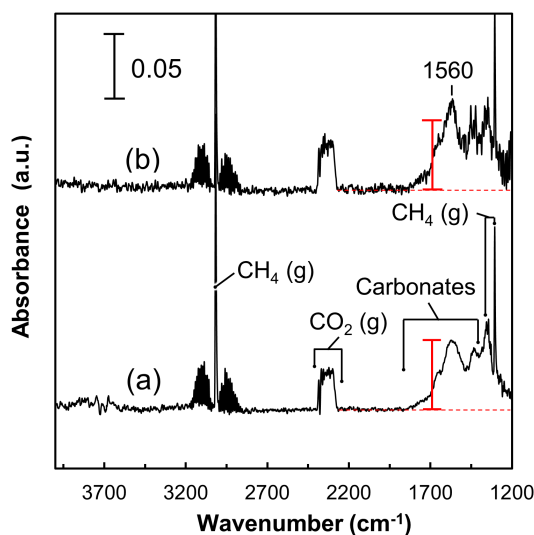


Figure 3.6 DRIFTS spectra for $\text{CO}_2/\text{CH}_4/\text{He}$ (8.3 vol%, 120 mL/min) activation over $\text{La-Ni}/\text{Al}_2\text{O}_3$ at 200 °C in plasma-DRIFTS cell: (a) plasma-off; (b) plasma-on.

Because CH_4 activation is impractical in low-temperature DRIFTS cells even with plasma, the plasma-enhanced surface reaction mechanism is further supported by the high-temperature DRIFTS study at 600 °C. The spectrum at 1 min in Figure 3.7 (a) for CO_2 treatment shows two broad peaks centered at 1560 and 1354 cm^{-1} , which are assigned to bidentate and monodentate carbonates, respectively. Then, the CO_2 flow is switched to CH_4 at 2 min. Gas phase CH_4 is detected as peaks at 1304 , 1354 and 3015 cm^{-1} (not shown). With continuous CH_4 flow, the peak at 1560 cm^{-1} shifts gradually to 1500 cm^{-1} between 2 and 4 min because the bidentate carbonate (1560 cm^{-1}) is gradually consumed, while polydentate carbonate (1500 cm^{-1}) [23, 69] becomes dominant, indicating that bidentate carbonate reacts primarily with CH_4 -derived species. Additionally, a weak broad band centered at 1750 cm^{-1} appears when CH_4 is introduced,

which is assigned to the C=O stretching vibration in surface CH_xO^* ($x=1-3$) species [66-68], and it is expected as the intermediate species for generating CO and H_2 [70, 71]. Here, the adsorbed species are denoted by “*”. In this case, the CH_x^* from CH_4 dehydrogenation is continuously oxidized by CO_3^{2-} (bidentate carbonate) to generate CH_xO^* before complete dehydrogenation of carbon occurs. The peaks of gas phase CO (2113 and 2176 cm^{-1} [72]) are detectable at 4.5 min accompanied by an enhanced CH_xO^* band (1750 cm^{-1}), indicating that the successful production of CH_xO^* leads to syngas (CO and H_2) generation.

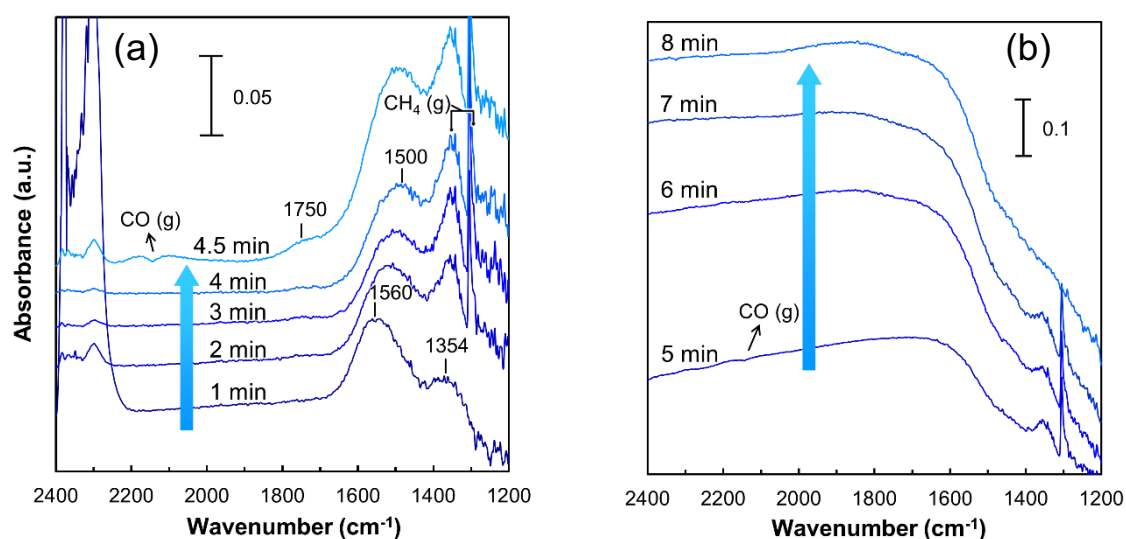


Figure 3.7 In situ DRIFTS spectra of CH_4 flows to carbonate-containing La-Ni/ Al_2O_3 at 600 °C in high-temperature cell (plasma-off). 1 min: $\text{CO}_2/\text{He}=14$ vol %, 70 mL/min; 2-7 min: $\text{CH}_4/\text{He}=14$ vol %, 70 mL/min; 8 min: $\text{He}=60$ mL/min.

In Figure 3.7 (b), the bands of product CO (g) became weak at 5 min due to the carbonate species being consumed, which is confirmed by the fact that all the carbonate peaks (between 1200 and 1800 cm^{-1}) disappear. The lack of carbonates leads to the oxidation-reduction behavior of Ni [22], which is attributed to the baseline shift from 5 to 7 min. The transparency difference between the reduced and oxidized samples, as well as the oxidation-reduction

behavior will be discussed in section 3.7. CH₄ is dehydrogenated continuously to coke [50] after the carbonates are fully consumed. The CH₄ flow is turned off at 8 min, and all the carbonate bands disappear.

3.6.2 Relationship between carbonate formation and CH₄ conversion

Table 3.3 summarizes the CH₄ conversion from our previous works, as well as the amounts of carbonates obtained from the DRIFTS and CO₂-TPD results in this work. For Ni/Al₂O₃, CH₄ conversion is not increased under plasma reforming compared with that of thermal reforming, indicating that the plasma-induced synergism for CH₄ conversion is negligible. For La-Ni/Al₂O₃, plasma reforming shows a 1.5-fold enhancement in CH₄ conversion compared with thermal reforming. Such plasma-induced synergism can be explained by the enhancement in carbonate generation, showing a 1.5-1.8 times enhancement compared with that of thermal treatment according to DRIFTS and CO₂-TPD experiments.

Ni nanoparticles work as the active sites for CH₄ dissociative chemisorption, and the complex La-Ni-Al oxide supplies peculiar active sites for CO₂ activation. The Ni weight percent of Ni/Al₂O₃ (12% wt.) is higher than that of La-Ni/Al₂O₃ (11% wt.). Moreover, approximately 2% wt. Ni contributes to LaNiAl₁₁O₁₉, while only 9% wt. Ni nanoparticles are estimated in La-Ni/Al₂O₃. Therefore, the CH₄ conversion with La-Ni/Al₂O₃ is lower than that with Ni/Al₂O₃. Additionally, significant coking is observed in Ni/Al₂O₃ [20] because Ni/Al₂O₃ is more reactive for CH₄, leading to much smaller CO selectivity than that of the La-Ni/Al₂O₃ catalyst [16, 20].

Table 3.3 Comparison of the CH₄ conversion and amount of carbonate generated

CH ₄ conversion in MDR			Amount of carbonate generated	
Reference	Kameshima <i>et al</i>	Sheng <i>et al</i>	DRIFTS results in	CO ₂ -TPD
	[20] ^(*a)	[16] ^(*b)	Figure 3.4 (c) ^(*c)	results in
				Figure 3.5 (I) ^(*d)
Catalyst	Ni/Al ₂ O ₃		La-Ni/Al ₂ O ₃	
Unit	mL/min	mL/min	Areal intensity of absorbance (-)	Areal intensity of desorbed- CO ₂ (-)
Thermal	450	141	8.3	5.6
Plasma	450	204	14.9	8.3
Gain	1	1.5	1.8	1.5

(*a) Catalyst temperature = 600 °C; flow rate of CH₄/CO₂ = 1000 mL/min; catalyst weight =14 g.

(*b) Catalyst temperature = 600 °C; flow rate of CH₄/CO₂ = 500 mL/min; catalyst weight =11 g.

(*c) Areal intensity of absorbance from DRIFTS was calculated by integration of absorbance intensity (a.u.) with wavenumber (cm⁻¹).

(*d) Areal intensity of desorbed-CO₂ from CO₂-TPD was calculated by integration of current intensity of m/z=44 (a.u.) with time (min).

3.6.3 Reaction mechanism of plasma-enhanced MDR

The plasma-enhanced reaction pathways over La-Ni/Al₂O₃ are explained based on the Langmuir-Hinshelwood mechanism, which are schematically illustrated in Figure 3.8. First, CH₄ is dissociatively chemisorbed on Ni as CH₃^{*} and H^{*} (R3.2), followed by consecutive dehydrogenation of adsorbed CH₃^{*} to fragments (CH_x^{*}) (R3.3). Additionally, as an acidic

species, CO₂ is adsorbed and activated on La because the La in the La-Ni-Al oxide complex supports a basic site contributing anionic oxygen (O²⁻) to adsorbed CO₂ for surface covalent carbonate species (CO₃²⁻) formation (R3.4). At the initial stage of reforming, vibrationally excited CH₄ and CO₂ enhance the interaction with catalysts, contributing to the increased amount of surface species.

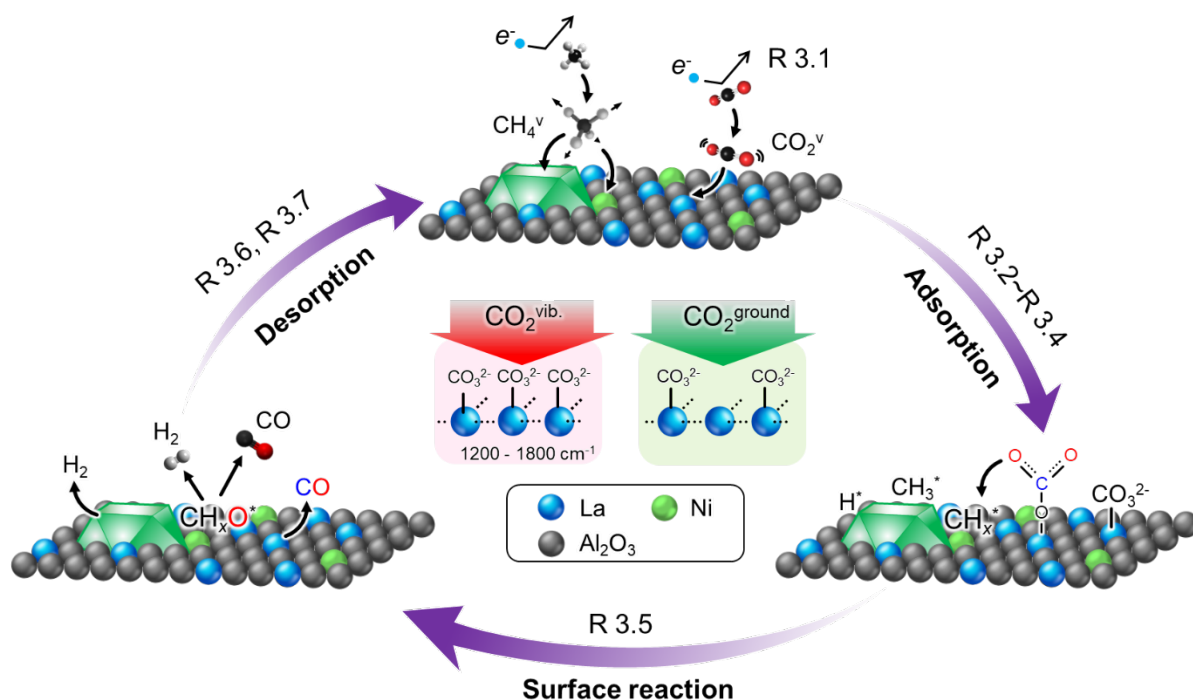


Figure 3.8 Plasma enhanced mechanism over La-Ni/Al₂O₃. Plasma induced reaction pathways (R3.1) is defined in section 3.5.1.

In the second stage of reforming, carbonate species (CO₃²⁻) oxidize CH_x^{*} (x=1-3) quickly on adjacent Ni to form CH_xO^{*} (R3.5), and successful production of CH_xO^{*} leads to syngas (CO and H₂) production (R3.6 and R3.7): as a result, active sites of Ni for CH₄ adsorption are

regenerated. In this case, complete dehydrogenation of CH_3^* to carbon, i.e., coking, is inhibited. More carbonate generation by plasma-activated CO_2 is expected to accelerate the surface reaction (R3.5) by increasing the surface coverage of carbonate. As a result, a promoted CH_4 conversion in plasma-assisted reforming is observed, as summarized in Table 3.3.



Likewise, plasma-activated CH_4 is anticipated to promote dissociative chemisorption over Ni sites. However, CH_x^* fragments need to react with carbonate species, and the active sites must be regenerated for the successive CH_4 conversion to syngas. This is presumably the reason that the interaction between plasma and $\text{Ni}/\text{Al}_2\text{O}_3$ is weak without La.

3.7 Oxidation-reduction behavior of La-Ni/ Al_2O_3

Chapter 2 has confirmed the oxidation-reduction behavior of Ni catalysts by Raman spectroscopy and optical microscopy [13]. In this chapter, it was found that the oxidation-reduction behavior enables a change in the transparency of La-Ni/ Al_2O_3 catalyst. The transmittance spectra (Figure 3.9 (I)) were directly obtained from background measurement in DRIFTS experiment, showing that oxidized and reduced La-Ni/ Al_2O_3 samples have different transmittance spectrum due to the different transparency of Ni (a) and NiO (b). The absorbance spectra could be obtained by Eq 3.4 (Beer's law) based on the transmittance spectra in the background measurement.

$$A(\nu) = 2 - \log(\%T(\nu)) \quad \text{Eq 3.4}$$

Here, A and $\%T$ represent the absorbance and percent transmittance, respectively. ν represents

the wavenumber (cm^{-1}). The absorbance spectra of La-Ni/ Al_2O_3 (thermal H_2 reduced sample) and La-NiO/ Al_2O_3 (thermal CO_2 oxidized sample) are shown in Figure 3.9 (II) (a) and (b), respectively. The spectrum (a) of the reduced sample shows an increase in the profile compared with that of the oxidized sample in the range of $1500\sim 4000\text{ cm}^{-1}$, as well as $600\sim 800\text{ cm}^{-1}$, indicating that the absorbance of the infrared signal increases in the case of the H_2 -reduced sample (i.e., La-Ni/ Al_2O_3). It should be noted that a strong absorbance band is observed in the range of $800\sim 1500\text{ cm}^{-1}$, which is subtracted as background.

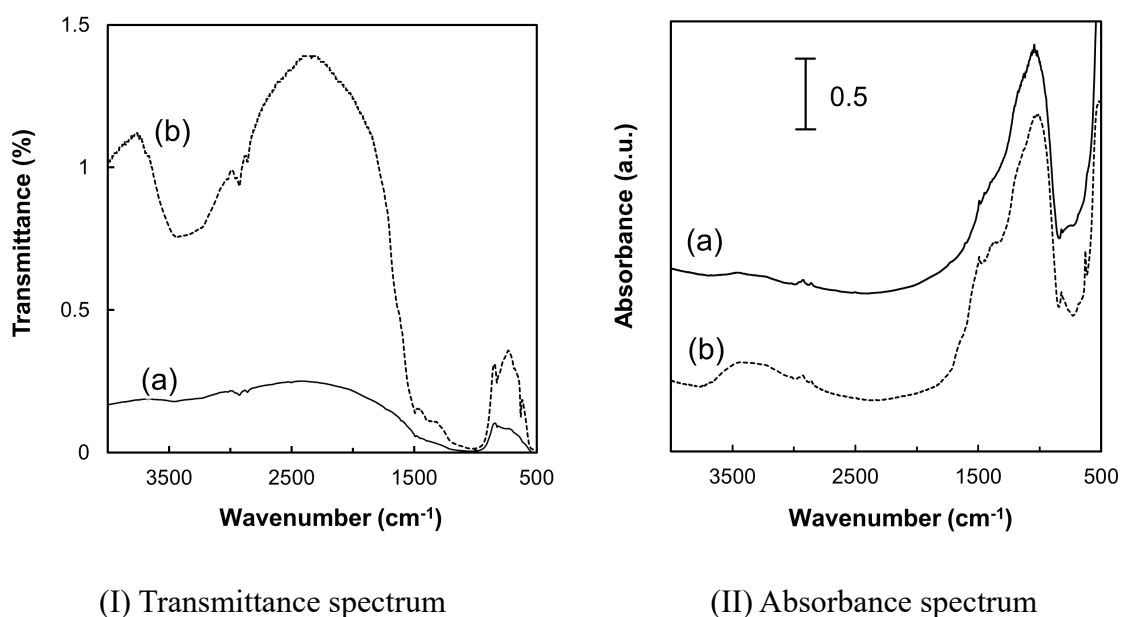


Figure 3.9 Transmittance (I) and absorbance (II) spectrum of (a) La-Ni/ Al_2O_3 and (b) La-NiO/ Al_2O_3 under He flow (100 mL/min) at 600 °C in high-temperature cell.

In Figure 3.10, the spectrum recorded at 1 min shows carbonate species ($1200\sim 1600\text{ cm}^{-1}$). Ni nanocrystals were simultaneously oxidized by thermal CO_2 to NiO. When the H_2 flowed to the DRIFTS cell from 5 min to 15 min instead of CO_2 , the baseline lifted upwards, which was attributed to NiO reduction by H_2 . Carbonates (between 1200 and 1600 cm^{-1}) were consumed at 5 min and gradually disappeared after 10 min. A weak OH^* band (3700 cm^{-1}) was

detected at 5 min in the inset figure. This indicates that OH^* species are the intermediate product when surface hydrogen reacts with carbonates [31] because the decomposition of H_2 easily forms adsorbed H species on Ni [50, 73, 74]. The bands of gas phase H_2O (1250 to 2000 cm^{-1} and 3500 to 4000 cm^{-1}) were not clearly detectable, suggesting that H_2O may not be produced via the reduction of NiO or carbonates. After 15 min, CO_2 was introduced instead of H_2 , and then the baseline “turned back” to oxidized conditions at 30 min with carbonate peaks, which was similar to the spectrum at 1 min.

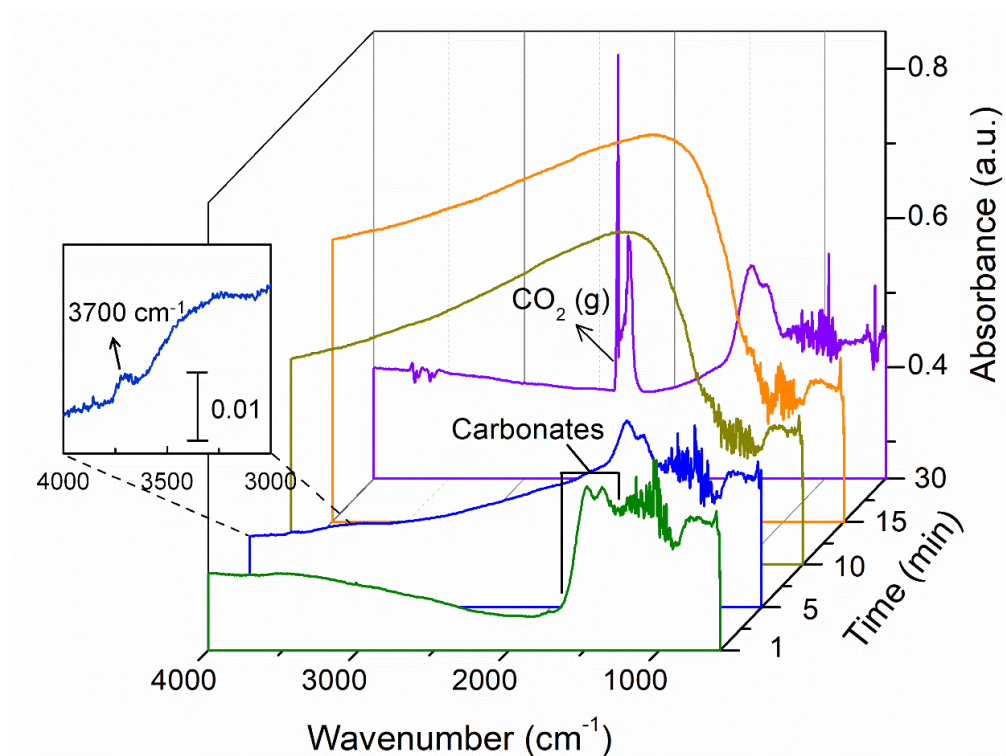


Figure 3.10 DRIFT spectra of oxidation-reduction behavior on $\text{La-Ni/Al}_2\text{O}_3$ at $600\text{ }^\circ\text{C}$ in high-temperature cell: 1 min: oxidized catalyst with CO_2/He (9 vol.%, 110 mL/min) treatment; 5-15 min: reduced catalyst with H_2/He (9 vol.%, 110 mL/min) treatment; 30 min: re-oxidized catalyst with CO_2/He (9 vol.%, 110 mL/min) treatment.

3.8 Conclusion

Nonthermal plasma can enhance CO₂ activation on La, leading to more surface carbonate species formation than with thermal catalysis. Moreover, bicarbonate and bridge carbonate can be generated by plasma treatment. Due to the characteristics of the neighboring distribution on the atomic scale between Ni and La in the La-Ni-Al oxide complex, the CO₂-La-derived carbonate species can oxidize CH_x^{*} on Ni to generate syngas. The synergism of plasma-assisted reforming is explained by the plasma-enhanced surface carbonate generation: more surface carbonates contribute to a higher surface coverage of CO₂. The faster surface reaction between CH_x^{*} species and carbonates leads to higher CH₄ conversion in plasma-assisted methane dry reforming. We would like to point out that activation of CH₄ into vibrational states should also play a vital role; however, co-reactants, i.e., plasma-activated CO₂, that form surface carbonates are necessary to maximize plasma catalysis.

3.9 References

- [1] S.N.B. Villadsen, P.L. Fosbøl, I. Angelidaki, J.M. Woodley, L.P. Nielsen, P. Møller, The potential of biogas; the solution to energy storage, *ChemSusChem* 12 (2019) 2147-2153.
- [2] R.G. Grim, A.T. To, C.A. Farberow, J.E. Hensley, D.A. Ruddy, J.A. Schaidle, Growing the bioeconomy through catalysis: A review of recent advancements in the production of fuels and chemicals from syngas-derived oxygenates, *ACS Catalysis* 9 (2019) 4145-4172.
- [3] P.J. Woolcock, R.C. Brown, A review of cleaning technologies for biomass-derived syngas, *Biomass and Bioenergy* 52 (2013) 54-84.
- [4] S. Liu, L.R. Winter, J.G. Chen, Review of Plasma-assisted catalysis for selective generation of oxygenates from CO₂ and CH₄, *ACS Catalysis* 10 (2020) 2855-2871.
- [5] Z. Sheng, S. Kameshima, K. Sakata, T. Nozaki, Plasma-enabled dry methane reforming, in: N. Britun, T. Silva (Eds.), *Plasma Chemistry and Gas Conversion*, IntechOpen, London, pp. 37-57.
- [6] X. Wang, Y. Gao, S. Zhang, H. Sun, J. Li, T. Shao, Nanosecond pulsed plasma assisted dry reforming of CH₄: The effect of plasma operating parameters, *Applied Energy* 243 (2019) 132-144.
- [7] L. Wang, Y. Yi, C. Wu, H. Guo, X. Tu, One-step reforming of CO₂ and CH₄ into high-value liquid chemicals and fuels at room temperature by plasma-driven catalysis,

Angewandte Chemie 56 (2017) 13679-13683.

- [8] S. Kameshima, R. Mizukami, T. Yamazaki, L.A. Prananto, T. Nozaki, Interfacial reactions between DBD and porous catalyst in dry methane reforming, *Journal of Physics D: Applied Physics* 51 (2018) 114006.
- [9] S. Xu, S. Chansai, C. Stere, B. Inceesungvorn, A. Goguet, K. Wangkawong, S.F.R. Taylor, N. Al-Janabi, C. Hardacre, P.A. Martin, X. Fan, Sustaining metal–organic frameworks for water–gas shift catalysis by non-thermal plasma, *Nature Catalysis* 2 (2019) 142-148.
- [10] S. K. P. Veerapandian, N. De Geyter, J.-M. Giraudon, J.-F. Lamonier, R. Morent, The use of zeolites for VOCs abatement by combining non-thermal plasma, adsorption, and/or catalysis: A Review, *Catalysts* 9 (2019).
- [11] J.C. Whitehead, Plasma–catalysis: the known knowns, the known unknowns and the unknown unknowns, *Journal of Physics D: Applied Physics* 49 (2016) 243001.
- [12] E.C. Neyts, A. Bogaerts, Understanding plasma catalysis through modelling and simulation—a review, *Journal of Physics D: Applied Physics* 47 (2014) 224010.
- [13] J. Kim, D.B. Go, J.C. Hicks, Synergistic effects of plasma-catalyst interactions for CH₄ activation, *Physical chemistry chemical physics : PCCP* 19 (2017) 13010-13021.
- [14] H.L. Chen, H.M. Lee, S.H. Chen, Y. Chao, M.B. Chang, Review of plasma catalysis on hydrocarbon reforming for hydrogen production—Interaction, integration, and prospects, *Applied Catalysis B: Environmental* 85 (2008) 1-9.
- [15] E.C. Neyts, K. Ostrikov, M.K. Sunkara, A. Bogaerts, Plasma catalysis: synergistic effects at the nanoscale, *Chemical Reviews* 115 (2015) 13408-13446.
- [16] Z. Sheng, K. Sakata, Y. Watanabe, S. Kameshima, H.-H. Kim, S. Yao, T. Nozaki, Factors determining synergism in plasma catalysis of biogas at reduced pressure, *Journal of Physics D: Applied Physics* 52 (2019) 414002.
- [17] Z. Sheng, Y. Watanabe, H.-H. Kim, S. Yao, T. Nozaki, Plasma-enabled mode-selective activation of CH₄ for dry reforming: First touch on the kinetic analysis, *Chemical Engineering Journal* 399 (2020) 125751.
- [18] L. Foppa, T. Margossian, S.M. Kim, C. Müller, C. Copéret, K. Larmier, A. Comas-Vives, Contrasting the role of Ni/Al₂O₃ interfaces in water–gas shift and dry reforming of methane, *Journal of the American Chemical Society* 139 (2017) 17128-17139.
- [19] M.-C. Silaghi, A. Comas-Vives, C. Copéret, CO₂ activation on Ni/ γ -Al₂O₃ catalysts by first-principles calculations: From ideal surfaces to supported nanoparticles, *ACS Catalysis* 6 (2016) 4501-4505.
- [20] S. Kameshima, K. Tamura, R. Mizukami, T. Yamazaki, T. Nozaki, Parametric analysis of plasma-assisted pulsed dry methane reforming over Ni/Al₂O₃ catalyst, *Plasma Processes and Polymers* 14 (2017) 1600096.
- [21] D.A. Constantinou, A.M. Efstathiou, The steam reforming of phenol over natural calcite materials, *Catalysis Today* 143 (2009) 17-24.

- [22] M.C.J. Bradford, M. Albert Vannice, The role of metal–support interactions in CO₂ reforming of CH₄, *Catalysis Today* 50 (1999) 87-96.
- [23] S.C. Shen, X. Chen, S. Kawi, CO₂ adsorption over Si-MCM-41 materials having basic sites created by postmodification with La₂O₃, *Langmuir* 20 (2004) 9130-9137.
- [24] L. Qian, Z. Ma, Y. Ren, H. Shi, B. Yue, S. Feng, J. Shen, S. Xie, Investigation of La promotion mechanism on Ni/SBA-15 catalysts in CH₄ reforming with CO₂, *Fuel* 122 (2014) 47-53.
- [25] O.V. Manoilova, S.G. Podkolzin, B. Tope, J. Lercher, E.E. Stangland, J.-M. Goupil, B.M. Weckhuysen, Surface acidity and basicity of La₂O₃, LaOCl, and LaCl₃ characterized by IR spectroscopy, TPD, and DFT calculations, *The Journal of Physical Chemistry B* 108 (2004) 15770-15781.
- [26] X.E. Verykios, Catalytic dry reforming of natural gas for the production of chemicals and hydrogen, *International Journal of Hydrogen Energy* 28 (2003) 1045-1063.
- [27] J.F. Múnera, S. Irusta, L.M. Cornaglia, E.A. Lombardo, D. Vargas Cesar, M. Schmal, Kinetics and reaction pathway of the CO₂ reforming of methane on Rh supported on lanthanum-based solid, *Journal of Catalysis* 245 (2007) 25-34.
- [28] K. Pokrovski, K.T. Jung, A.T. Bell, Investigation of CO and CO₂ adsorption on tetragonal and monoclinic zirconia, *Langmuir* 17 (2001) 4297-4303.
- [29] T. Tabakova, F. Boccuzzi, M. Manzoli, D. Andreeva, FTIR study of low-temperature water-gas shift reaction on gold/ceria catalyst, *Applied Catalysis A: General* 252 (2003) 385-397.
- [30] D. Cornu, H. Guesmi, J.-M. Krafft, H. Lauron-Pernot, Lewis acido-basic interactions between CO₂ and MgO surface: DFT and DRIFT approaches, *The Journal of Physical Chemistry C* 116 (2012) 6645-6654.
- [31] A.H. Khoja, M. Tahir, N.A. Saidina Amin, Evaluating the performance of a Ni catalyst supported on La₂O₃-MgAl₂O₄ for dry reforming of methane in a packed bed dielectric barrier discharge plasma reactor, *Energy & Fuels* 33 (2019) 11630-11647.
- [32] S. Xu, S. Chansai, Y. Shao, S. Xu, Y.-c. Wang, S. Haigh, Y. Mu, Y. Jiao, C.E. Stere, H. Chen, X. Fan, C. Hardacre, Mechanistic study of non-thermal plasma assisted CO₂ hydrogenation over Ru supported on MgAl layered double hydroxide, *Applied Catalysis B: Environmental* 268 (2020) 118752.
- [33] H. Chen, Y. Mu, Y. Shao, S. Chansai, H. Xiang, Y. Jiao, C. Hardacre, X. Fan, Nonthermal plasma (NTP) activated metal–organic frameworks (MOFs) catalyst for catalytic CO₂ hydrogenation, *AIChE Journal* 66 (2020) e16853.
- [34] R. Vakili, R. Gholami, C.E. Stere, S. Chansai, H. Chen, S.M. Holmes, Y. Jiao, C. Hardacre, X. Fan, Plasma-assisted catalytic dry reforming of methane (DRM) over metal-organic frameworks (MOFs)-based catalysts, *Applied Catalysis B: Environmental* 260 (2020) 118195.

- [35] G. Chen, V. Georgieva, T. Godfroid, R. Snyders, M.-P. Delplancke-Ogletree, Plasma assisted catalytic decomposition of CO₂, *Applied Catalysis B: Environmental* 190 (2016) 115-124.
- [36] B. Ashford, Y. Wang, L. Wang, X. Tu, in: X. Tu, J.C. Whitehead, T. Nozaki (Eds.), *Plasma Catalysis: Fundamentals and Applications*, Springer International Publishing, Cham, 2019, pp. 271-307.
- [37] K. Yuan, J.-Q. Zhong, X. Zhou, L. Xu, S.L. Bergman, K. Wu, G.Q. Xu, S.L. Bernasek, H.X. Li, W. Chen, Dynamic oxygen on surface: Catalytic intermediate and coking barrier in the modeled CO₂ reforming of CH₄ on Ni (111), *ACS Catalysis* 6 (2016) 4330-4339.
- [38] D. Mei, X. Zhu, C. Wu, B. Ashford, P.T. Williams, X. Tu, Plasma-photocatalytic conversion of CO₂ at low temperatures: Understanding the synergistic effect of plasma-catalysis, *Applied Catalysis B: Environmental* 182 (2016) 525-532.
- [39] S. Huygh, E.C. Neyts, Adsorption of C and CH_x radicals on anatase (001) and the influence of oxygen vacancies, *The Journal of Physical Chemistry C* 119 (2015) 4908-4921.
- [40] Z. Sheng, S. Kameshima, S. Yao, T. Nozaki, Oxidation behavior of Ni/Al₂O₃ catalyst in nonthermal plasma-enabled catalysis, *Journal of Physics D: Applied Physics* 51 (2018) 445205.
- [41] K. Li, X. Chang, C. Pei, X. Li, S. Chen, X. Zhang, S. Assabumrungrat, Z.-J. Zhao, L. Zeng, J. Gong, Ordered mesoporous Ni/La₂O₃ catalysts with interfacial synergism towards CO₂ activation in dry reforming of methane, *Applied Catalysis B: Environmental* 259 (2019) 118092.
- [42] K. Sutthiumporn, S. Kawi, Promotional effect of alkaline earth over Ni–La₂O₃ catalyst for CO₂ reforming of CH₄: Role of surface oxygen species on H₂ production and carbon suppression, *International Journal of Hydrogen Energy* 36 (2011) 14435-14446.
- [43] W. Mo, F. Ma, Y. Ma, X. Fan, The optimization of Ni–Al₂O₃ catalyst with the addition of La₂O₃ for CO₂–CH₄ reforming to produce syngas, *International Journal of Hydrogen Energy* 44 (2019) 24510-24524.
- [44] M. Gasperin, M.C. Saine, A. Kahn, F. Laville, A.M. Lejus, Influence of M²⁺ ions substitution on the structure of lanthanum hexaaluminates with magnetoplumbite structure, *Journal of Solid State Chemistry* 54 (1984) 61-69.
- [45] R.T. Downs, M. Hall-Wallace, The American mineralogist crystal structure database, *American Mineralogist* 88, (2003) 247-250.
- [46] A. Tou, H.-H. Kim, H. Einaga, Y. Teramoto, A. Ogata, Ozone-assisted catalysis of CO: In situ Fourier transform IR evidence of the cooperative effect of a bimetallic Ag-Pd catalyst, *Chemical Engineering Journal* 355 (2019) 380-389.
- [47] K.K. Bando, K. Sayama, H. Kusama, K. Okabe, H. Arakawa, In-situ FT-IR study on CO₂ hydrogenation over Cu catalysts supported on SiO₂, Al₂O₃, and TiO₂, *Applied Catalysis*

- A: General 165 (1997) 391-409.
- [48] A. Karelovic, P. Ruiz, Improving the hydrogenation function of Pd/ γ -Al₂O₃ catalyst by Rh/ γ -Al₂O₃ addition in CO₂ methanation at low temperature, *ACS Catalysis* 3 (2013) 2799-2812.
 - [49] A. Slagtern, Y. Schuurman, C. Leclercq, X. Verykios, C. Mirodatos, Specific features concerning the mechanism of methane reforming by carbon dioxide over Ni/La₂O₃ catalyst, *Journal of Catalysis* 172 (1997) 118-126.
 - [50] S. Jiang, Y. Lu, S. Wang, Y. Zhao, X. Ma, Insight into the reaction mechanism of CO₂ activation for CH₄ reforming over NiO-MgO: A combination of DRIFTS and DFT study, *Applied Surface Science* 416 (2017) 59-68.
 - [51] M. Németh, Z. Schay, D. Srankó, J. Károlyi, G. Sáfrán, I. Sajó, A. Horváth, Impregnated Ni/ZrO₂ and Pt/ZrO₂ catalysts in dry reforming of methane: Activity tests in excess methane and mechanistic studies with labeled ¹³CO₂, *Applied Catalysis A: General* 504 (2015) 608-620.
 - [52] Y. Yan, Y. Dai, H. He, Y. Yu, Y. Yang, A novel W-doped Ni-Mg mixed oxide catalyst for CO₂ methanation, *Applied Catalysis B: Environmental* 196 (2016) 108-116.
 - [53] X. Jiao, L. Li, N. Zhao, F. Xiao, W. Wei, Synthesis and low-temperature CO₂ capture properties of a novel Mg-Zr solid sorbent, *Energy & Fuels* 27 (2013) 5407-5415.
 - [54] H. Lu, X. Yao, J. Li, S. Yao, Z. Wu, H. Zhang, H. Lin, T. Nozaki, Mechanism on the plasma-catalytic oxidation of graphitic carbon over Au/ γ -Al₂O₃ by in situ plasma DRIFTS-mass spectrometer, *Journal of Hazardous Materials* 396 (2020) 122730.
 - [55] X. Wang, U.S. Ozkan, Correlation of NO and CO₂ adsorption sites with aldehyde hydrogenation performance of sulfided NiMo/Al₂O₃ catalysts, *Journal of Catalysis* 227 (2004) 492-501.
 - [56] T. Nozaki, N. Muto, S. Kado, K. Okazaki, Dissociation of vibrationally excited methane on Ni catalyst: Part 1. Application to methane steam reforming, *Catalysis Today* 89 (2004) 57-65.
 - [57] J. Quan, F. Muttaqien, T. Kondo, T. Kozarashi, T. Mogi, T. Imabayashi, Y. Hamamoto, K. Inagaki, I. Hamada, Y. Morikawa, J. Nakamura, Vibration-driven reaction of CO₂ on Cu surfaces via Eley-Rideal-type mechanism, *Nature Chemistry* 11 (2019) 722-729.
 - [58] H. Ueta, L. Chen, R.D. Beck, I. Colon-Diaz, B. Jackson, Quantum state-resolved CH₄ dissociation on Pt(111): coverage dependent barrier heights from experiment and density functional theory, *Physical chemistry chemical physics : PCCP* 15 (2013) 20526-20535.
 - [59] A.L. Utz, Mode selective chemistry at surfaces, *Current Opinion in Solid State and Materials Science* 13 (2009) 4-12.
 - [60] Y. Qin, G. Niu, X. Wang, D. Luo, Y. Duan, Status of CO₂ conversion using microwave plasma, *Journal of CO₂ Utilization* 28 (2018) 283-291.
 - [61] A.S. Al-Fatesh, M.A. Naeem, A.H. Fakeeha, A.E. Abasaheed, Role of La₂O₃ as promoter

- and support in Ni/ γ -Al₂O₃ catalysts for dry reforming of methane, Chinese Journal of Chemical Engineering 22 (2014) 28-37.
- [62] H.J. Lee, W. Joe, I.K. Song, Direct synthesis of dimethyl carbonate from methanol and carbon dioxide over transition metal oxide/Ce_{0.6}Zr_{0.4}O₂ catalysts: Effect of acidity and basicity of the catalysts, Korean Journal of Chemical Engineering 29 (2012) 317-322.
- [63] J. Horlyck, S. Lewis, R. Amal, J. Scott, The impact of La doping on dry reforming Ni-based catalysts loaded on FSP-alumina, Topics in Catalysis 61 (2018) 1842-1855.
- [64] J. Guo, H. Lou, L. Mo, X. Zheng, The reactivity of surface active carbonaceous species with CO₂ and its role on hydrocarbon conversion reactions, Journal of Molecular Catalysis A: Chemical 316 (2010) 1-7.
- [65] J. Zheng, C. Wang, W. Chu, Y. Zhou, K. Köhler, CO₂ methanation over supported Ru/Al₂O₃ catalysts: Mechanistic studies by in situ infrared spectroscopy, ChemistrySelect 1 (2016) 3197-3203.
- [66] V. Ločař, FT-IR study of methanol, formaldehyde and methyl formate adsorption on the surface of Mo/Sn oxide catalyst, Applied Catalysis A: General 309 (2006) 33-36.
- [67] Q. Yang, X. Yin, C. Wu, S. Wu, D. Guo, Thermogravimetric-Fourier transform infrared spectrometric analysis of CO₂ gasification of reed (*Phragmites australis*) kraft black liquor, Bioresource Technology 107 (2012) 512-516.
- [68] C.-J. Liu, B. Xue, B. Eliasson, F. He, Y. Li, G.-H. Xu, Methane conversion to higher hydrocarbons in the presence of carbon dioxide using dielectric-barrier discharge plasmas, Plasma Chemistry and Plasma Processing 21 (2001) 301-310.
- [69] D. Andriamasinoro, R. Kieffer, A. Kiennemann, J.L. Rehspringer, P. Poix, A. Vallet, J.C. Lavalley, Preparations and characterization of lanthana catalysts: study of their activity in CO/H₂ reactions, Journal of Materials Science 24 (1989) 1757-1766.
- [70] S. Kameshima, K. Tamura, Y. Ishibashi, T. Nozaki, Pulsed dry methane reforming in plasma-enhanced catalytic reaction, Catalysis Today 256 (2015) 67-75.
- [71] T. Nozaki, S. Kameshima, Z. Sheng, K. Tamura, T. Yamazaki, in: X. Tu, J.C. Whitehead, T. Nozaki (Eds.), Plasma Catalysis: Fundamentals and Applications, Springer International Publishing, Cham, 2019, pp. 231-269.
- [72] Y. Wu, H. Xie, S. Tian, N. Tsubaki, Y. Han, Y. Tan, Isobutanol synthesis from syngas over K-Cu/ZrO₂-La₂O₃(x) catalysts: Effect of La-loading, Journal of Molecular Catalysis A: Chemical 396 (2015) 254-260.
- [73] J.K. Nørskov, Effective medium potentials for molecule-surface interactions: H₂ on Cu and Ni surfaces, The Journal of Chemical Physics 90 (1989) 7461-7471.
- [74] C. Zhi, Q. Wang, B. Wang, D. Li, R. Zhang, Insight into the mechanism of methane synthesis from syngas on a Ni(111) surface: a theoretical study, RSC Advances 5 (2015) 66742-66756.

Chapter 4: Electrical properties of dielectric barrier discharge

This chapter is adapted from the publication work:

Zunrong Sheng, Kenta Sakata, Yoshiki Watanabe, Seigo Kameshima, Hyun-Ha Kim, Shuiliang Yao, Tomohiro Nozaki, Journal of Physics D: Applied Physics 52 (2019) 414002 (13pp), DOI: 10.1088/1361-6463/ab2d36.

4.1 Abstract

This chapter presents the clear evidence of nonthermal plasma-induced synergism of biogas reforming studied at 5 kPa. Reactant conversion and product yield were increased by superposing dielectric barrier discharge (DBD) to the Ni-based supported catalyst at fixed temperature: reforming performance was further promoted by increasing the operating frequency from 12 kHz to 100 kHz, while maintaining the catalyst temperature (600 °C) as well as specific energy input ($SEI = 1.37$ eV/molecule). Reforming characteristics were correlated with the electrical properties of packed-bed DBD, showing the increase in discharge current is critically important to strength plasma-induced synergism, while an increase in mean electron energy seems to be a minor effect. Moreover, discharge properties were correlated with electron collision kinetics: the vibrationally excited CH₄ and CO₂ play a key role in plasma catalysis of biogas reforming.

4.2 Introduction

The methane dry reforming (MDR) is an endothermic reaction. To satisfy the reaction enthalpy, high-temperature thermal energy is required to meet the large positive value of Gibbs free energy in thermal reforming for spontaneous reaction [1]. Significantly, the plasma-assisted MDR could be initiated at much lower temperature than thermal catalysis due to the reactive species produced by electron impact reaction. Because electron-driven reaction is almost independent of ambient temperature, nonthermal plasma catalysis enables low-temperature MDR without any assist with combustion, bringing the tremendous benefits towards sustainable material and energy conversion processes.

The catalyst packed-bed dielectric barrier discharge (PB-DBD) reactor is most frequently employed plasma-assisted MDR [2-9], which features merits of low-cost, compact structure and flexible operation. It is also widely employed in other gas treatment fields, e.g. CH₄ stream reforming [10], VOCs abatement [11, 12], CO₂ decomposition [13], NO_x and ozone synthesis [14, 15], and formaldehyde removal [16]. The interaction of nonthermal plasma and heterogeneous catalyst is discussed in review literatures [17-20]; however, the effect of catalyst on plasma is complicated.

In a non-packed DBD reactor, discharge mode is the filamentary discharge propagating across the gas gap as the “free-standing” filamentary [1]. In a PB-DBD reactor, the surface streamer is propagated along catalyst surface [21-27], which is reported to be a key role to enhance the catalytic performance of catalyst [22]. Moreover, the electric field concentrates at several pellet contacts, instead of the uniform electric field, leading to intensive partial discharges between the contact area of catalysts [28-30]. Some works also reported that the porosity of catalyst enhanced the local electric field [31-34], contributing to a high energy tail of electron energy distribution [35-37]. According to the widely-used porous catalyst, the plasma generation, plasma penetration and electric field change have been discussed based on

different pore size both by simulation and experimental study [38, 39]. For example, Zhang *et al* reported that plasma species is generation is the pores of catalyst, which is in micrometer range [38].

This chapter presents the clear evidence of nonthermal plasma-induced synergism in relation to the discharge characteristics of PB-DBD operated at 5 kPa. Reactant conversion and product yield were increased by superposing the dielectric barrier discharge to the heterogeneous catalysts at fixed catalyst temperature: conversion and yield were further increased by increasing the operation frequency from 12 kHz to 100 kHz. The electrical properties of PB-DBD were studied comprehensively by the Lissajous plot analysis, showing the increase in discharge current is critically important to strengthen nonthermal plasma-induced synergism, while increase in mean electron energy seems to be a minor effect. Moreover, discharge properties were correlated with electron collision kinetics: the vibrationally excited CH₄ and CO₂ play a key role in plasma catalysis of MDR.

4.3 Experimental section

4.3.1 Experimental system

Figure 4.1 shows the reactor system. The reactor consists of a quartz tube (i.d. = 20 mm), the high voltage electrode (3 mm diameter) at the center and the ground electrode outside of the quartz tube. The high voltage was applied between these electrodes to generate PB-DBD. An external capacitor (33 nF) is connected to the ground electrode in series for charge measurement. The voltage and current waveforms were recorded by oscilloscope (Agilent Technologies; DSO-X 3014A) via the high voltage probe (Tektronix; P6015A) and the current probe (Tektronix; TCP201), respectively. The voltage and current waveforms are displayed in Figure 4.2. 100 kHz power source (ASTECH; LG-10S RF Generator) generates sinusoidal high voltage; 12 kHz power source (Logy Electric; LHV-13AC) generates deformed-sinusoidal

signal.

The commercially available catalyst pellets (ca. 11 g) were packed for 40 mm length as Figure 4.1 shown. The catalyst pellet is Rasching ring type with the dimension of 3×3 mm (diameter×height) having 1 mm hole. The components of catalyst are nickel (11% wt.) and lanthanum (3% wt.) with porous Al₂O₃ as support. Total pore volume of Ni was measured by H₂ adsorption, showing 0.65 cm³/g. The operational temperature is controlled by an electrical furnace. The temperature distribution of packed-bed is detected by a thermography through the observation window (Figure 4.1). Because catalyst bed temperature increased slightly due to the heat generated by DBD, the furnace temperature was adjusted so that the catalyst bed temperature was maintained at 600 °C. Plasma gas temperature was estimated by optical emission spectroscopy of rotational band of CO (B-A) transition [40], showing the gas temperature of streamers equilibrated with catalyst pellet temperature. The CH₄/CO₂ ratio was automatically incremented by the programed mass flow controller, while total flow rate was kept constant at 1000 cm³/min.

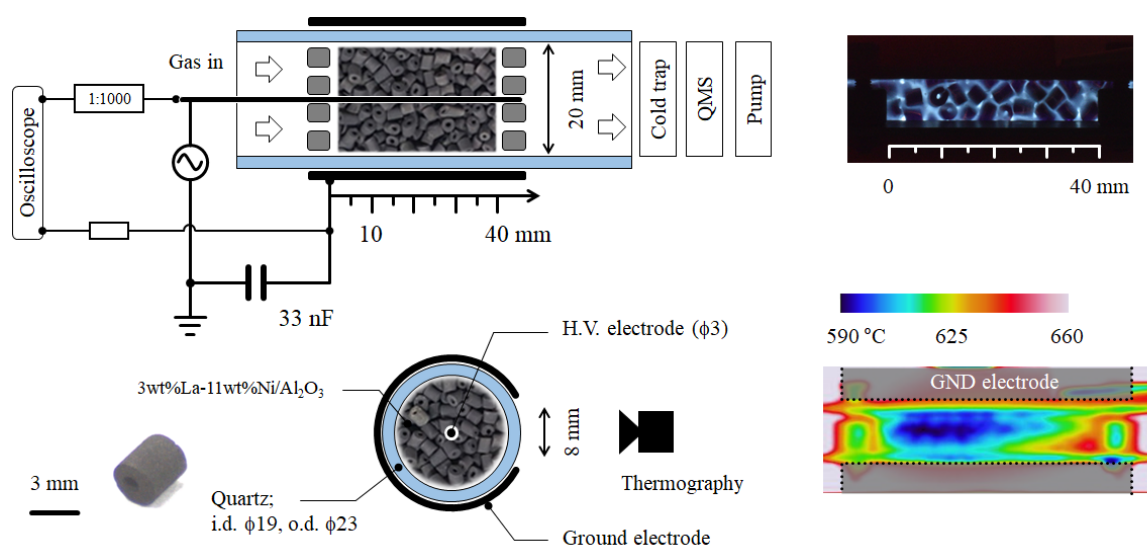


Figure 4.1 Schematic diagram of PB-DBD reactor. Inset pictures show DBD generated by 12 kHz high-voltage power source (Logy Electric) and a thermo-image of the packed-bed.

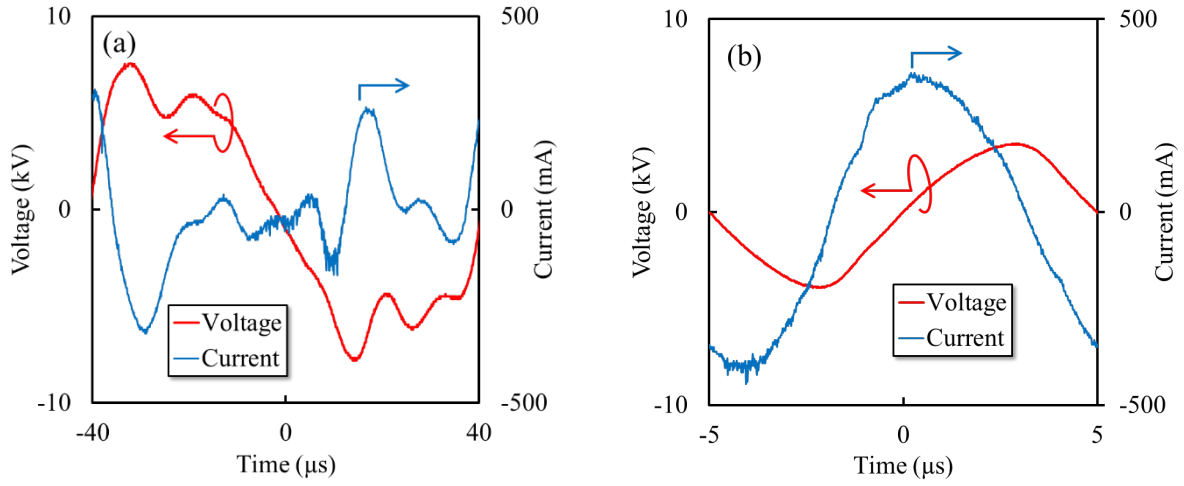


Figure 4.2 Voltage and current waveforms of packed-bed DBD: (a) 12 kHz and (b) 100 kHz. CH_4 fraction was 0.5, and power was 85 W.

4.3.2 Parameter definition

Specific energy input (*SEI*) has been defined in Chapter 2. The Gaseous hourly space velocity (*GHSV*) was calculated by the Eq 4.1:

$$GHSV \text{ (h}^{-1}\text{)} = \frac{60 \times Q_{\text{total}}^{\text{in}}}{V_0} \quad \text{Eq 4.1}$$

The $Q_{\text{total}}^{\text{in}}$ represents total volumetric gas flow rate at the reactor inlet (cm^3/min); V_0 expresses the volume of empty DBD reactor (cm^3); Based on the mole balance on the packed-bed DBD reactor, conversion and selectivity of each species were calculated by the Eq 4.2-4.6.

$$\text{CH}_4 \text{ conversion \%} = \frac{F_{\text{CH}_4}^{\text{in}} - F_{\text{CH}_4}^{\text{out}}}{F_{\text{CH}_4}^{\text{in}}} \times 100 \quad \text{Eq 4.2}$$

$$\text{CO}_2 \text{ conversion \%} = \frac{F_{\text{CO}_2}^{\text{in}} - F_{\text{CO}_2}^{\text{out}}}{F_{\text{CO}_2}^{\text{in}}} \times 100 \quad \text{Eq 4.3}$$

$$\text{H}_2 \text{ selectivity \%} = \frac{F_{\text{H}_2}^{\text{out}}}{2(F_{\text{CH}_4}^{\text{in}} - F_{\text{CH}_4}^{\text{out}})} \times 100 \quad \text{Eq 4.4}$$

$$\text{CO selectivity \%} = \frac{F_{\text{CO}}^{\text{out}}}{(F_{\text{CO}_2}^{\text{in}} - F_{\text{CO}_2}^{\text{out}}) + (F_{\text{CH}_4}^{\text{in}} - F_{\text{CH}_4}^{\text{out}})} \times 100 \quad \text{Eq 4.5}$$

$$\text{Coke selectivity \%} = \frac{F_{\text{coke}}}{(F_{\text{CO}_2}^{\text{in}} - F_{\text{CO}_2}^{\text{out}}) + (F_{\text{CH}_4}^{\text{in}} - F_{\text{CH}_4}^{\text{out}})} \times 100 \quad \text{Eq 4.6}$$

Average coking rate was calculated by the Eq 4.7 and Eq 4.8:

$$F_{\text{coke}} = \frac{1}{T_R} \times \frac{P}{RT} \times A \quad \text{Eq 4.7}$$

$$A = \int_0^{T_D} \Delta Q_{\text{CO}} dt \quad \text{Eq 4.8}$$

F (mol/s) expresses mole flow rate; ΔQ_{CO} (m³/s) represents volumetric flow rate of CO; T_D (s) and T_R (s) expresses the duration of decoking and reforming period, respectively. Refer to Figure 4.3 for the notation.

4.3.3 Experimental condition

The experimental conditions for reforming and Lissajous plot analysis are shown respectively in Table 4.1 (a) and (b).

Table 4.1 Conditions for experiments. (a) Reforming analysis at fixed power and temperature; (b) Lissajous plot analysis at fixed CH₄ fraction: Total flow rate = 1000 cm³/min (at STP); $GHSV = 5144 \text{ h}^{-1}$; Pressure = 5 kPa.

(a)	Frequency (kHz)	Power (W)	SEI (eV/molecule)	CH ₄ fraction (–)	Catalyst Temp. (°C)
Plasma catalysis	12 100	90	1.37	0.33–0.60	600
Thermal catalysis	-	-	-		
	100				

(b)	Frequency (kHz)	Power (W)	SEI (eV/molecule)	CH ₄ fraction (–)	Catalyst Temp. (°C)
PB-DBD	12				600
	100				
Empty-DBD	12	6–90	0.09–1.37	0.44	Furnace temp. was set to 600 °C
	100				

4.4 General reforming behavior

4.4.1 Pulsed reforming spectrometry

The representative result of pulsed reforming spectrometry is displayed in Figure 4.3: (a) and (b) show the gas composition and the corresponding catalyst temperature for the first 3 cycles, while (c) and (d) show the last 3 cycles. The real-time gases shown in Figure 4.3 were analyzed by the quadruple mass spectrometer (QMS, Prisma-100; Pfeiffer Vacuum GmbH). T_D (s) and T_R (s) in Figure 4.3 (c) expresses the duration of decoking and reforming period, respectively. Due to coke formation during the last 3 cycle, de-coking period was extended from 10 to 20 min. The conversion, selectivity, and average reaction rate were calculated when the gas composition and catalyst temperature reached the steady state at the end of each cycle.

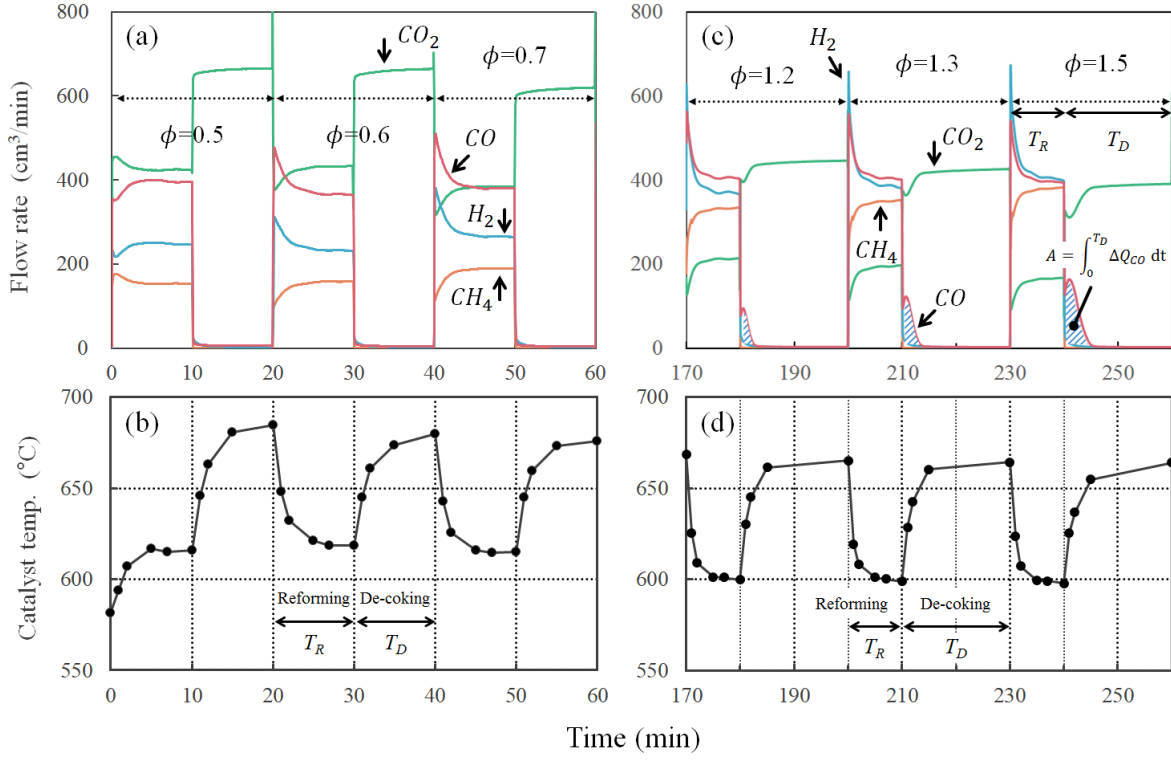
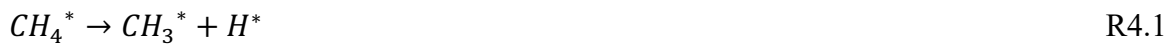


Figure 4.3 Time dependent change in gas composition and catalyst temperature. $\Phi = \text{CH}_4/\text{CO}_2$ ratio ($= 0.5, 0.6, 0.7, 0.8, 0.9, 1.0, 1.1, 1.2, 1.3, 1.5$). $f = 12$ kHz. Other conditions: see Table 4.1 (a).

4.4.2 Conversion and selectivity

Figure 4.4 (a)–(d) show basic reforming behavior: conversion and selectivity are plotted with respect to the initial CH_4 fraction. In overall, CH_4 and CO_2 conversion were enhanced clearly by DBD; reforming performance was further enhanced by increasing frequency from 12 kHz to 100 kHz at fixed catalyst temperature of 600 °C. CH_4 conversion is initiated by dissociative chemisorption (R4.1), followed by consecutive dehydrogenation of adsorbed CH_4 fragments (R4.2):



Reaction R4.1 is known to be the key rate-determining step for CH_4 reforming reaction, indicating DBD has an ability to promote the CH_4 dissociation reaction. Adsorbed CH_4 fragments (CH_x^*) must be oxidized to CH_xO^* by the adsorbed CO_2^* to yield syngas, while dehydrogenation of CH_x^* would occur spontaneously: full dehydrogenation of CH_x^* leads to the formation of undesired solid carbon. Although CO_2 conversion is enhanced by DBD (Figure 4.4 (b)), dehydrogenation of CH_x to coke is unavoidable when CH_4 fraction exceeds stoichiometry ($\text{CH}_4/\text{CO}_2 > 1$). At 100 kHz, coke formation is accelerated dramatically under CH_4 rich condition: correspondingly, CO selectivity decreased (Figure 4.4 (d)). Except for coking behavior, overall conversion and selectivity express a rather trivial trend: conversion increases by DBD at a fixed temperature and input power, while selectivity is incremented slightly. In the next section, detailed reforming behavior is discussed by the kinetic analysis.

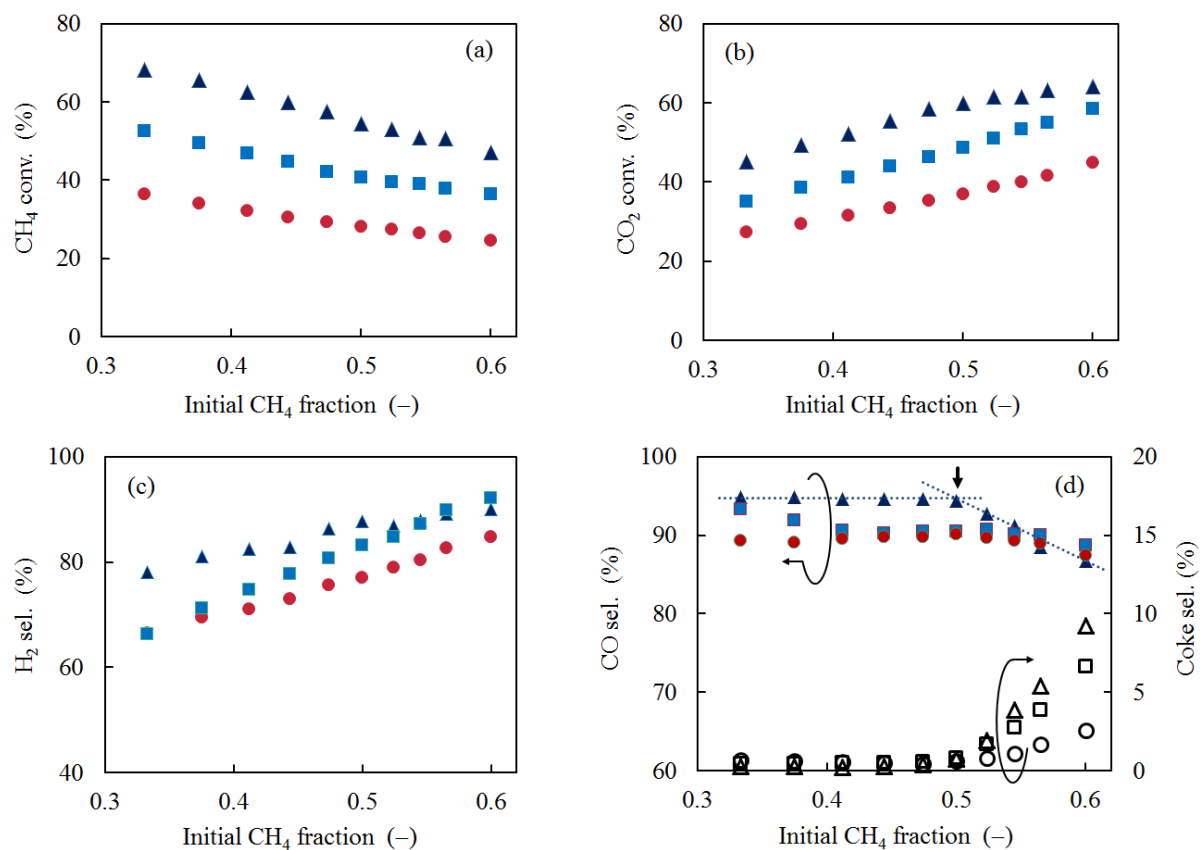


Figure 4.4 Conversion and selectivity at fixed catalyst temperature (600°C). Input power was also kept unchanged: see Table 4.1 (a) for experimental conditions. (a) CH₄ conversion; (b) CO₂ conversion; (c) H₂ selectivity; (d) CO and coke selectivity. ● Thermal catalysis; ■ Plasma catalysis (12 kHz); ▲ Plasma catalysis (100 kHz).

4.5 Discharge characteristics

Discharge properties of PB-DBD is further studied towards the deep insight into the reaction enhancement mechanism. The supplementary experiments in section 4.5.3 were carried out at fixed CH₄/CO₂ ratio and the catalyst temperature. Empty-DBD reactor (w/o catalyst pellets) was also employed, enabling comprehensive understanding of discharge behavior of PB-DBD.

4.5.1 Discharge power and controlling parameters

The discharge power was obtained by two methods: (a) Eq 4.9 by the integration of Lissajous plot (Figure 4.5) multiplies frequency to get P_L ; (b) Eq 4.10 by Manley's equation [41] to get P_M :

$$P_L = f \oint Q dU \quad \text{Eq 4.9}$$

$$P_M = 4f \bar{U}_{sus} C_{die} \left(\frac{U_{p-p}}{2} - \left(1 + \frac{C_{gas}}{C_{die}} \right) \bar{U}_{sus} \right) \quad \text{Eq 4.10}$$

f , Q and U are frequency, charge, and applied voltage respectively; \bar{U}_{sus} and U_{p-p} are the discharge sustain voltage and peak-to-peak applied voltage. The Lissajous plots of 12 kHz and 100 kHz DBD are shown in Figure 4.5. Because the Lissajous plot is slightly asymmetric, the \bar{U}_{sus} was measured by the mean absolute value of negative U_{sus}^- and positive U_{sus}^+ ; refer to Figure 4.5 for the notation of symbols. The C_{die} and C_{gas} are the capacitance of overall dielectric materials and gas gap, respectively. Assume C_{die} is much larger than C_{gas} together with Eq 4.11

and 4.12 [42], Eq 4.10 simplifies to Eq 4.13.

$$\frac{Q_{p-p}}{2} = C_{die} \left(\frac{U_{p-p}}{2} - \bar{U}_{sus} \right) \quad \text{Eq 4.11}$$

$$\frac{I_{p-p}}{2} = f \frac{Q_{p-p}}{2} \quad \text{Eq 4.12}$$

$$P_M = 4f \bar{U}_{sus} \frac{Q_{p-p}}{2} = 4 \bar{U}_{sus} \frac{I_{p-p}}{2} \quad \text{Eq 4.13}$$

Q_{p-p} represents the peak-to-peak value of charges accumulated over dielectric materials; I_{p-p} is equivalent to the macroscopic mean discharge current, which is not related directly to the nanosecond current pulses due to the streamer formation. Figure 4.6 shows there is a linear relationship between P_M and P_L . Catalyst temperature was adjusted at 600 °C in terms of input power variation. For the Empty-DBD, the temperature of the furnace was fixed at 600 °C. P_M overestimates P_L at 20 % maximum error probably because Eq. 5 does not take into account the stray capacity in the system. Nevertheless, Figure 4.6 draws an important conclusion that the Manley's equation is applicable to express the input power characteristics in packed-bed DBD in which the power-determining parameters are decoupled into \bar{U}_{sus} and I_{p-p} . Interestingly, all data points are plotted on a single line: there is no specific dependence on either packed materials or frequency. More interestingly, discharge properties are independent of gas composition where CH_4 and CO_2 conversion and product yield changed to a large extent by the presence of a catalyst as well as input power. This phenomenon is discussed in section 4.5.2 and 4.5.3.

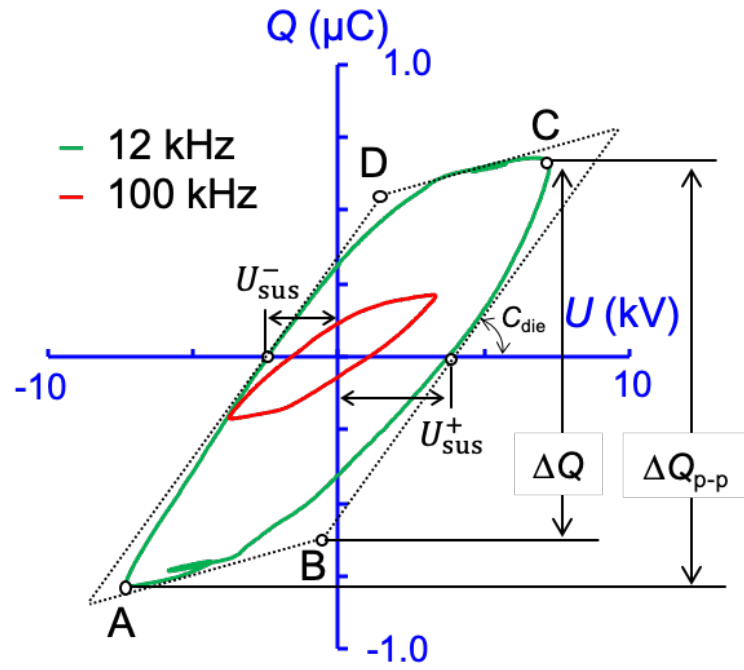


Figure 4.5 Lissajous plot (CH_4 fraction = 0.44, $P_L = 90$ W, catalyst temperature = 600 °C).

Green curve: 12 kHz DBD; Red curve: 100 kHz DBD.

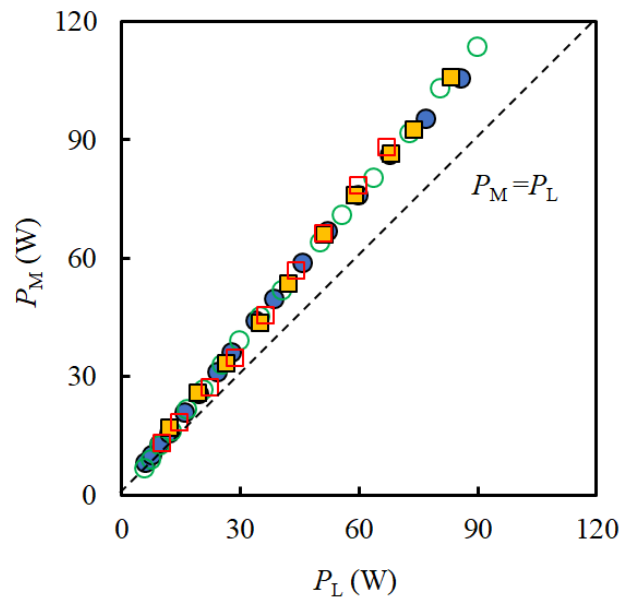


Figure 4.6 The relationship between P_M and P_L . \square 100 kHz Empty-DBD; \blacksquare 100 kHz PB-DBD; \circ 12 kHz Empty-DBD; \bullet 12 kHz PB-DBD. Conditions: Table 4.1 (b).

4.5.2 Voltage-Current characteristics

The power-determining parameters are analyzed at fixed discharge power of 90 W. Three parameters shown in Figure 4.7 are almost independent of initial CH₄ fraction, implying the discharge properties is essentially unaffected by CH₄ as well as CO₂ fraction. It is quite interesting but somewhat inconsistent with the common knowledge of discharge physics. Generally, discharge property depends greatly on gas composition; the composition changes from CH₄/CO₂ mixture at the reactor inlet to a mixture of CH₄/CO₂/CO/H₂/H₂O at the outlet. Moreover, as clearly seen in Figure 4.4, reforming behavior is quite different by CH₄ fraction, yielding wide variety of gas composition. Nevertheless, discharge properties, or power-determining parameters, are kept unchanged with respect to CH₄ fraction: microscopic insight into discharge behavior is probably not accessible by macroscopic approach such as Lissajous plot. There is inevitably a limitation for the interpretation of data. Keep this fact in mind, let us further analyze discharge behavior from macroscopic point of view.

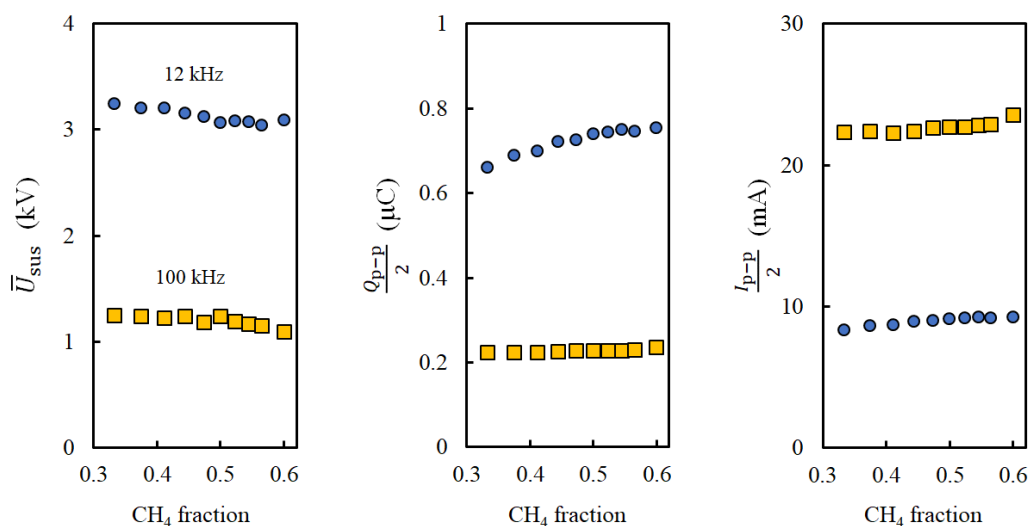


Figure 4.7 Power-determining parameters (Eq 4.13) v.s. Initial CH₄ fraction. ● 12 kHz PB-DBD; ■ 100 kHz PB-DB. Conditions: Table 4.1 (a).

In contrast, there is a unique dependence of the frequency on discharge current. The half value of peak-to-peak charge ($Q_{p-p}/2$) for 100 kHz-DBD is smaller than that of 12 kHz-DBD. At 100 kHz, charge accumulation period (B-C and D-A in Figure 4.5) is inevitably shorter than that of 12 kHz. Accordingly, total charges accumulated in the one-cycle basis at 100 kHz is smaller than that of 12 kHz. However, multiplying frequency to the total charge per cycle, discharge current for 100 kHz becomes larger. Ideally, all charges created by streamers are supposed to recombine and extinguish during the non-discharge period (A-B and C-D in Figure 4.5). However, the duration of non-discharge period at 100 kHz is shorter than that of 12 kHz, which may lead to residual charges over the packed materials. As a result, the discharge gap has a more electrically conductive nature at 100 kHz than 12 kHz, leading to lower sustain voltage (\bar{U}_{sus}) at fixed input power (cf. Eq. (4.19)). Such frequency-dependent voltage-current characteristics are quite well-known for DBD type discharge [43-45]: 12 kHz-DBD is characterized as high-voltage and low-current discharge, while 100 kHz-DBD is low-voltage and high-current discharge. The higher \bar{U}_{sus} would lead to a higher reduced electric field (E/N) that the electron would gain higher energy. It might imply that 12 kHz-DBD is more beneficial than 100 kHz-DBD in terms of excited species generation. However, conversion of CH_4 and CO_2 in 100 kHz-DBD is larger than that of 12 kHz-DBD (cf. Figure 4.4): increasing the discharge current is critically important than increasing the sustain voltage. Detailed discussion is presented in the section 4.6 in relation to the electron collision kinetics yielding vibrationally excited species.

4.5.3 Other properties

Figure 4.8 show (a) C_{die} , (b) \bar{U}_{sus} , (c) $Q_{p-p}/2$, and (d) $I_{p-p}/2$ with respect to the applied voltage. The C_{die} is measured by the slope of discharge phase (B→C and D→A) in Lissajous plot (Figure 4.5). The C_{die} increases linearly with increasing $U_{p-p}/2$ in all cases. The same trend

has been reported in Ref [46, 47]. Mei *et al* [48] simplified the overall capacitance of PB-DBD as two capacitances in series (Eq 4.14):

$$\frac{1}{C_{\text{die}}} = \frac{1}{C_{\text{quartz}}} + \frac{1}{C_{\text{pellet}}} \quad \text{Eq 4.14}$$

C_{die} is the overall capacitance for PB-DBD reactor; C_{quartz} and C_{pellet} respectively represents capacitance for quartz tube and packed materials. Interestingly, there is no significant difference in C_{die} between PB- and Empty-DBD reactors. Because C_{pellet} is much larger than C_{quartz} [48] and C_{die} is approximated by C_{quartz} . It is inevitable that C_{die} is independent of frequency within the range tested in this study.

The \bar{U}_{sus} and $Q_{\text{p-p}}/2$ increase linearly with applied voltage. The Empty-DBD reactor yields the similar trend with the corresponding PB-DBD reactor, illustrating that the packed materials play a minor role for changing discharge characteristics. This trend is different with some other studies [21, 49], where there is a change of Lissajous plot between PB- and Empty-DBD reactors in atmospheric pressure. This phenomenon could attribute to the reduced pressure operation in our study (5 kPa). Streamers are diffused and separated from pellet surface: properties of streamer are somewhat decoupled from dielectric properties of catalyst pellets. In fact, DBD is generated stably at 5 kPa under the coking condition where electrically conductive carbon film prohibits DBD formation at atmospheric pressure. In contrast, discharge current shows distinctive dependence on the frequency. At a fixed voltage, 100 kHz-DBD generates much larger discharge current than 12 kHz-DBD. Meantime, there is no noticeable difference between PB- and Empty-DBD reactors because of the same reason that $Q_{\text{p-p}}$ is not influenced by packed materials.

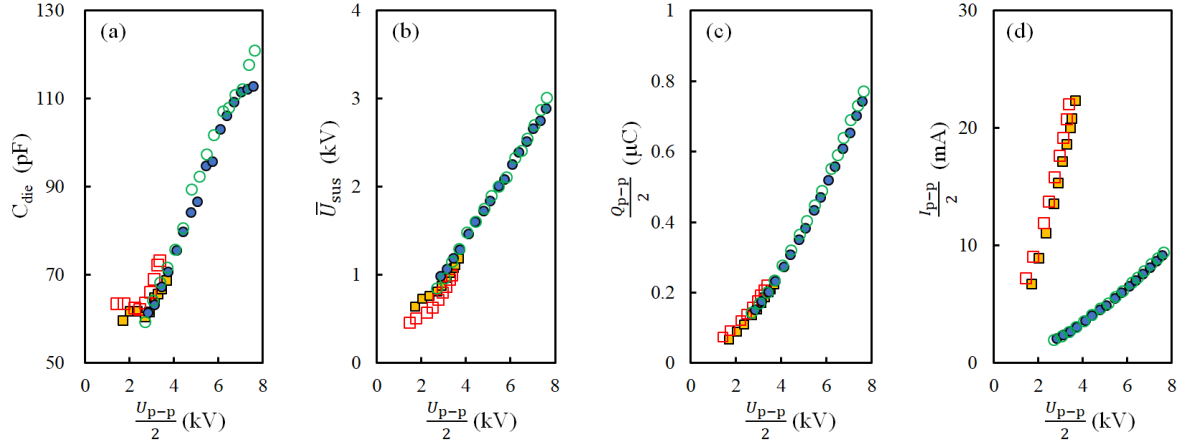


Figure 4.8 Power-determining parameters (Eq 4.13) v.s. Applied voltage at fixed CH_4/CO_2 ratio. \circ 12 kHz Empty-DBD; \bullet 12 kHz PB-DBD; \square 100 kHz Empty-DBD; \blacksquare 100 kHz PB-DBD. Conditions: Table 4.1 (b).

As shown in Figure 4.8 (a)-(c), discharge properties of 12 kHz and 100 kHz-DBD are plotted on the single curve. In this sense, we hypothesize that discharge properties and the related chemistry between 12 kHz and 100 kHz are essentially the same. Different discharge properties may arise that 100 kHz-DBD is operated at low \bar{U}_{sus} regime, while 12 kHz-DBD is operated at higher \bar{U}_{sus} regime within a single-curved characteristic. However, such difference was not identified by the macroscopic analysis of Lissajous plot. By contrast, effect of frequency is clearly distinguished. High-frequency operation induces increased number of streamers per unit time, leading to a remarkable increase in the overall discharge current. Inevitably, the total amount of excited species increases as discharge current increases that is the important source of plasma-induced synergism.

4.6 Electron collision kinetics

The net increase in CH₄ conversion by DBD is measured by the difference between plasma and thermal catalysis which were estimated from Figure 4.4 (a): the average value are shown in Table 4.2 (see ΔCH_4 column). The discharge current is also provided in Table 4.2, showing that $I_{p-p}/2$ is increased by 2.5 times by the frequency: correspondingly, the net increase in CH₄ conversion gained 2.0-fold (cf. *gain* row in Table 4.2). These numbers are further correlated with production rate of vibrationally excited species.

Table 4.2 Comparison of net increase in CH₄ conversion and production rate of vibrationally excited CH₄ in terms of mean discharge current.

	$\frac{I_{p-p}}{2}$ (mA)	$\frac{2\Delta Q}{2e}f$ (electron/s)	$F_{CH_4^v}$ (molecule/s)	ΔCH_4 (molecule/s)
Reference	Figure 4.7	Figure 4.5	Eq. 4.17	Figure 4.4
12 kHz	8.95	9.9×10^{16}	4.0×10^{18}	2.6×10^{19}
100 kHz	22.6	2.5×10^{17}	1.0×10^{19}	5.3×10^{19}
gain	2.5	2.5	2.5	2.0

First, rate coefficients were estimated by solving Boltzmann equation using BOLSIG+ with an appropriate cross-section set of CH₄ [50, 51] and CO₂ [51]. Table 4.3 presents a list of elementary reaction for elementally electron-molecule collisions considered in BOLSIG+. Knowing the rate coefficient, or inelastic collision frequency, is more important than energy loss fraction because we need to know how many active species are produced per unit time, and to validate such number is sufficient or not to explain plasma-induced synergism. Figure 4.9 shows the rate coefficients v.s. the reduced electric field (E/N). The result clearly shows the

production of vibrationally excited CH₄ and CO₂ is the dominant reaction pathways than dissociation and ionization when E/N is well below 700 Td. The rate expression for the production of vibrationally excited CH₄ is formulated as R4.3 and Eq 4.15.



$$r_v = \frac{dCH_4^v}{dt} = k_v N_{CH_4} N_e \quad Eq\ 4.15$$

Assume the rate constant is of the order of $k_v = 2 \times 10^{-14}$ m³/molecules/s; number density of CH₄ is $N_{CH_4} = 2 \times 10^{23}$ molecules/m³ (5 kPa, 873 K, CH₄/CO₂ = 1), electron density of streamer is $N_e = 10^{18}$ electrons/m³; streamer propagation time is $\Delta t = 10 \times 10^{-9}$ s. Put all these numbers into Eq 4.16, yielding the number density of vibrationally excited CH₄ produced in a single streamer:

$$\Delta CH_4^v = 2 \times 10^{-14} \times 2 \times 10^{23} \times 10^{18} \times 10 \times 10^{-9} = 4 \times 10^{19} \quad (\text{molecules}/m^3)$$

$$\Delta CH_4^v / N_e = 40 \quad Eq\ 4.16$$

Eq 4.16 implicates a single electron can produce 40 times more vibrationally excited CH₄ during streamer propagation. Although the model is oversimplified, numerical modeling of one-dimensional streamer propagation in CH₄ predicted a similar behavior [45]. Likewise, production of vibrationally excited CO₂ would contribute to the net increase in material conversion efficiency. Coupling Eq 4.16 and the charge transferred per half cycle (ΔQ ; see Figure 4.5), the production rate of vibrationally excited CH₄ per unit time is estimated as Eq 4.17.

$$F_{CH_4^v} = \left(2 \times \frac{\Delta Q}{2e} f \right) \times \left(\frac{\Delta CH_4^v}{N_e} \right) \quad \text{molecules/s} \quad Eq\ 4.17$$

Elementary charge is expressed as $e = 1.602 \times 10^{-19}$ (C). Assume electrons and ions are equally accumulated over the dielectric materials, ΔQ must be divided by 2; while discharge event

occurs every half cycle, 2 was multiplied.

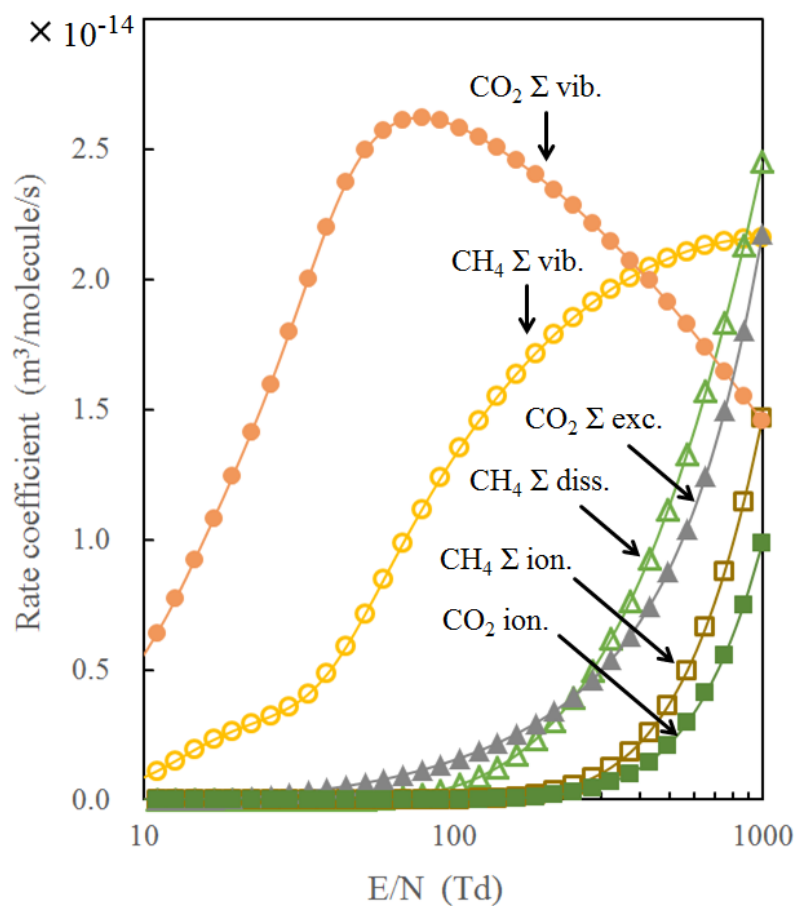


Figure 4.9 Electron collision rate coefficients estimated by BOLSIG+ (version 03/2016) at $\text{CH}_4/\text{CO}_2 = 1$ and 873 K. Momentum transfer and electron attachment are not shown. See Table 4.3 for elementary reactions.

Table 4.3 Elementary collision processes for CH₄ [50, 51] and CO₂ [51].

Description	Collision type	Reaction	Threshold (eV)
Not shown in Fig. 4.9	Attachment	$\text{CH}_4 \rightarrow \text{CH}_3 + \text{H}^-$	7.7
		$\text{CH}_4 \rightarrow \text{H}_2 + \text{CH}_2^-$	9.0
	Elastic	–	–
CH ₄ Σ vib.	Vibration	$\text{CH}_4 \rightarrow \text{CH}_4$ (V24)	0.16
		$\text{CH}_4 \rightarrow \text{CH}_4$ (V13)	0.36
CH ₄ Σ diss.	Dissociation	$\text{CH}_4 \rightarrow \text{CH}_4^* \rightarrow \text{CH}_3 + \text{H}$	9.0
		$\text{CH}_4 \rightarrow \text{CH}_4^* \rightarrow \text{CH}_2 + \text{H}_2$	10.0
		$\text{CH}_4 \rightarrow \text{CH}_4^* \rightarrow \text{CH} + \text{H}_2 + \text{H}$	11.0
		$\text{CH}_4 \rightarrow \text{CH}_4^* \rightarrow \text{C} + 2\text{H}_2$	12.0
CH ₄ Σ ion.	Ionization	$\text{CH}_4 \rightarrow \text{CH}_4^+$	12.6
		$\text{CH}_4 \rightarrow \text{H} + \text{CH}_3^+$	14.3
Not shown in Fig. 4.9	Attachment	$\text{CO}_2 \rightarrow \text{CO} + \text{O}^-$	3.85
	Elastic	–	–
CO ₂ Σ vib.	Vibration	$000 \rightarrow 010$	0.083
		$000 \rightarrow 020 + 100$	0.167
		$000 \rightarrow 0n0 + n00$	0.252
		$000 \rightarrow 001$	0.291
		$000 \rightarrow 0n0 + n00$	0.339
		$000 \rightarrow 0n0 + n00$	0.422
		$000 \rightarrow 0n0 + n00$	0.505
CO ₂ Σ exc.	Vib. excitation	$000 \rightarrow 0n0 + n00$	2.5
	Elect. excitation	$\text{CO}_2 \rightarrow \text{CO}_2^*$	7.0
			10.5
CO ₂ ion.	Ionization	$\text{CO}_2 \rightarrow \text{CO}_2^+$	13.3

Results are summarized in Table 4.2 for 12 kHz and 100 kHz cases. Production rate of CH_4^v is 5-6 times smaller than the net increase in CH_4 conversion. However, this number is surprisingly correlated well with the experimental observation. DBD is characterized as a number of weakly ionized streamers where ionization is limited in a sparsely distributed narrow filamentary region with nanosecond duration. However, due to a large inelastic collision frequency for vibrational excitation, as well as a large number of streamers generated per unit time, DBD has a capability of supplying a sufficient amount of vibrationally excited species: it is the key determining factor of DBD-induced synergism. For more accurate estimation, individual contribution of all vibrational species must be analyzed together with V-T relaxation. Another possibility is the free radicals such as CH_i ($i = 0-3$); however, the production rate of radicals is 10 times smaller than that of vibrational species. Moreover, lifetime is much shorter than vibrational species: radical flux to the catalyst surface may be too small to convince the synergism. Meantime, production of radical consumes a large part of electrical energy due to a large excitation threshold, leading to a significant energy penalty. Increasing the discharge current at low \bar{U}_{sus} regime is critically important to produce vibrationally excited species selectively, and thus for the efficient CH_4 and CO_2 conversion.

4.7 Conclusion

The basic property of dry methane reforming (biogas reforming) was investigated based on high- and low-frequency PB-DBD reactor. Aiming for providing deep insight into plasma-assisted catalytic performance, the discharge characteristics were investigated comprehensively, and correlated with reforming characteristics as well as electron collision kinetics. Major conclusions are summarized as follows:

- (1) As for overall reforming performance, 100 kHz-DBD leads the highest reactant conversion and product yield, followed by 12 kHz-DBD, and both of hybrid reforming show a

significant enhancement than thermal reforming under the fixed catalyst temperature (600 °C).

- (2) Excessive CH₄ activation accelerates coke formation: coking reaction is onset by DBD at smaller CH₄/CO₂ ratio, followed by faster growth of coke in the CH₄ rich condition.
- (3) Discharge power in PB-DBD is characterized by Manley's equation. The power-determining parameters are decoupled into \bar{U}_{sus} and I_{p-p} , while I_{p-p} is tuned by U_{p-p} and f : the effect of frequency on I_{p-p} is tremendous. On the other hand, \bar{U}_{sus} is not actively tailored by the operating condition: \bar{U}_{sus} is determined as a consequence of complex discharge events.
- (4) There is no clear difference between Empty- and PB-DBD reactors in discharge characteristics: overall capacitance, discharge sustain voltage, and electric charges are plotted on the single curve with respect to applied voltage regardless of packing materials as well as gas composition. DBD is operated at 5 kPa in this study: characteristics of streamer would be somewhat decoupled with dielectric properties of packing materials, leading to a negligible effect on discharge properties.
- (5) Discharge properties of 12 kHz and 100 kHz-DBD are essentially unchanged: 100 kHz is operated in the smaller \bar{U}_{sus} regime, while 12 kHz is operated in the higher \bar{U}_{sus} regime within the single-curved discharge characteristic. Some difference may arise due to different \bar{U}_{sus} ; however, the effect of \bar{U}_{sus} on discharge properties was not distinguished clearly by macroscopic analysis of Lissajous plot: the role of \bar{U}_{sus} on CH₄ and CO₂ activation process has yet to be elucidated in this study.
- (6) Large increase in discharge current at 100 kHz-DBD is due to the increased number of streamers per unit time, while discharge properties of "streamer swarm" would be kept unchanged. In other words, electron density and electron energy in a single streamer are most unlikely tailored by the frequency. The increase in discharge current is critically

important to emerge plasma-induced synergism, while an increase in mean electron energy seems to be a minor effect.

- (7) Further increase in frequency enables to strengthen the synergism due to the increased discharge current. It is presumably true only when the excess heat generation by DBD at high frequency is avoided. Increase in charge accumulation over the packed material at a higher frequency may lead to a transition of discharge behavior, which may be characterized by the deformation of Lissajous plot from standard parallelogram.
- (8) Generation of vibrationally excited species are the dominant electron-molecule collision pathways. Production rate of vibrationally excited species are correlated well with the net increase in CH₄ conversion, electric charges, and discharge current.
- (9) Due to the catalyst pellets, gas composition between Empty- and PB-DBD is completely different. Nevertheless, power-determining parameters were not distinguished clearly in terms of gas composition. An advanced diagnostic technique enabling microscopic insight is necessary. One possibility is an actinometrical emission spectroscopy based on a consistent collision-radiative model. Probe accessing and laser-induced absorption spectrometry are hard to apply to the packed-bed configuration.

4.8 Reference

- [1] Z. Sheng, S. Kameshima, K. Sakata, T. Nozaki, Plasma-enabled dry methane reforming, in: N. Britun, T. Silva (Eds.), *Plasma Chemistry and Gas Conversion*, IntechOpen, London, pp. 37-57.
- [2] S. Kameshima, K. Tamura, Y. Ishibashi, T. Nozaki, Pulsed dry methane reforming in plasma-enhanced catalytic reaction, *Catalysis Today* 256 (2015) 67-75.
- [3] Z. Sheng, S. Kameshima, S. Yao, T. Nozaki, Oxidation behavior of Ni/Al₂O₃ catalyst in nonthermal plasma-enabled catalysis, *Journal of Physics D: Applied Physics* 51 (2018) 445205.
- [4] S. Kameshima, R. Mizukami, T. Yamazaki, L.A. Prananto, T. Nozaki, Interfacial reactions between DBD and porous catalyst in dry methane reforming, *Journal of Physics D: Applied Physics* 51 (2018) 114006.

- [5] D. Ray, P.M.K. Reddy, C. Subrahmanyam, Ni-Mn/ γ -Al₂O₃ assisted plasma dry reforming of methane, *Catalysis Today* 309 (2018) 212-218.
- [6] L. Brune, A. Ozkan, E. Genty, T. Visart de Bocarmé, F. Reniers, Dry reforming of methane via plasma-catalysis: influence of the catalyst nature supported on alumina in a packed-bed DBD configuration, *Journal of Physics D: Applied Physics* 51 (2018) 234002.
- [7] S. Kameshima, K. Tamura, R. Mizukami, T. Yamazaki, T. Nozaki, Parametric analysis of plasma-assisted pulsed dry methane reforming over Ni/Al₂O₃ catalyst, *Plasma Processes and Polymers* 14 (2017) 1600096.
- [8] X. Wang, Y. Gao, S. Zhang, H. Sun, J. Li, T. Shao, Nanosecond pulsed plasma assisted dry reforming of CH₄: The effect of plasma operating parameters, *Applied Energy* 243 (2019) 132-144.
- [9] N. Bouchoul, E. Fourré, J.-M. Tatibouët, C. Batiot-Dupeyrat, Plasma-catalytic dry reforming of CH₄ over calcium oxide: Catalyst structural and textural modifications, *Plasma Chemistry and Plasma Processing* 39 (2019) 713-727.
- [10] T. Nozaki, W. Fukui, K. Okazaki, Reaction enhancement mechanism of the nonthermal discharge and catalyst hybrid reaction for methane reforming, *Energy & Fuels* 22 (2008) 3600-3604.
- [11] S. Yao, S. Weng, Q. Jin, H. Lu, Z. Wu, X. Zhang, J. Han, H. Lu, X. Tang, B. Jiang, Mechanism of decane decomposition in a pulsed dielectric barrier discharge reactor, *IEEE Transactions on Plasma Science* 44 (2016) 2660-2666.
- [12] H. Huang, D. Ye, X. Guan, The simultaneous catalytic removal of VOCs and O₃ in a post-plasma, *Catalysis Today* 139 (2008) 43-48.
- [13] R. Snoeckx, A. Bogaerts, Plasma technology - a novel solution for CO₂ conversion?, *Chemical Society reviews* 46 (2017) 5805-5863.
- [14] B.S. Patil, N. Cherkasov, J. Lang, A.O. Ibhaden, V. Hessel, Q. Wang, Low temperature plasma-catalytic NO_x synthesis in a packed DBD reactor: Effect of support materials and supported active metal oxides, *Applied Catalysis B: Environmental* 194 (2016) 123-133.
- [15] U. Kogelschatz, Dielectric-barrier discharges: Their history, discharge physics, and industrial applications, *Plasma Chemistry and Plasma Processing* 23 (2003) 1-46.
- [16] X. Zhu, X. Gao, R. Qin, Y. Zeng, R. Qu, C. Zheng, X. Tu, Plasma-catalytic removal of formaldehyde over Cu–Ce catalysts in a dielectric barrier discharge reactor, *Applied Catalysis B: Environmental* 170-171 (2015) 293-300.
- [17] W.-C. Chung, D.-H. Mei, X. Tu, M.-B. Chang, Removal of VOCs from gas streams via plasma and catalysis, *Catalysis Reviews* (2018) 1-62.
- [18] E.C. Neyts, K. Ostrikov, M.K. Sunkara, A. Bogaerts, Plasma catalysis: Synergistic effects at the nanoscale, *Chemical Reviews* 115 (2015) 13408-13446.
- [19] E.C. Neyts, A. Bogaerts, Understanding plasma catalysis through modelling and

- simulation—a review, *Journal of Physics D: Applied Physics* 47 (2014) 224010.
- [20] H.-H. Kim, Y. Teramoto, N. Negishi, A. Ogata, A multidisciplinary approach to understand the interactions of nonthermal plasma and catalyst: A review, *Catalysis Today* 256 (2015) 13-22.
 - [21] X. Tu, H.J. Gallon, M.V. Twigg, P.A. Gorry, J.C. Whitehead, Dry reforming of methane over a Ni/Al₂O₃ catalyst in a coaxial dielectric barrier discharge reactor, *Journal of Physics D: Applied Physics* 44 (2011) 274007.
 - [22] H.-H. Kim, J.-H. Kim, A. Ogata, Microscopic observation of discharge plasma on the surface of zeolites supported metal nanoparticles, *Journal of Physics D: Applied Physics* 42 (2009) 135210.
 - [23] H. Kim, N. Hwang, A. Ogata, Y. Song, Propagation of surface streamers on the surface of HSY zeolites-supported silver nanoparticles, *IEEE Transactions on Plasma Science* 39 (2011) 2220-2221.
 - [24] H.-H. Kim, Y. Teramoto, T. Sano, N. Negishi, A. Ogata, Effects of Si/Al ratio on the interaction of nonthermal plasma and Ag/HY catalysts, *Applied Catalysis B: Environmental* 166-167 (2015) 9-17.
 - [25] X. Tu, H.J. Gallon, J.C. Whitehead, Transition behavior of packed-bed dielectric barrier discharge in argon, *IEEE Transactions on Plasma Science* 39 (2011) 2172-2173.
 - [26] T. Nozaki, N. Muto, S. Kadio, K. Okazaki, Dissociation of vibrationally excited methane on Ni catalyst: Part 2. Process diagnostics by emission spectroscopy, *Catalysis Today* 89 (2004) 67-74.
 - [27] A. Mizuno, Generation of non-thermal plasma combined with catalysts and their application in environmental technology, *Catalysis Today* 211 (2013) 2-8.
 - [28] T. Nozaki, K. Okazaki, Non-thermal plasma catalysis of methane: Principles, energy efficiency, and applications, *Catalysis Today* 211 (2013) 29-38.
 - [29] J. Van Durme, J. Dewulf, C. Leys, H. Van Langenhove, Combining non-thermal plasma with heterogeneous catalysis in waste gas treatment: A review, *Applied Catalysis B: Environmental* 78 (2008) 324-333.
 - [30] M.A. Malik, Y. Minamitani, K.H. Schoenbach, Comparison of catalytic activity of aluminum oxide and silica gel for decomposition of volatile organic compounds (VOCs) in a plasmacatalytic Reactor, *IEEE Transactions on Plasma Science* 33 (2005) 50-56.
 - [31] O. Guaitella, F. Thevenet, E. Puzenat, C. Guillard, A. Rousseau, C₂H₂ oxidation by plasma/TiO₂ combination: Influence of the porosity, and photocatalytic mechanisms under plasma exposure, *Applied Catalysis B: Environmental* 80 (2008) 296-305.
 - [32] K. Woo Seok, P. Jin Myung, K. Yongho, H. Sang Hee, Numerical study on influences of barrier arrangements on dielectric barrier discharge characteristics, *IEEE Transactions on Plasma Science* 31 (2003) 504-510.
 - [33] C. Jen-Shih, K.G. Kostov, K. Urashima, T. Yamamoto, Y. Okayasu, T. Kato, T. Iwaizumi,

- K. Yoshimura, Removal of NF_3 from semiconductor-process flue gases by tandem packed-bed plasma and adsorbent hybrid systems, *IEEE Transactions on Industry Applications* 36 (2000) 1251-1259.
- [34] T. Takuma, Field behaviour at a triple junction in composite dielectric arrangements, *IEEE Transactions on Electrical Insulation* 26 (1991) 500-509.
- [35] C.-j. Liu, J.-x. Wang, K.-l. Yu, B. Eliasson, Q. Xia, B. Xue, Y.-h. Zhang, Floating double probe characteristics of non-thermal plasmas in the presence of zeolite, *Journal of Electrostatics* 54 (2002) 149-158.
- [36] F. Holzer, F.D. Kopinke, U. Roland, Influence of ferroelectric materials and catalysts on the performance of non-thermal plasma (NTP) for the removal of air pollutants, *Plasma Chemistry and Plasma Processing* 25 (2005) 595-611.
- [37] X. Tu, H.J. Gallon, J.C. Whitehead, Electrical and spectroscopic diagnostics of a single-stage plasma-catalysis system: effect of packing with TiO_2 , *Journal of Physics D: Applied Physics* 44 (2011) 482003.
- [38] Y.-R. Zhang, K. Van Laer, E.C. Neyts, A. Bogaerts, Can plasma be formed in catalyst pores? A modeling investigation, *Applied Catalysis B: Environmental* 185 (2016) 56-67.
- [39] Q.-Z. Zhang, W.-Z. Wang, A. Bogaerts, Importance of surface charging during plasma streamer propagation in catalyst pores, *Plasma Sources Science and Technology* 27 (2018).
- [40] Y. Du, K. Tamura, S. Moore, Z. Peng, T. Nozaki, P.J. Bruggeman, $\text{CO}(\text{B}^1\Sigma^+ \rightarrow \text{A}^1\Pi)$ angstrom system for gas temperature measurements in CO_2 containing plasmas, *Plasma Chemistry and Plasma Processing* 37 (2017) 29-41.
- [41] T.C. Manley, The electric characteristics of the ozonator discharge, *Transactions of The Electrochemical Society* 84 (1943) 83.
- [42] Z. Falkenstein, J.J. Coogan, Microdischarge behaviour in the silent discharge of nitrogen - oxygen and water - air mixtures, *Journal of Physics D: Applied Physics* 30 (1997) 817-825.
- [43] J.S. Boisvert, J. Margot, F. Massines, Transitions of an atmospheric-pressure diffuse dielectric barrier discharge in helium for frequencies increasing from kHz to MHz, *Plasma Sources Science and Technology* 26 (2017) 035004.
- [44] T. Nozaki, K. Okazaki, Carbon nanotube synthesis in atmospheric pressure glow discharge: A review, *Plasma Processes and Polymers* 5 (2008) 300-321.
- [45] T. Nozaki, N. Muto, S. Kado, K. Okazaki, Dissociation of vibrationally excited methane on Ni catalyst: Part 1. Application to methane steam reforming, *Catalysis Today* 89 (2004) 57-65.
- [46] T. Butterworth, R. Elder, R. Allen, Effects of particle size on CO_2 reduction and discharge characteristics in a packed bed plasma reactor, *Chemical Engineering Journal* 293 (2016) 55-67.

- [47] T. Butterworth, R.W.K. Allen, Plasma-catalyst interaction studied in a single pellet DBD reactor: dielectric constant effect on plasma dynamics, *Plasma Sources Science and Technology* 26 (2017) 065008.
- [48] D. Mei, X. Zhu, Y.-L. He, J.D. Yan, X. Tu, Plasma-assisted conversion of CO₂ in a dielectric barrier discharge reactor: understanding the effect of packing materials, *Plasma Sources Science and Technology* 24 (2014) 015011.
- [49] Y. Uytendhouwen, S. Van Alphen, I. Michiels, V. Meynen, P. Cool, A. Bogaerts, A packed-bed DBD micro plasma reactor for CO₂ dissociation: Does size matter?, *Chemical Engineering Journal* 348 (2018) 557-568.
- [50] W.L. Morgan, A critical evaluation of low-energy electron impact cross sections for plasma processing modeling. II: Cl₄, SiH₄, and CH₄, *Plasma Chemistry and Plasma Processing* 12 (1992) 477-493.
- [51] MORGAN database. <http://www.lxcat.laplace.univ-tlse.fr> (retrieved 4 June 2013).

Chapter 5: Kinetic study on methane dry reforming

This chapter is adapted from the publication work:

Zunrong Sheng, Yoshiki Watanabe, Hyun-Ha Kim, Shuiliang Yao and Tomohiro Nozaki, Chemical Engineering Journal 399 (2020) 125751, DOI: 10.1016/j.cej.2020.125751.

5.1 Abstract

A rigorous determination of kinetic parameters of CH₄ dry reforming is provided to elucidate the drastic reaction promotion mechanism enabled by plasma-catalyst interaction. Lanthanum-modified Ni/Al₂O₃ catalyst was combined with dielectric barrier discharge (DBD) at 5 kPa and 400–700 °C without dilution gas. Reaction order for CH₄ and CO₂ were determined respectively as 0.68 and –0.17, which were kept unchanged by DBD, indicating the surface coverage of CH₄ and CO₂ was not influenced by nonthermal plasma. The Arrhenius plot for forward CH₄ rate constant revealed that 12 kHz DBD hybrid reaction is characterized as *mixed catalysis* where plasma and thermal catalysis are not decoupled. In contrast, 100 kHz DBD is regarded as *pure plasma catalysis*, which yielded significant improvement of CH₄ and CO₂ conversion via vibrational excitation. Activation energy decreased from 91 kJ/mol to 44.7 kJ/mol which was well correlated with the state-specific gas-surface reactivity of vibrationally excited CH₄ on Ni surfaces.

5.2 Introduction

Nonthermal plasma-assisted catalytic conversion of CH₄ shows a multiple-functional benefit which enables fluctuating renewable power utilization and CH₄ upgrade to various chemical commodities [1-3]. Moreover, nonthermal plasma provides a promising reaction pathway to reduce the reaction temperature while promoting reforming performance with the

appropriate catalysts and reaction system are combined [4-7]. CH₄ is the most stable hydrocarbon molecules due to highly symmetric C-H geometry. High temperature thermal energy is required to activate the strong C-H bond which inevitably uses combustion of feedstock [7-9]. Advantage of nonthermal plasma is the use of electron impact reaction occurring independently of reaction temperature [10-12]. Particularly, activation into vibrationally excited states is known to be an effective approach when combining heterogeneous catalysts [13-15]. Such unique reactivity is not limited to CH₄, but similar reaction enhancement mechanism is possible with CO₂ [15-17], H₂O [18, 19], and N₂ [20, 21].

State-resolved molecular beam study revealed the vibrationally excited CH₄ enhances dissociative chemisorption over Ni clean surface [22, 23]. There is a mode selective reactivity, showing a drastic decrease of the C-H activation energy barrier is possible via stretching vibration mode where the vibrational efficacy exceeds 100 % [24]. Similarly, vibrationally excited CO₂ enhances the surface reaction between adsorbed hydrogen in the Eley-Rideal mechanism [16, 25]. Meanwhile, the molecular beam study does not mention a particular reaction system which enables supplying vibrationally excited molecules without increasing the temperature of the system. Vibrationally excited CH₄ and CO₂ are generated abundantly by the low-energy electron collision in nonthermal plasma. References [13, 26] confirmed that a single electron produces 40–150 times more vibrationally excited CH₄ and CO₂ in dielectric barrier discharge (DBD) type nonthermal plasma. The vibrationally excited molecules would most likely contribute to the net increase of CH₄ and CO₂ conversion in the DBD-catalyst hybrid reaction. However, unlike the molecular beam study, there are several difficulties to make deeper insight into mode-selective promotion of catalytic reaction. First, quantitative measurement of vibrationally excited molecules and their transport property, or flux to the catalyst surface, is hard to attain. Because nonthermal plasma is generated in a packed-bed reactor which hinders the optical probing for the *in situ* optical diagnostics of target molecules.

Second, catalyst surface is not clean and contaminated by various adsorbed molecules. Moreover, nanocrystal catalyst consists of different facets on their surface: not only catalyst metals, but also the support materials and catalyst-support-interface play a significant role. Third, not all molecules are excited into vibrational states because nonthermal plasma is characterized as weakly ionized plasma; therefore, plasma catalysis is considered as *mixed catalysis* where both thermal and plasma-induced catalysis are coupled.

Considering these facts, rigorous determination of intrinsic kinetic parameters of plasma-enabled promotion of CH₄ dry reforming was performed using lanthanum-modified Ni/Al₂O₃ catalyst. First, reaction order was determined in a consistent manner with and without DBD. Data was analyzed based on Langmuir-Hinshelwood surface reaction model for bimolecular system (CH₄ and CO₂). The reaction order, or the surface coverage of adsorbed species, was essentially unchanged by DBD: $\alpha = 0.68$ for CH₄ and $\beta = -0.17$ for CO₂. By knowing reaction orders and feed gas conversion, the reaction rate constant was decoupled from the overall forward reaction rate, providing the activation energy of the intrinsic plasma-surface reaction. Activation energy of the forward CH₄ reaction rate was analyzed as a functions of catalyst temperature, specific energy input (*SEI*, eV/molecule), and the frequency of power source. Activation energy decreases from 91 kJ/mol for the thermal catalysis to 44.7 kJ/mol for 100 kHz DBD hybrid reaction. These estimation was well correlated with the state-specific molecular beam study which yielded the activation energy of 42–69 kJ/mol via vibrationally excited CH₄ on Ni surface. In the case of 12 kHz DBD, plasma-catalyst hybrid reaction is characterized as *mixed catalysis*: plasma and thermal catalysis behavior were observed simultaneously. The apparent activation energy is essentially unchanged by *SEI* unless the electrical properties of DBD is kept unchanged. The intrinsic kinetic parameters of plasma-enabled promotion of CH₄ dry reforming are discussed comprehensively.

5.3 Experimental section

5.3.1 Experimental system

The detailed experimental system was presented in chapter 4 [26]. Briefly, packed-bed dielectric barrier discharge (PB-DBD) reactor was employed in this study. Quartz tube (i.d. 20 mm, o.d. 23 mm) was packed with Lanthanum-modified Ni/Al₂O₃ catalyst pellets over 40 mm length (Raschig ring; La-3wt%; Ni-11wt%). High-voltage (stainless steel) electrode is located in the center of the reactor (3 mm diameter). Two power sources were used for this experiment: (i) 12 kHz–100 W (Logy Electric; LHV-13AC), (ii) 15 kHz–200 W (Tamaoki Electronics; TE-HFV1520K-0400), and (iii) 100 kHz–100 W (ASTECH; LG-10S RF Generator). All power sources generate sinusoidal high-voltage output. Online gas analysis was performed by a quadrupole mass spectrometer (QMS, PrismaPlus; Pfeiffer Vacuum GmbH). Temperature of the catalyst bed was measured by the infrared camera (TH5104; NEC Sanei Instrument Ltd.). The measured data was calibrated by the thermocouples in advance, and further correlated with the rotational temperature of CO Angstrom system [27], showing the gas (rotational) temperature of corresponding emission region and the catalyst temperature are equilibrated.

5.3.2 Temperature measurement

Temperature distribution of catalyst bed is provided in Figure 5.1 based on thermal reforming, 12 kHz and 100 kHz DBD hybrid reforming, respectively. Catalyst temperature is determined by the energy balance: 1. Heating by the external electric heater, 2. Heat generated by DBD (if any), 3. Heat absorption by dry reforming, and 4. Heat removed by gas flow. It should be pointed out that the average catalyst temperature is in the same level for thermal and 12/100 kHz DBD hybrid reforming, while endothermic energy is different (cf. the CH₄/CO₂ conversion in Chapter 4): the endothermic enthalpy for 100 kHz DBD is greater than 12 kHz DBD because of larger CH₄ conversion. Meanwhile, input power was kept unchanged. One

might expect the catalyst bed temperature in 100 kHz DBD would be lower than that of 12 kHz DBD. However, such situation increases the temperature difference between catalyst bed and the furnace, increasing the heat flux from the furnace to the catalyst bed. As a result, catalyst temperature is in the same level even though the endothermic energy is different.

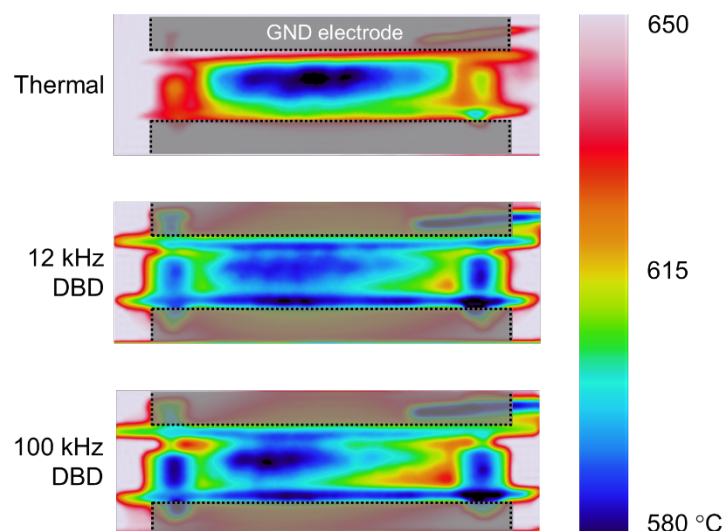


Figure 5.1 Thermal images of catalyst bed in thermal reforming, 12 kHz and 100 kHz DBD hybrid reforming. Average catalyst temperature = 600 °C; Input power in 12 kHz and 100 kHz DBD is 90 W.

5.4 Kinetic analysis

5.4.1 Reaction order for thermal reaction

The forward CH_4 reaction rate is expressed by the power-law kinetics (Eq 5.1-5.3). By taking the natural logarithm of Eq 5.1 and rewrite it into Eq 5.2. The k_f and P expresses the forward reaction rate constant and the average concentration of feed gas (mol/m^3). In order to avoid excessive coke accumulation in CH_4 rich condition, the pulsed reforming technique was applied [5]. Catalyst temperature was set to ca. 480 °C so that the reaction order is evaluated in the reaction-limited regime ($480\text{ °C} < T_B = 510\text{ °C}$; cf. Figure 5.3 and Table 5.4). Conversion

of CH₄ and CO₂ were below 20% which is sufficiently below the thermal equilibrium and the effect of reverse reaction was ignored.

$$-\frac{dP_{CH_4}}{dt} = r_{CH_4} = k_f P_{CH_4}^\alpha P_{CO_2}^\beta \quad \text{Eq 5.1}$$

$$\ln(r_{CH_4}) = \ln(k_f) + \alpha \ln(P_{CH_4}) + \beta \ln(P_{CO_2}) \quad \text{Eq 5.2}$$

$$P_i = \frac{P_i^{in} + P_i^{out}}{2} \quad \text{Eq 5.3}$$

The average reaction rate (r_i ; mol/m³/s) was calculated using mole concentration of each species (P_i ; mol/m³) in Eq 5.4–5.6.

$$r_i = v_i r = \frac{\Delta C_i}{\Delta t} = \frac{C_i^{in} - C_i^{out}}{\Delta t} \quad \text{Eq 5.4}$$

$$\Delta t = \frac{2V}{Q_{total}^{in} + Q_{total}^{out}} \quad \text{Eq 5.5}$$

$$V = V_0 - \sum v_{pellet} \quad \text{Eq 5.6}$$

v_{pellet} expresses the volume of a single catalyst pellet ($v_{pellet} = 18.8 \text{ mm}^3$; $\phi 3 \times \phi 1 \times 3$ mm). By measuring the total weight of all packed pellets multiple times, the average number of pellets is 302 pieces, yielding $V = 5965 \text{ mm}^3$ ($V_0 = 11663 \text{ mm}^3$).

Figure 5.2 shows $\ln(k_f)$ v.s. $\ln(P_{CH_4})$ and $\ln(P_{CO_2})$ respectively. Experimental conditions are presented in Table 5.1. The forward reaction rate increases monotonically with the average CH₄ concentration and the reaction order was obtained from the slope as $\alpha = 0.68$. In contrast, forward reaction rate decreases slightly with average CO₂ concentration, resulting in $\beta = -0.17$. As a result, the power-law rate equation is determined as Eq 5.7. For Ni-based catalysts, reaction orders for CH₄ dry reforming are in the range of $\alpha = 0.55$ – 1.1 and $\beta = 0$ – 0.55 [28]. When a catalyst promoter (such as rare earth, alkali, or alkaline-earth metal oxides) is added, reaction order for CO₂ changes from positive to negative value [29] because the formation of carbonate species with a promoter element modifies the adsorption behavior of CO₂.

$$r_{CH_4} = k_f P_{CH_4}^{0.68} P_{CO_2}^{-0.17} \quad \text{Eq 5.7}$$

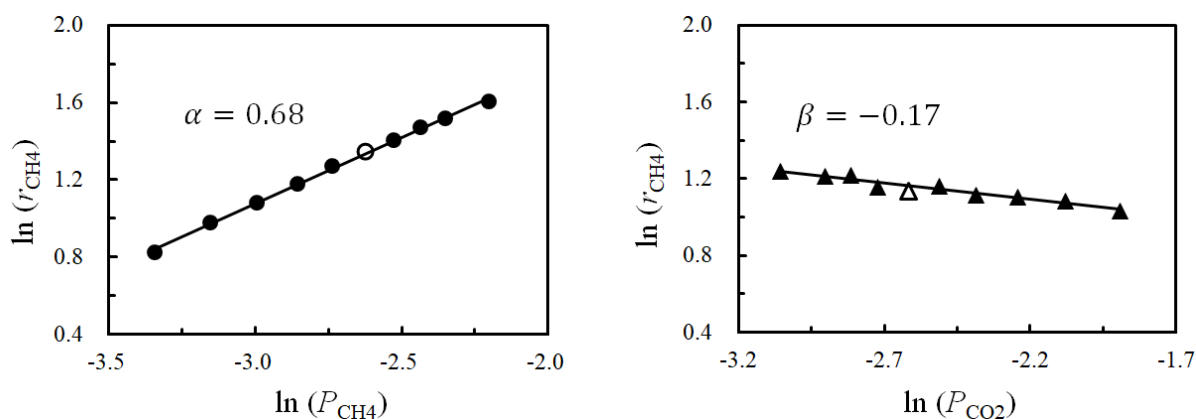


Figure 5.2 Reaction order in thermal reaction for CH_4 (α) and CO_2 (β), respectively. A hollow symbol represents stoichiometric condition ($CH_4/CO_2 = 1$).

Table 5.1 Experimental conditions for the reaction order α and β without DBD. Total flow rate = 2,000 cm^3/min (STP); $GHSV = 10,290 h^{-1}$ (STP); Catalyst temperature = 480 $^{\circ}C$; Pressure = 5 kPa. Argon was used as a balance.

α	CH_4	100	120	140	160	180	200	220	240	260	300
Flow rate	CO_2	200									
(cm^3/min)	Ar	1700	1680	1660	1640	1620	1600	1580	1560	1540	1500
CH_4/CO_2 ratio		0.5	0.6	0.7	0.8	0.9	1.0	1.1	1.2	1.3	1.5
β	CH_4	200									
Flow rate	CO_2	400	333	286	250	222	200	182	167	154	133
(cm^3/min)	Ar	1400	1467	1514	1550	1578	1600	1618	1633	1646	1667
CH_4/CO_2 ratio		0.5	0.6	0.7	0.8	0.9	1.0	1.1	1.2	1.3	1.5

5.4.2 Surface coverage

In the case of Ni/Al₂O₃ catalyst, CH₄ weakly chemisorbed on Ni surface and CO₂ strongly bounded near the metal-support interface [30, 31]. Based on the Langmuir-Hinshelwood reaction model with bimolecular reaction system (CH₄ and CO₂) where adsorption of the respective molecule occurs independent sites, the overall reaction rate is expressed by the Eq 5.8 [31-33]. k_s expresses the surface reaction rate constant; P is concentration of reactant; θ is a surface coverage ($0 < \theta < 1$); K is an equilibrium constant for adsorption/desorption; n is a number of active sites per unit area. Subscript A and B respectively denotes CH₄ and CO₂. K and θ are correlated with Langmuir isotherm where adsorption and desorption are equilibrated. Assume CH₄ is weakly bound by metallic sites and CO₂ adsorption is strong and equilibrated [3] that $K_A P_A \ll 1$ and $K_B P_B \gg 1$ [31, 32], the above equation is approximated as Eq 5.9 and Eq 5.10. Because k_s and K_A are temperature dependent, k_f is expressed by Arrhenius form as a temperature dependent term. For the simple formulation with the ideal assumption where no side reaction occurs, reaction order is deduced as $\alpha = 1$ and $\beta = 0$, respectively. Such relationship is well reproduced in Figure 5.1, showing the forward reaction rate increases linearly with CH₄ partial pressure: it is almost independent with respect to CO₂ concentration, meaning the zeroth-order dependence.

$$r_{CH_4} = k_s n_A n_B \theta_A \theta_B = k_s n_A n_B \frac{K_A K_B P_A P_B}{(1 + K_A P_A)(1 + K_B P_B)} \quad \text{Eq 5.8}$$

$$r_{CH_4} = k_s n_A n_B K_A P_A = k_f P_A^{\alpha=1} P_B^{\beta=0} \quad \text{Eq 5.9}$$

$$k_f = k_s n_A n_B K_A = A e^{-\frac{E_t}{RT}} \quad \text{Eq 5.10}$$

In chapter 3, when Ni-based catalyst is modified by Lanthanum, due to strong interaction between CO₂ and La-Ni-Al oxide, CO₂ forms Lanthanum carbonates which increase oxygen-containing adsorbates. In this sense, CH₄ and CO₂ adsorption sites are fairly separated which supports zeroth-order dependence of CO₂ partial pressure. Meanwhile, complexity arises from

the fact that the interface between Ni and La-oxide also provides adsorption sites for both CH₄ and CO₂ [28]: strong interaction between CO₂ and La-oxide hinders CH₄ adsorption. Assume CH₄ and CO₂ share the same adsorption site, L-H formulation yields the negative reaction order for CO₂ (Eq 5.11). Applying the same approximation as $K_A P_A \ll 1$ and $K_B P_B \gg 1$; the reaction order for CO₂ takes the negative value when CH₄ and CO₂ share the same adsorption sites (Eq 5.12). The reaction order is correlated with the surface coverage of individual molecules. Results shown in Figure 5.2 explain general reforming behavior of CH₄/CO₂ bimolecular system on La-modified Ni/Al₂O₃ catalysts quite well.

$$r_{CH_4}' = k_s n \frac{K_A K_B P_A P_B}{(1 + K_A P_A + K_B P_B)^2} \quad \text{Eq 5.11}$$

$$r_{CH_4}' = k_s n \frac{K_A P_A}{K_B P_B} \propto P_A P_B^{-1} \quad \text{Eq 5.12}$$

5.4.3 Reaction order for plasma hybrid reaction

The reaction orders for CH₄ (α) and CO₂ (β) in the thermal catalysis have been obtained in last section. In the case of plasma catalysis, gas dilution must be avoided strictly because plasma-excited inert gas (such as N₂ and Ar) would induce unpredictable gas phase and surface reactions which lead to an inappropriate interpretation of kinetic data. Therefore, the reaction orders in plasma catalysis were measured under the condition that both CH₄ and CO₂ partial pressure were varied simultaneously.

Assume the power-law kinetics for the forward CH₄ reaction rate equation (Eq 5.13). By taking the natural logarithm of Eq 5.13 and rewrite it into Eq 5.14–5.16:

$$-\frac{dP_{CH_4}}{dt} = r_{CH_4} = k_f P_{CH_4}^{\alpha'} P_{CO_2}^{\beta'} \quad \text{Eq 5.13}$$

$$\ln r_{CH_4} = \ln k_f + \alpha' \ln P_{CH_4} + \beta' \ln P_{CO_2} \quad \text{Eq 5.14}$$

$$\ln \frac{r_{CH_4}}{P_{CO_2}^{\beta'}} \propto \alpha' \ln P_{CH_4} \quad \text{Eq 5.15}$$

$$\ln \frac{r_{CH_4}}{P_{CH_4}^{\alpha'}} \propto \beta' \ln P_{CO_2} \quad \text{Eq 1.16}$$

Here, k_f and P respectively express the forward reaction rate constant and the average concentration of CH_4 and CO_2 ; α' and β' represent the modified reaction orders in plasma catalysis. The α' and β' are not known at this point. Assume $\alpha' = \alpha$ and $\beta' = \beta$ as tentative values and performed iterative calculation until the deviation of α' and β' becomes smaller than 1% error.

Figure 5.3(a) expresses $\ln \frac{r_{CH_4}}{P_{CO_2}^{\beta'}}$ v.s. $\ln P_{CH_4}$ showing the linear relationship with and without DBD. Modified reaction order for CH_4 (α') is obtained from the slope of each line. Similarly, modified reaction order for CO_2 (β') is obtained from Figure 5.2(b) as summarized in Table 5.2 for all cases. In the case of 100 kHz DBD, data obtained in CH_4 rich condition ($CH_4/CO_2 > 1$) was excluded due to an unfavored side reaction, i.e. coke formation.

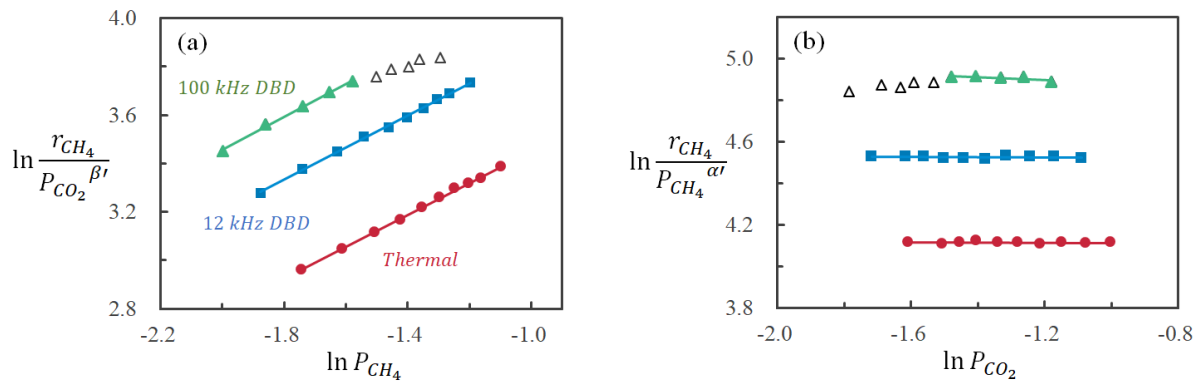


Figure 5.3 Modified reaction orders: (a) α' for CH_4 and (b) β' for CO_2 . Catalyst temperature was fixed at 600 °C for all cases. $SEI = 1.37$ eV/molecules for 12 kHz and 100 kHz DBD hybrid reaction. Total flow rate = 1,000 cm³/min (STP); GHSV = 5144 h⁻¹ (STP); Pressure = 5 kPa. Δ represents CH_4 rich condition.

Table 5.2 Reaction orders obtained from Figure 5.3.

	α'	α	β'	β
Thermal	0.66		-0.003	
12 kHz DBD	0.66	0.68*	-0.003	-0.17*
100 kHz DBD	0.68		-0.071	

* data from *section 5.4.1*

Comparing thermal and plasma catalysis, the reaction rate increases from thermal catalysis to 12 kHz DBD, and further promoted by 100 kHz DBD [26]. However, the modified reaction order for CH₄ is essentially unchanged by DBD. CH₄ chemisorption is promoted via vibrational excitation of CH₄: enhanced surface interaction might be measured as a smaller reaction order for CH₄ than that of thermal catalysis. However, as summarized in Table 5.2, modified reaction orders match quite well with that of thermal catalysis ($\alpha \approx \alpha'$). Although a remarkable contribution of vibrationally excited CH₄ increases the forward CH₄ reaction rate, the surface coverage by CH₄ is presumably low which satisfies $K_A P_A \ll 1$ (cf. section 5.4.2).

State-resolved molecular beam study revealed that the initial sticking probability (S_0) increases an order of magnitude when CH₄ is excited to the C-H stretching vibration mode [22]. However, the saturated surface coverage is determined as a function of S_0 , and not influenced by the vibrational excitation. CH₄ chemisorption via stretching vibrational excitation is fast and effective when the Ni surface is clean or fully vacant, and the adsorbed CH₄ fragments build up quickly up to the saturation state which hinders further CH₄ chemisorption. For example, saturated coverage by CH₃* over Pt(111) surface increases up to ca. 30%: another 30% is occupied by atomic hydrogen (H*), and the rest of 40% are kept vacant due to the lateral interference of surface CH₃* and H* [34]. Moreover, the surface coverage of dissociative products increases the energy barrier for successive chemisorption of incident CH₄ [34]. It

seems to be contradicted to the experimental observation where CH_4 conversion increased clearly by DBD at fixed catalyst temperature. Oxidation of CH_x^* is promoted by CO_2 -derived adsorbed oxygen which regenerate active sites for successive CH_4 chemisorption as chapter 4 depicted: it is no doubt that the simultaneous excitation of both CH_4 and CO_2 is the key to promoting overall reforming performance.

Modified reaction order for CO_2 at 12 kHz and thermal catalysis are close to zero because CO_2 adsorption is intrinsically strong without DBD [28, 31]. The reaction order changes from near zero to the negative in 100 kHz DBD case: the negative reaction order implies that CO_2 adsorption is strengthened by 100 kHz DBD and interferes CH_4 chemisorption [28, 29]. The important conclusion in Chapter 4 is confirmed here: not only CO_2 adsorption but also the formation of carbonate species are promoted by DBD [35] which is the important source of synergism enabled by nonthermal plasma. Although plasma-activated CO_2 hinders CH_4 conversion slightly, it is the important source of synergism enabled by nonthermal plasma because of two reasons: regeneration of active site for successive CH_4 chemisorption and the suppression of coking.

5.4.4 Arrhenius curve

The forward rate equation of CH_4 dry reforming is confirmed as Eq 5.17 – Eq 5.19. The A and E_t represent pre-exponential factor and the activation energy for thermal catalysis, respectively. Reaction order was essentially unchanged by DBD; therefore, $\alpha = 0.68$ and $\beta = -0.17$ were adopted for Arrhenius plot analysis. Table 5.3 shows the experimental conditions. Two frequencies were applied at constant input power and the flow rate, yielding the specific energy input of $SEI = 1.37$ eV/molecule. Furnace temperature was increased at a constant heating rate of $2^\circ\text{C}/\text{min}$, while the catalyst temperature was measured by thermography at constant interval. Plasma sustain voltage (U_{sus}) and mean discharge current ($I_{\text{p-p}}$) were

measured by Lissajous diagram which are also provided in Table 5.3; discharge power is proportional to $U_{\text{sus}} \times I_{\text{p-p}}$ [26].

$$r_{\text{CH}_4} = k_f P_{\text{CH}_4}^{0.68} P_{\text{CO}_2}^{-0.17} \quad \text{Eq 5.17}$$

$$k_f = A e^{-\frac{E_t}{RT}} \quad \text{Eq 5.18}$$

$$\ln(k_f) = -\frac{E_t}{RT} + \ln(A) \quad \text{Eq 5.19}$$

Table 5.3 Experimental conditions for Arrhenius plot analysis: 450 °C < Catalyst temperature < 670 °C. CH₄/CO₂ = 0.8, total pressure = 5 kPa. A small deviation of U_{sus} and $I_{\text{p-p}}$ was caused by different catalyst temperatures.

		Frequency	U_{sus}	$I_{\text{p-p}}/2$	Power	Total flow ^{*3}	SEI^{*3}	$GHSV^{*3}$
<i>Run</i>		(kHz)	(kV)	(mA)	(W)	(cm ³ /min)	(eV/molecule)	(h ⁻¹)
Plasma catalysis	A	12 ^{*1}	3.03 ^{+0.16} _{-0.21}	9.18 ^{+0.61} _{-0.47}	90	1,000	1.37	5,144
	B	100 ^{*2}	1.28 ^{+0.07} _{-0.13}	21.5 ^{+0.84} _{-0.81}				
Thermal catalysis	C			Not apply				

^{*1} Logy Electric; LHV-13AC, ^{*2} ASTECH; LG-10S RF Generator, ^{*3} STP (25 °C and 101 kPa)

Figure 5.4 shows the Arrhenius curve for three conditions (*Run A–C*). In the case of thermal catalysis, in the low-temperature regime, the reaction is characterized by a reaction-limited regime where the slop of the line expresses the activation energy of the forward CH₄

reaction rate. Activation energy for thermal catalysis yielded $E_t = 91$ kJ/mol which agrees well with reported value for CH_4 dry reforming [33]. In high-temperature, the activation energy is almost halved as summarized in Table 5.4. In the high-temperature regime, the apparent activation energy is determined by the combined effect of the surface reaction and the diffusion of molecules through porous pellets which is formulated by the effectiveness factor of the catalyst [36, 37]. The apparent reaction rate is decreased due to the mass transfer resistance in micropores. The diffusion-impacted apparent reaction rate is proportional to the square root of apparent reaction rate constant, yielding $E_{\text{app}} = E_t/2$ as formulated in Eq 5.20 which agrees well with the experimental observation. Here, D denotes the diffusion coefficient in the porous medium.

$$r_{\text{app}} \propto \sqrt{\frac{k_f}{D}} \propto e^{-\frac{E_t/2}{RT}} \quad \text{Eq 5.20}$$

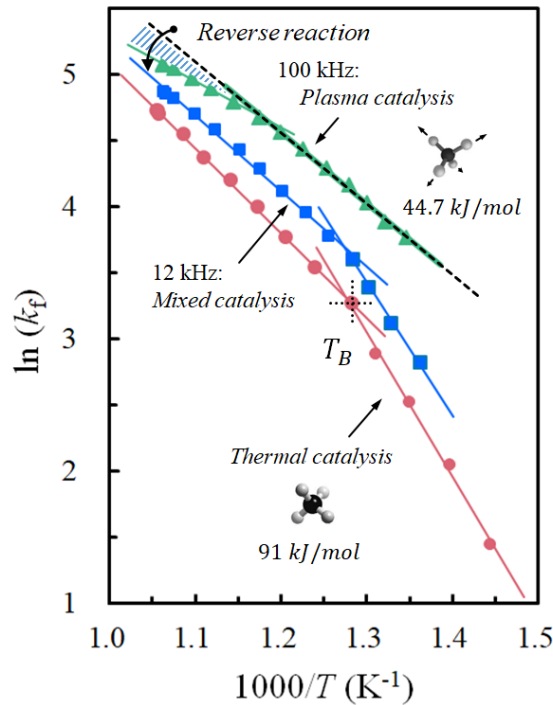


Figure 5.4 Arrhenius plot for thermal (●), mixed (■), and plasma catalysis (▲). The deviation due to the reverse reaction is highlighted by the shaded area.

Table 5.4 Activation energy and break temperature (T_B)

	T_B (°C)	Activation energy (kJ/mol)	
		$T < T_B$	$T > T_B$
Plasma catalysis (100 kHz DBD)	(580)	44.7	29.4
Mixed catalysis (12 kHz DBD)	510	83.2	47.6
Thermal catalysis	510	91.2	53.4

Similar to thermal catalysis, 12 kHz DBD hybrid reaction also exhibits a convex Arrhenius behavior where the reaction regime is separated at break temperature of $T_B = 510$ °C. Because DBD is a weakly ionized plasma, catalytic reaction due to ground state molecule occurs dominantly and the contribution of vibrationally excited species is relatively weak. In other words, 12 kHz DBD hybrid reaction is characterized as *mixed catalysis*. Convex behavior is explained by the mass transfer resistance in the micropores due to ground state CH_4 . The additional CH_4 conversion via vibrationally excited CH_4 occurs in parallel, yielding a larger rate constant compared to the thermal catalysis. Correspondingly, apparent activation energy is measured as slightly smaller value than thermal catalysis.

Almost identical Arrhenius behavior was observed in DBD-assisted CH_4 steam reforming [38]. Spherical 12wt%-Ni/ Al_2O_3 catalyst pellets were used and DBD was generated using 1–5 kHz bipolar pulsed high voltage. *SEI* was set to a small value (0.22–0.36 eV/molecule) to avoid excessive plasma heating. First, the activation energy for the thermal catalysis was $E_t = 102$ kJ/mol; activation of CH_4 is the rate-determining step and this value agrees well with the literature [39]. The activation energy was halved from 102 to 50 kJ/mol in the high-temperature regime (cf. Eq 5.20) at the break temperature of $T_B = 420$ °C. The Arrhenius curve for DBD

hybrid reaction shifts upward having slightly smaller activation energy than thermal reaction, indicating the DBD hybrid reaction is *mixed catalysis*.

Arrhenius behavior in 100 kHz DBD is unique. The reaction rate constant in the low-temperature regime is even greater than that of thermal catalysis in the high-temperature regime. Moreover, the break temperature at $T_B = 510\text{ }^\circ\text{C}$ is no longer observed. The observation implies that the overall reaction is dominated by the vibrationally excited molecules which increases reaction rate dramatically compared to thermal reaction. Such reaction occurs most likely in the 20 micrometers thin layer of the outer surface of pellets [40]: neither generation of DBD nor the diffusion of plasma-generated reactive species in the internal micropores is possible. Therefore, the effect of internal diffusion of the ground-state molecule, or the effectiveness factor, is intrinsically not applicable in 100 kHz DBD case.

Meanwhile, Arrhenius curve shows convexity at $580\text{ }^\circ\text{C}$. This is not related to the internal mass transfer resistance because DBD-induced reaction do not occur in the internal micropores. It is due to the excessive CH_4 and CO_2 conversion which approaches the thermal equilibrium. In that case, the rate equation must take into account reverse reaction (Eq 5.21) [33, 39]. K_e represents equilibrium constant for CH_4 dry reforming at given catalyst temperature. Obviously, the experimental measurement ($r_{\text{CH}_4}|_{\text{net}}$) underestimates the forward reaction rate near the thermal equilibrium: the rate constant is measured as smaller value when $T > 580\text{ }^\circ\text{C}$. We hypothesize that the Arrhenius curve in 100 kHz DBD is expressed as a dotted straight line without convex behavior, indicating that vibrationally excited CH_4 dominates dry reforming near the external surface of pellets over the entire temperature examined. Therefore, the Arrhenius curve expresses the plasma catalysis in the case of 100 kHz DBD. The activation energy ($E_p = 44.7\text{ kJ/mol}$) expresses the pure plasma catalysis.

$$r_{\text{CH}_4}|_{\text{net}} = r_{\text{CH}_4} \left(1 - \frac{1}{K_e} \frac{P_{\text{CO}}^2 P_{\text{H}_2}^2}{P_{\text{CH}_4} P_{\text{CO}_2}} \right) \quad \text{Eq 5.21}$$

5.5 State-specific CH₄ activation

According to the analysis of reaction orders and the activation energy, rate-determining step is the chemisorption of CH₄ which yielded the activation energy of $E_t = 91$ kJ/mol in thermal catalysis. The decrease in the activation energy by DBD is explained by the vibrational excitation of CH₄. Detailed kinetic study for state-specific vibrational excitation of CH₄ in terms of well-defined Ni surface has been performed by the molecular beam study. The vibrational efficacy (η) is defined by the Eq 5.22 [24]. The E_t (= 91 kJ/mol) represents the activation energy for thermal catalysis (plasma-off). The E_a^v is the apparent activation energy when the reaction of vibrationally excited CH₄ is superposed. The E_v expresses the vibrational activation threshold. The forward reaction rate constant for vibrationally excited species is modified by the temperature-dependent Arrhenius expression (Eq 5.23).

$$\eta = \frac{E_t - E_a^v}{E_v} \quad \text{Eq 5.22}$$

$$k_f = Ae^{-\frac{E_a^v}{RT}} = Ae^{-\frac{E_t - \eta E_v}{RT}} \quad \text{Eq 5.23}$$

Figure 5.5 schematically expresses the reaction coordinate with different activation energy barrier and the corresponding vibrational efficacy. The activation energy and the reaction enthalpy for CH₄ chemisorption over Ni (111) surface, as a model case, was obtained by density functional theory (DFT) analysis (R5.1) [41, 42]:



The C-H bond breaking requires a large activation energy barrier; however, the endothermic reaction enthalpy is relatively small. When CH₃* and H* adsorb separately without lateral interaction, assuming very low surface coverage, the reaction enthalpy takes the small value of 14 kJ/mol. In the case of co-adsorption of CH₃* and H* where the lateral interaction is not

negligible, the endothermic reaction enthalpy increases to 35 kJ/mol. Interestingly, the vibrational activation energy and the reaction enthalpy is of the same order; the internal vibrational energy would be utilized for overcoming energy barrier at low surface temperature. Moreover, possessing sufficient internal energy for supplying major part of endothermic energy if the vibrational energy dissipation is negligible during the course of the chemisorption dynamics [15, 43].

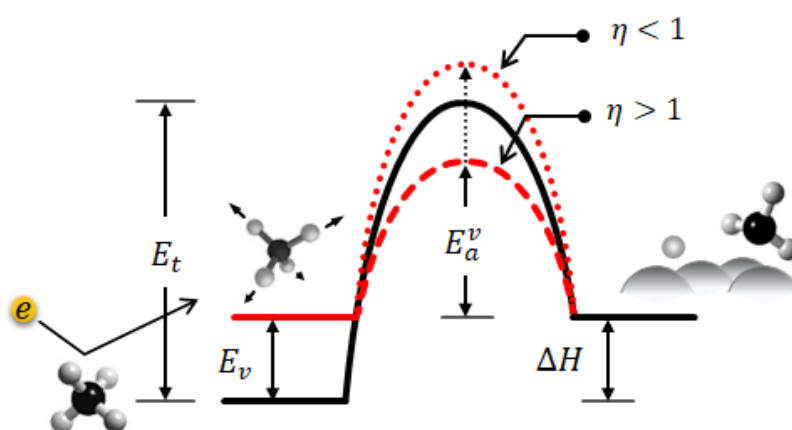


Figure 5.5 Reaction coordinate for dissociative CH₄ chemisorption on metal surface. Solid curve; ground state CH₄, Dotted curves; vibrationally excited CH₄ with different efficacy.

Similar equation with Eq 5.23 was studied for homogeneous 2-body reactions involving various vibrationally excited species [44]. In the case of homogeneous reaction, the efficacy takes the values between 0 and 1, yielding the lowest apparent activation energy of $E_t - E_v$ ($\eta = 1$) is possible. In contrast, the vibrational efficacy for the heterogeneous reaction would take the value greater than 1 ($\eta > 1$) [45], indicating the drastic decrease of the activation energy barrier is possible. Such unique reactivity is the source of synergism when nonthermal plasma is combined with heterogeneous catalysts.

CH₄ is excited vibrationally into four fundamental modes by the low-energy electron impact: ν_1 (361.7 meV) Symmetric stretch, ν_2 (190.2 meV) Twisting, ν_3 (374.3 meV)

Asymmetric stretch, ν_4 (161.9 meV) Scissoring. Electron energy-loss spectrum shows that excitation by electron impact into ν_4 and ν_1 modes is strong when the incident electron energy is as small as 0.1–1.5 eV, while weak excitation into ν_2 and ν_3 appears as shoulder peak of ν_4 and ν_1 [46]. Several overtones and combined vibrations such as $2\nu_4$, $\nu_1+\nu_4$, and $2\nu_1$ are possible; however, these excitation levels are ruled out as effective vibration mode due to a low excitation probability. For the analysis of electron impact reaction kinetics, collision cross section data set was obtained from ref [47, 48].

The apparent activation energy (E_a^v) for vibrationally excited CH₄ over various Ni surfaces was estimated using Eq 5.23 with the mode-specific vibrational efficacy provided in ref. [45]. Vibrational efficacy on Pt [34, 49] and Ir [50] surfaces is also provided in Figure 5.6 for comparison. The CH₄(ν_1) mode has the second largest excitation probability in nonthermal plasma which leads to $E_a^v = 42$ kJ/mol on the Ni(100) surface. Contribution of CH₄(ν_3) is also significant due to a large vibrational efficacy which leads the activation energy of 57 kJ/mol and 46 kJ/mol respectively on Ni(100) and Ni(111) surfaces. The apparent activation energy would decrease from 91 to 42–57 kJ/mol as a result of multiple stretching vibrational excitations reacting over multiple Ni facets. Indeed, CH₄(ν_1) and CH₄(ν_3) are the major vibrationally excited mode by low-energy electron impact. The activation energy of 44.7 kJ/mol obtained in 100 kHz DBD case is quite reasonable. Note, in the case of 12 kHz DBD, direct comparison of activation energy is not feasible because the results represent *mixed catalysis*.

Overtone stretching vibration mode such as CH₄($2\nu_3$) also exhibits large vibrational efficacy, leading to the activation energy of as small as 23–27 kJ/mol; however, direct excitation of ground state CH₄ to $2\nu_3$ mode is hardly observed by the low energy electron impact. Therefore, such small activation energy is ruled out as an effective reaction enhancement pathway. The vibrational efficacy of bending vibration mode is smaller than that

of stretching mode, yielding activation energy of 59–69 kJ/mol via overtone vibration $\text{CH}_4(3\nu_4)$. In overall, activation energy via vibrationally excited CH_4 ranges from 42–69 kJ/mol, which is relatively well correlated with experimental measurement of 44.7 kJ/mol.

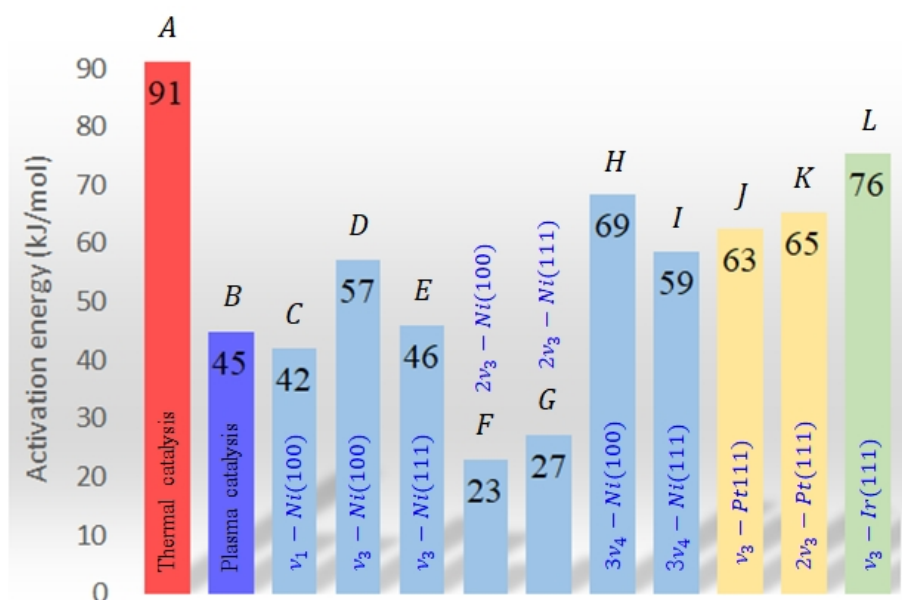


Figure 5.6 Activation energy of vibrationally excited CH_4 reacting over Ni [45], Pt [34, 49], and Ir [50] surfaces. *A–B*; this work, *C–E*; ν_1 and ν_3 on Ni, *F–I*; overtone on Ni, *J–L*; other metal surface (Pt, Ir).

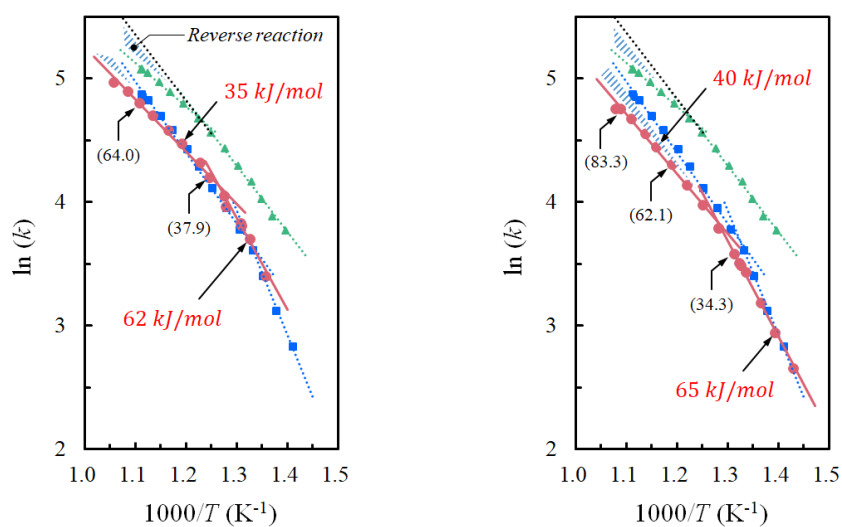
5.6 Correlation between kinetic and plasma parameters

In order to investigate *SEI* dependence, plasma catalysis at higher energy density (*SEI* = 2.0 eV/molecule) was performed by increasing the input power (*Run D* in Table 5.5) or decreasing the total flow rate (*Run E*). All experiments were carried out at $\text{CH}_4/\text{CO}_2 = 0.8$ without dilution gas. In order to avoid plasma heating due to excess energy input, *SEI* was set to smaller than specific energy requirement (*SER*) of CH_4 dry reforming ($\text{CH}_4 + \text{CO}_2 = 2\text{H}_2 + 2\text{CO}$; $\text{SER} = \Delta H = 247 \text{ kJ/mol} = 2.56 \text{ eV/molecule}$). Reaction conditions and the Arrhenius plots are presented respectively in Table 5.5 and Figure 5.7.

Table 5.5 Experimental conditions for Arrhenius plot analysis: $440^{\circ}\text{C} < \text{catalyst temperature} < 735^{\circ}\text{C}$; CH_4/CO_2 ratio = 0.8; total pressure = 5 kPa; $GHSV = 5,144 \text{ h}^{-1}$.

<i>Run</i>	Frequency (kHz)	\bar{U}_{sus} (kV)	$I_{p-p}/2$ (mA)	Power (W)	Total flow ^{*3} (cm ³ /min)	<i>SEI</i> ^{*4} (eV/molecule)
A (Control)	12 ^{*1}	$3.03^{+0.16}_{-0.21}$	$9.18^{+0.61}_{-0.47}$	90	1,000	1.37
B (Control)	100 ^{*2}	$1.28^{+0.07}_{-0.13}$	$21.5^{+0.84}_{-0.81}$	90	1,000	1.37
D	15 ^{*3}	$3.15^{+0.25}_{-0.15}$	$12.5^{+1.27}_{-1.17}$	130	1,000	2.0
E	12 ^{*1}	$3.05^{+0.23}_{-0.35}$	$9.19^{+0.67}_{-0.94}$	90	700	2.0

^{*1} Logy Electric; LHV-13AC, ^{*2} ASTECH; LG-10S RF Generator, ^{*3} Tamaoki Electronics; TE-HFV1520K-0400, ^{*4} STP (25 °C and 101 kPa)



(a) $SEI = 2.0$, Run D (Red circle) (b) $SEI = 2.0$, Run E (Red circle)

Figure 5.7 Arrhenius plot: (a) $SEI = 2.0$, Run D (Red circle), (b) $SEI = 2.0$, Run E (Red circle).

Run A: Blue square (12 kHz, $SEI = 1.37$ eV/molecule), Run B: Green triangle (100 kHz, $SEI =$

1.37 eV/molecule) in all Figures. The number in parenthesis indicates CH₄ conversion (%) for Red circle. The deviation due to reverse reaction is highlighted by the shades.

In the case of *Run D* (Figure 5.7 (a), $SEI = 2.0$ eV/molecule), Arrhenius curve also overlaps with that of *Run A* ($SEI = 1.37$ eV/molecule). However, an exact value of apparent activation energy decreases slightly because the contribution of vibrationally excited CH₄ would be enhanced to some extent by increasing SEI . Similarly, Figure 5.7 (b) represents almost identical results between *Run A* and *Run E* in the low-temperature regime. However, there is a clear deviation in high temperature. CH₄ conversion at *Run E* ($SEI = 2.0$ eV/molecule) approaches to the thermal equilibrium when $T > T_B$. In that case, measured reaction rate underestimates forward CH₄ reaction rate because the reverse reaction was not taken into account. This phenomenon is similar to 100 kHz DBD case (Figure 5.4) where the reaction rate constant is measured as smaller value when $T > 580$ °C due to the limitation of equilibrium.

DBD is characterized as a swarm of filamentary microdischarges (known as streamers) with nanosecond duration (1–10 ns) [51]. Dynamics behavior of streamer propagation in a packed-bed DBD reactor has been studied extensively by Kim *et al* [52]. Figure 5.8 shows the streamers generated by the nanosecond high-voltage pulses on Ag/Al₂O₃ catalyst pellets in air. Streamers are known to propagate in close contact with catalyst pellet, enabling better interaction between plasma-generated reactive species and catalyst materials. Electron number density and electron energy in each streamer is the key determining factors for the ionization, dissociation, and excitation of molecules. Particularly in CH₄ reforming, the generation of vibrationally excited CH₄ in streamers is the key to enhancing the rate-determining step as schematically depicted in Figure 5.8. The k_f represents the forward rate constant for the rate-determining step (CH₄ chemisorption).

However, it is hardly probing to an individual streamer by the measurement due to a highly

localized and transient nature of streamers: time- and space-averaged properties of *streamer swarm* are characterized by plasma sustain voltage (U_{sus}) and mean discharge current ($I_{\text{p-p}}$) via the Lissajous diagram analysis [3, 51]. The electron collision rate coefficient (k_e) for ionization, dissociation, and excitation of molecules is determined as a function of the reduced electric field (E/N_g) (Eq 5.24) [53]. The E expresses the electric field acting over the gas gap. The d (m) represents the characteristic length which is determined generally by the gas gap between electrodes. N_g is number density of molecules at given temperature and pressure, which could be calculated by Eq 5.25 [54], where P , N_A , R and T represent gas pressure, Avogadro constant, gas constant and gas temperature, respectively.

$$k_e = f\left(\frac{E}{N_g}\right) = f\left(\frac{U_{\text{sus}}/d}{N_g}\right) \quad \text{Eq 5.24}$$

$$N_g = \frac{P \times N_A}{R \times T} \quad \text{Eq 5.25}$$

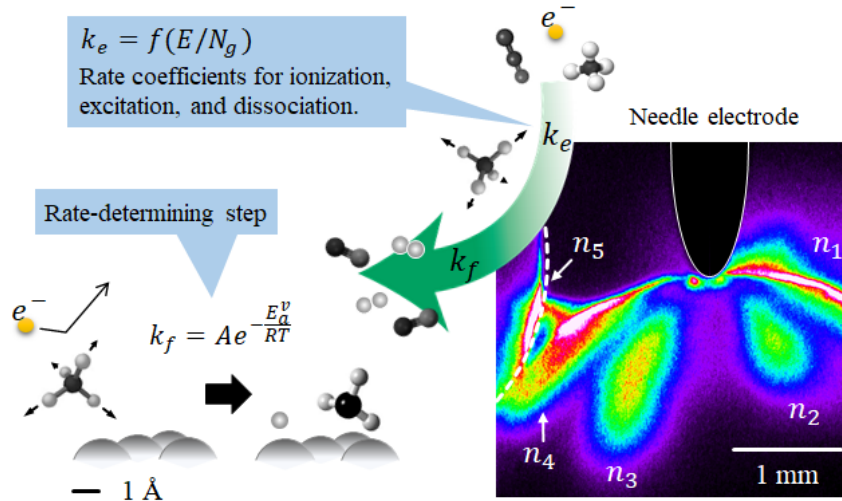


Figure 5.8 Streamer discharges on $\text{Ag}/\text{Al}_2\text{O}_3$ catalyst pellets in air generated by nanosecond high-voltage to the needle electrode [52] (room temperature and atmospheric pressure). The image shows 50 times accumulation of 10 ns exposure imaging, showing multiple streamers (n_1 – n_5).

As shown in Table 5.5, U_{sus} is almost unchanged by either increasing input power or decreasing gas flow rate when the operating frequency was 12–15 kHz. Electrical properties of DBD is almost unchanged by SEI because electron collision rate coefficients would not change to a large extent under the same U_{sus} . Therefore, the effect of SEI on Arrhenius curve is undistinguishable when the frequency was 12–15 kHz. In contrast, electrical properties of DBD at 100 kHz is quite different: U_{sus} decreases by half and $I_{\text{p-p}}$ is doubled (*Run B* in Table 5.3 and 5.5; see also Chapter 4 [26]). Low-energy electrons are preferred to generate vibrationally excited CH_4 [26]. Obviously, the contribution of vibrationally excited CH_4 in 100 kHz DBD is greater than that of 12 kHz DBD. The overall reaction is considered to be plasma catalysis (not *mixed catalysis*) as discussed in section 5.4.4. Arrhenius plot for 100 kHz DBD is categorized as a different curve even if SEI takes the same value such as $SEI = 1.37$ eV/molecule.

CH_4 chemisorption is known to be the rate-determining step which is characterized by the activation energy (E_t , kJ/mol). When vibrationally excited CH_4 is generated in streamers and interacts with the catalyst surface (cf. Figure 5.8), apparent activation energy decreases from E_t to E_a^v (cf. Figure 5.5) depending on the vibrational excitation mode, Ni crystal orientation, and the vibrational efficacy (section 5.5). Because streamer formation is spatially discrete, reaction enhancement by DBD is localized where the streamer attaches the catalyst surface. In contrast, thermal reaction occurs in parallel where no streamer is generated. In other words, apparent activation energy reflects a combined effect of thermal and plasma catalysis which is defined as *mixed catalysis*. As input power increases, contribution of vibrationally excited CH_4 increases which is measured as a smaller activation energy

5.7 Conclusion

Electron impact excitation of feed gas molecules occurring in a single streamer is the key determining factors of kinetic parameters such as reaction rate constant, the activation energy, and the reaction orders. Meanwhile, a number of streamers generated per unit time determine the net flux of reactive species to the catalyst surface, which in turn influences the apparent activation energy measured by the Arrhenius plot. The 12 kHz DBD is characterized as *mixed catalysis* where thermal catalysis occurs dominantly and a weak interaction of plasma-induced reaction is possible. In contrast, 100 kHz DBD is regarded as pure *plasma catalysis* due to the significant contribution of vibrationally excited CH_4 to the surface reaction. A drastic modification of U_{sus} and $I_{\text{p-p}}$ is possible by 100 kHz DBD (Table 5.3), yielding nearly two-time more vibrationally excited species than 12 kHz DBD [26]. In that case, Arrhenius behavior is clearly distinguished from 12 kHz DBD case even if SEI was maintained at the same value as $SEI = 1.37$ eV/molecule. Considering vibrational efficacy provided by the state-specific gas-surface reactivity of vibrationally excited CH_4 , the activation energy is estimated to be 42–69 kJ/mol which agrees well with this experimental measurement in 100 kHz DBD case (44.7 kJ/mol). If the activation energy is measured as smaller than this value, either the mass transfer resistance or the reverse reaction (limitation of thermodynamic equilibrium) must be taken into account in the model.

In the case of mixed catalysis (12 kHz DBD case), apparent activation energy cannot be compared directly with state-resolved molecular beam study; because contribution of thermal and plasma catalysis is not decoupled. Activation energy slightly decreases by increasing SEI ; however, effect of SEI is negligibly small under the fixed frequency of 12–15 kHz simply because the electrical properties of DBD is almost unchanged.

Although vibrationally excited CH_4 is the preliminary important step for enhanced performance of CH_4 dry reforming, co-activation of CO_2 is also the key factor because the

adsorbed CH₄ fragment must be oxidized and removed by CO₂-derived oxygen-containing surface species; active sites are regenerated for the successive CH₄ chemisorption which is the key to enhancing overall reforming performance. Moreover, Chapter 3 has confirmed that lanthanum-modification of Ni/Al₂O₃ catalysts plays the key role to enhance the surface interaction with plasma-activated CO₂. Plasma-catalyst synergy was not as strong when Ni/Al₂O₃ catalyst (without Lanthanum promoter) was applied to DBD hybrid reaction [55]. The combination of appropriate catalyst materials, together with plasma activation of co-reactant, must be optimized for further improvement of plasma catalysis of CH₄ dry reforming.

5.8 References

- [1] M. Scapinello, E. Delikonstantis, G.D. Stefanidis, The panorama of plasma-assisted non-oxidative methane reforming, *Chemical Engineering and Processing: Process Intensification* 117 (2017) 120-140.
- [2] Z. Zakaria, S.K. Kamarudin, Direct conversion technologies of methane to methanol: An overview, *Renewable and Sustainable Energy Reviews* 65 (2016) 250-261.
- [3] T. Nozaki, S. Kameshima, Z. Sheng, K. Tamura, T. Yamazaki, in: X. Tu, J.C. Whitehead, T. Nozaki (Eds.), *Plasma Catalysis: Fundamentals and Applications*, Springer International Publishing, Cham, 2019, pp. 231-269.
- [4] Y.X. Zeng, L. Wang, C.F. Wu, J.Q. Wang, B.X. Shen, X. Tu, Low temperature reforming of biogas over K-, Mg- and Ce-promoted Ni/Al₂O₃ catalysts for the production of hydrogen rich syngas: Understanding the plasma-catalytic synergy, *Applied Catalysis B: Environmental* 224 (2018) 469-478.
- [5] S. Kameshima, K. Tamura, Y. Ishibashi, T. Nozaki, Pulsed dry methane reforming in plasma-enhanced catalytic reaction, *Catalysis Today* 256 (2015) 67-75.
- [6] H. Lee, D.H. Kim, Direct methanol synthesis from methane in a plasma-catalyst hybrid system at low temperature using metal oxide-coated glass beads, *Scientific Reports* 8 (2018) 9956.
- [7] S.T. Wismann, J.S. Engbæk, S.B. Vendelbo, F.B. Bendixen, W.L. Eriksen, K. Aasberg-Petersen, C. Frandsen, I. Chorkendorff, P.M. Mortensen, Electrified methane reforming: A compact approach to greener industrial hydrogen production, *Science* 364 (2019) 756.
- [8] X. Guo, G. Fang, G. Li, H. Ma, H. Fan, L. Yu, C. Ma, X. Wu, D. Deng, M. Wei, D. Tan, R. Si, S. Zhang, J. Li, L. Sun, Z. Tang, X. Pan, X. Bao, Direct, nonoxidative conversion of methane to ethylene, aromatics, and hydrogen, *Science* 344 (2014) 616.

- [9] M. Ravi, M. Ranocchiari, J.A. van Bokhoven, The direct catalytic oxidation of methane to methanol—A critical assessment, *Angewandte Chemie International Edition* 56 (2017) 16464-16483.
- [10] R. Zhou, R. Zhou, Y. Xian, Z. Fang, X. Lu, K. Bazaka, A. Bogaerts, K. Ostrikov, Plasma-enabled catalyst-free conversion of ethanol to hydrogen gas and carbon dots near room temperature, *Chemical Engineering Journal* 382 (2020) 122745.
- [11] B. Huang, C. Zhang, H. Bai, S. Zhang, K. Ostrikov, T. Shao, Energy pooling mechanism for catalyst-free methane activation in nanosecond pulsed non-thermal plasmas, *Chemical Engineering Journal* 396 (2020) 125185.
- [12] X. Wang, Y. Gao, S. Zhang, H. Sun, J. Li, T. Shao, Nanosecond pulsed plasma assisted dry reforming of CH₄: The effect of plasma operating parameters, *Applied Energy* 243 (2019) 132-144.
- [13] T. Nozaki, K. Okazaki, Non-thermal plasma catalysis of methane: Principles, energy efficiency, and applications, *Catalysis Today* 211 (2013) 29-38.
- [14] P. Mehta, P. Barboun, D.B. Go, J.C. Hicks, W.F. Schneider, Catalysis enabled by plasma activation of strong chemical bonds: A review, *ACS Energy Letters* 4 (2019) 1115-1133.
- [15] P.R. Shirhatti, I. Rahinov, K. Golibrzuch, J. Werdecker, J. Geweke, J. Altschäffel, S. Kumar, D.J. Auerbach, C. Bartels, A.M. Wodtke, Observation of the adsorption and desorption of vibrationally excited molecules on a metal surface, *Nature Chemistry* 10 (2018) 592-598.
- [16] J. Quan, F. Muttaqien, T. Kondo, T. Kozarashi, T. Mogi, T. Imabayashi, Y. Hamamoto, K. Inagaki, I. Hamada, Y. Morikawa, J. Nakamura, Vibration-driven reaction of CO₂ on Cu surfaces via Eley–Rideal-type mechanism, *Nature Chemistry* 11 (2019) 722-729.
- [17] M. Kawasaki, T. Morita, K. Tachibana, Facile carbon fixation to performic acids by water-sealed dielectric barrier discharge, *Scientific Reports* 5 (2015) 14737.
- [18] P.M. Hundt, B. Jiang, M.E. van Reijzen, H. Guo, R.D. Beck, Vibrationally promoted dissociation of water on Ni(111), *Science* 344 (2014) 504.
- [19] G.C. Schatz, Stretched water is more reactive, *Science* 290 (2000) 950.
- [20] B.S. Patil, Q. Wang, V. Hessel, J. Lang, Plasma N₂-fixation: 1900–2014, *Catalysis Today* 256 (2015) 49-66.
- [21] K.H.R. Rouwenhorst, H.-H. Kim, L. Lefferts, Vibrationally excited activation of N₂ in plasma-enhanced catalytic ammonia synthesis: A kinetic analysis, *ACS Sustainable Chemistry & Engineering* 7 (2019) 17515-17522.
- [22] B. Jackson, S. Nave, The dissociative chemisorption of methane on Ni(111): The effects of molecular vibration and lattice motion, *The Journal of Chemical Physics* 138 (2013) 174705.
- [23] A.L. Utz, Vibrations that live long and prosper, *Nature Chemistry* 10 (2018) 577-578.
- [24] R.R. Smith, D.R. Killelea, D.F. DelSesto, A.L. Utz, Preference for vibrational over

- translational energy in a gas-surface reaction, *Science* 304 (2004) 992.
- [25] J. Quan, T. Kondo, G. Wang, J. Nakamura, Energy transfer dynamics of formate decomposition on Cu(110), *Angewandte Chemie International Edition* 56 (2017) 3496-3500.
 - [26] Z. Sheng, K. Sakata, Y. Watanabe, S. Kameshima, H.-H. Kim, S. Yao, T. Nozaki, Factors determining synergism in plasma catalysis of biogas at reduced pressure, *Journal of Physics D: Applied Physics* 52 (2019) 414002.
 - [27] Y. Du, K. Tamura, S. Moore, Z. Peng, T. Nozaki, P.J. Bruggeman, CO($B^1\Sigma^+ \rightarrow A^1\Pi$) angstrom system for gas temperature measurements in CO₂ containing plasmas, *Plasma Chemistry and Plasma Processing* 37 (2017) 29-41.
 - [28] G. Sierra Gallego, C. Batiot-Dupeyrat, J. Barrault, F. Mondragón, Dual active-site mechanism for dry methane reforming over Ni/La₂O₃ produced from LaNiO₃ perovskite, *Industrial & Engineering Chemistry Research* 47 (2008) 9272-9278.
 - [29] T. Osaki, T. Mori, Role of potassium in carbon-free CO₂ reforming of methane on K-promoted Ni/Al₂O₃ catalysts, *Journal of Catalysis* 204 (2001) 89-97.
 - [30] H.M. Christina Papadopoulou, and Xenophon Verykios, Chapter 3: Utilization of biogas as a renewable carbon source: Dry reforming of methane, *Catalysis for Alternative Energy Generation*, Springer, New York, 2012, pp.57–127.
 - [31] J. Gao, Z. Hou, H. Lou, X. Zheng, in: D. Shekhawat, J.J. Spivey, D.A. Berry (Eds.), *Fuel Cells: Technologies for Fuel Processing*, Elsevier, Amsterdam, 2011, pp. 191-221.
 - [32] S. Wang, A comprehensive study on carbon dioxide reforming of methane over Ni/ γ -Al₂O₃ catalysts, *Industrial & Engineering Chemistry Research* 38 (1999) 2615-2625.
 - [33] U. Olsbye, T. Wurzel, L. Mleczko, Kinetic and reaction engineering studies of dry reforming of methane over a Ni/La/Al₂O₃ catalyst, *Industrial & Engineering Chemistry Research* 36 (1997) 5180-5188.
 - [34] H. Ueta, L. Chen, R.D. Beck, I. Colón-Díaz, B. Jackson, Quantum state-resolved CH₄ dissociation on Pt(111): coverage dependent barrier heights from experiment and density functional theory, *Physical Chemistry Chemical Physics* 15 (2013) 20526-20535.
 - [35] S. Xu, S. Chansai, Y. Shao, S. Xu, Y. Wang, S. Haigh, Y. Mu, Y. Jiao, C. Stere, H. Chen, X. Fan, C. Hardacre, Mechanistic study of non-thermal plasma assisted CO₂ hydrogenation over Ru supported on MgAl layered double hydroxide, *Applied Catalysis B: Environmental* 268 (2020) 118752.
 - [36] H. S. Fogler, in *Elements of chemical reaction engineering*, 5th edn, Englewood Cliffs, NJ: Prentice Hall, 2016, pp. 719-766.
 - [37] S. Kameshima, R. Mizukami, T. Yamazaki, L.A. Prananto, T. Nozaki, Interfacial reactions between DBD and porous catalyst in dry methane reforming, *Journal of Physics D: Applied Physics* 51 (2018) 114006.
 - [38] T. Nozaki, H. Tsukijihara, W. Fukui, K. Okazaki, Kinetic analysis of the catalyst and

- nonthermal plasma hybrid reaction for methane steam reforming, *Energy & Fuels* 21 (2007) 2525-2530.
- [39] J. Wei, E. Iglesia, Isotopic and kinetic assessment of the mechanism of reactions of CH₄ with CO₂ or H₂O to form synthesis gas and carbon on nickel catalysts, *Journal of Catalysis* 224 (2004) 370-383.
- [40] Z. Sheng, S. Kameshima, S. Yao, T. Nozaki, Oxidation behavior of Ni/Al₂O₃ catalyst in nonthermal plasma-enabled catalysis, *Journal of Physics D: Applied Physics* 51 (2018) 445205.
- [41] S.-G. Wang, D.-B. Cao, Y.-W. Li, J. Wang, H. Jiao, Reactivity of surface OH in CH₄ reforming reactions on Ni(111): A density functional theory calculation, *Surface Science* 603 (2009) 2600-2606.
- [42] H. Liu, B. Wang, M. Fan, N. Henson, Y. Zhang, B.F. Towler, H. Gordon Harris, Study on carbon deposition associated with catalytic CH₄ reforming by using density functional theory, *Fuel* 113 (2013) 712-718.
- [43] R. Moiraghi, A. Lozano, E. Peterson, A. Utz, W. Dong, H.F. Busnengo, Nonthermalized precursor-mediated dissociative chemisorption at high catalysis temperatures, *The Journal of Physical Chemistry Letters* 11 (2020) 2211-2218.
- [44] A. Fridman, *Plasma Chemistry*, Cambridge University Press, Cambridge, 2008.
- [45] A.L. Utz, Mode selective chemistry at surfaces, *Current opinion in solid state and materials science* 13 (2009) 4-12.
- [46] M. Allan, Excitation of the four fundamental vibrations of CH₄ by electron impact near threshold, *Journal of Physics B: Atomic, Molecular and Optical Physics* 38 (2005) 1679-1685.
- [47] W.L. Morgan, A critical evaluation of low-energy electron impact cross sections for plasma processing modeling. II: Cl₄, SiH₄, and CH₄, *Plasma Chemistry and Plasma Processing* 12 (1992) 477-493.
- [48] MORGAN database. <http://www.lxcat.laplace.univ-tlse.fr> (retrieved 4 June 2013).
- [49] R. Bisson, M. Sacchi, T.T. Dang, B. Yoder, P. Maroni, R.D. Beck, State-resolved reactivity of CH₄(2v₃) on Pt(111) and Ni(111): Effects of barrier height and transition state location, *The Journal of Physical Chemistry A* 111 (2007) 12679-12683.
- [50] E. Dombrowski, E. Peterson, D. Del Sesto, A.L. Utz, Precursor-mediated reactivity of vibrationally hot molecules: Methane activation on Ir(111), *Catalysis Today* 244 (2015) 10-18.
- [51] U. Kogelschatz, Dielectric-barrier discharges: Their history, discharge physics, and industrial applications, *Plasma Chemistry and Plasma Processing* 23 (2003) 1-46.
- [52] H.-H. Kim, Y. Teramoto, A. Ogata, Time-resolved imaging of positive pulsed corona-induced surface streamers on TiO₂ and γ -Al₂O₃-supported Ag catalysts, *Journal of Physics D: Applied Physics* 49 (2016) 415204.

- [53] A. Fridman, A. Chirokov, A. Gutsol, Non-thermal atmospheric pressure discharges, *Journal of Physics D: Applied Physics* 38 (2005) R1-R24.
- [54] D. Adrianto, Z. Sheng, T. Nozaki, Mechanistic study on nonthermal plasma conversion of CO₂, *International Journal of Plasma Environmental Science and Technology* 14 (2020) e01003 (9pp).
- [55] S. Kameshima, K. Tamura, R. Mizukami, T. Yamazaki, T. Nozaki, Parametric analysis of plasma-assisted pulsed dry methane reforming over Ni/Al₂O₃ catalyst, *Plasma Processes and Polymers* 14 (2017) 1600096.

Chapter 6: Conclusion and future work

6.1 Conclusions

This thesis concentrates on the CO₂ and CH₄ activation behavior in nonthermal plasma-catalyst interface, aiming for an interpretation of enhancement mechanism in nonthermal plasma-enabled methane dry reforming (MDR). The DBD (dielectric barrier discharge) provides vibrationally excited species (e.g. CO₂^v and CH₄^v) by low-energy electron impact in nonthermal plasma-enabled MDR. Two kinds of nickel-based catalysts were employed to investigate the CO₂-Ni and CO₂-La interaction, respectively. DBD-activated CO₂ shows enhancement for oxygen-contained species uptake over Ni and La respectively, which further influence the coke formation behavior and the oxidation of adsorbed CH₄ fragments (CH_x^{*}), respectively. The low and high frequency DBD were employed to reveal the influence of the electrical properties on overall reforming behaviors by Lissajous plot analysis and electron-molecule collisions theory. The kinetic analysis was carried out to reveal a plasma-enabled mode-selective CH₄ activation over the Ni catalyst. This current work provides a fundamental discussion towards nonthermal plasma-enhanced methane dry reforming based on microscopic surface chemistry, and macroscopic kinetic analysis and electron collision kinetics.

In chapter 2, the oxidation behavior of Ni/Al₂O₃ catalyst by DBD-activated CO₂ was investigated compared with CO₂ thermal oxidation. Quantitative analysis of *Temperature programmed reaction spectrometry* reveals plasma oxidation is much stronger than thermal oxidation. The distribution of NiO over the cross-section of catalyst pellets (spherical 3 mm mean diameter) was analyzed by Raman spectroscopy. Two Ni oxidation pathways were distinguished based on the *SEI*. When *SEI* is sufficiently small (< 1 eV/molecule), direct oxidation by DBD-activated CO₂ becomes the main oxidation route which significantly oxidizes Ni to NiO, where oxidation amount was much higher than corresponding thermal

oxidation. Since NiO thin layer was formed in the external surface during plasma oxidation with the thickness of ca. 20 micrometers, both DBD generation and DBD-activated species penetration into the internal pores are inhibited. Due to the formation of NiO, catalyst uptakes oxygen beyond thermal equilibrium known as Langmuir isotherm. The NiO thin layer drives the oxidation-reduction cycle in the plasma catalysis of MDR, where ground state CH_4 is dehydrogenated almost fully within the 20 μm NiO shell before further diffusion into internal pores.

In chapter 3, La-modified $\text{Ni}/\text{Al}_2\text{O}_3$ was employed to investigate surface adsorbed oxygen-contained species formation behaviors over La compared with non-La-adding $\text{Ni}/\text{Al}_2\text{O}_3$. In-situ plasma-DRIFTS and ex-situ CO_2 -TPD study were carried out to understand the plasma and catalyst interfacial phenomena. Nonthermal plasma can enhance CO_2 activation on La, leading to more surface carbonate species formation than that in thermal catalysis. Moreover, bicarbonate and bridge carbonate can be generated by DBD-activated CO_2 treatment. Due to the characteristics of the neighboring distribution on the atomic scale between Ni and La in the $\text{La-Ni}/\text{Al}_2\text{O}_3$, the CO_2 -La-derived carbonate species oxidize CH_x^* on Ni to generate syngas. The synergism of nonthermal plasma-enabled reforming is explained by the DBD-enhanced surface carbonate generation: enhanced surface carbonates accelerate surface reaction between CH_x^* species. Regeneration of active sites for following CH_4 chemisorption is promoted towards a higher CH_4 conversion.

In chapter 4, the basic property of methane dry reforming was presented based on low and high frequency packed bed DBD reactor. The discharge behaviors by Lissajous plot and electron collision kinetics were investigated comprehensively. The 100 kHz-DBD leads the highest reactant conversion and product yield, followed by 12 kHz-DBD, and both of DBD hybrid reforming show a significant enhancement than thermal reforming. The power-determining parameters are decoupled into plasma sustain voltage (\bar{U}_{sus}) and mean discharge

current (I_{p-p}). The effect of frequency on I_{p-p} is tremendous. Besides, 100 kHz DBD is operated in the low \bar{U}_{sus} and high I_{p-p} regime, while 12 kHz DBD is operated high \bar{U}_{sus} and low I_{p-p} regime. The increase in discharge current is critically important to emerge nonthermal plasma-induced synergism, while an increase in mean electron energy seems to be a minor effect. Generation of vibrationally excited species are the dominant electron-molecule collision pathways. Production rate of vibrationally excited species are correlated well with the net increase in CH₄ conversion.

In chapter 5, a kinetic analysis of methane dry reforming was investigated to elucidate the drastic reaction promotion mechanism enabled by plasma-catalyst interaction. Reaction order for CH₄ and CO₂ were determined respectively as 0.68 and -0.17, which were kept unchanged by DBD, indicating the surface coverage of CH₄ and CO₂ was not influenced by nonthermal plasma. The Arrhenius plot for forward CH₄ rate constant revealed that 12 kHz DBD hybrid reaction is characterized as *mixed catalysis* where plasma and thermal catalysis are not decoupled. In contrast, 100 kHz DBD is regarded as *pure plasma catalysis* where DBD-activated species dominates surface reaction, contributing to a decrease of activation energy from 91 to 45 kJ/mol. Such result is well correlated with molecule beam study where activation energy via vibrationally excited CH₄ ranges 42–69 kJ/mol on various Ni surfaces, illustrating vibrationally excited CH₄ plays the key role in pure plasma catalysis towards activation energy decrease.

6.2 Future work

First, exploring new types of catalysts is an important future work. Based on the results in Chapter 2 and Chapter 3, modification of catalyst is a promising approach to improve of CH₄ or CO₂ activation under nonthermal plasma. For a bimolecular-attended heterogeneous system, a good-performance catalyst should supply the active sites both for CH₄ and CO₂ activation simultaneously. Moreover, these two kinds of active site should be avoided for “long-distance” distribution. Otherwise, the surface reaction is difficult. The bimetallic or alloyed catalyst are promising to lead future works, which may convert “nano-scale” study of metallic crystal into “Ångstrom-scale” or even “atomic-scale” study. In this case, unambiguous mechanism is expected to be built based on experimental and simulation study (e.g. Density functional theory [1]).

The research of oxygen species fixation in catalyst may be an interesting topic in plasma catalysis. The carbon from CH₄ dehydrogenation is readily dissolved into Ni catalyst particles, and forms a core-shell like carbon-rich solid solute (e.g. NiC) [2]. It should be noted that the lattice oxygen (i.e. NiO) could contribute to the coke suppress (Chapter 2). The nickel-based oxidation-reduction have been demonstrated by Ref.[3] that a certain level of surface oxygen can optimize the utilization of CH₄ and improve the coking resistance. In our study, the lattice oxygen (NiO) enhanced by plasma seems active to suppress NiC, while it is inert for CH₄ derived adsorbed species: CH₄ conversion was not affected by plasma although NiO layer in Ni/Al₂O₃ catalyst was generated under plasma-activated CO₂. Besides, the reactivity of NiO in methane dry reforming has not been evaluated, although the relationship between oxidation behavior and coke formation behavior have been demonstrated unambiguously. Different with Ni/Al₂O₃, the La-modified Ni/Al₂O₃ shows a clear CH₄ conversion enhancement by nonthermal plasma which is contributed by enhanced adsorbed carbonates formation over the lanthanum. However, the influence of carbonates species on coke formation behavior is

expected to be investigated [4]. More importantly, X-ray photoelectron spectroscopy (XPS) should be carried out before and after experiment to understand behavior of lanthanum. Chemical shift of La3d binding energy may be observed if the carbonate species are adsorbed on the La sites rather than other basic site, i.e. dispersing agent magnesium oxide. In this case, the oxidation state of La in complex La-Ni-Al oxide could be confirmed.

Optimization of interaction between DBD and catalyst is still an important work, and there is a long way to go. Interaction of DBD and catalyst pellet occurs only at the external surface of the pellets, and the effected thickness is ca. 20 μm [5], which means a majority of the active sites in micropores of catalyst do not interact with any excited species. As Chapter 1 mentioned, the scale of plasma species is too short compared with that of chemical reaction so that the morphology of pore and catalyst dramatically impact the flux of plasma species on the active site. Moreover, the mass transfer resistance [2] maybe excluded with a modified catalyst microstructure where pure plasma catalysis (Chapter 5) is expected. The powder of catalyst is widely employed in thermal catalysis, however, only surface contact with plasma in plasma-enabled catalysis based on the Chapter 2 analysis. For an uniform heterogeneous catalysis, the fluidized bed reactor could provide a potential approach to enhance the interaction between plasma species and catalyst powder [6]. In this case, diffusion-controlled regime could be ignored even at high temperature.

Finally, the in situ plasma-DRIFTS experiment was carried out at 200 °C limited by heat tolerance of the plasma-DRIFTS chamber. However, the plasma enabled reforming is commonly operated at 500~600°C [7]. In this case, CO₂ activation with plasma at high temperature is still unclear. Indeed, the desorption rate may be accelerated at high temperature that it is difficult to detect the surface species. The gas-phase change could be detected by the QMS. In the DRIFTS experiment, the interval time for recoding is 30s (26-scan accumulation), while the time scale for absorption, surface reaction, and desorption is much shorter. Therefore,

a rapid scanning of IR measurement is necessary. The QMS is sensitive to respond to the change of gas species (scanning scale is in ns~s). In overall, for a better understand of plasma-enable Langmuir-Hinshelwood mechanism, it is necessary to combine the IR setup and QMS together for an overall pathway reaction exploration.

6.3 References

- [1] K. Li, F. He, H. Yu, Y. Wang, Z. Wu, Theoretical study on the reaction mechanism of carbon dioxide reforming of methane on La and La₂O₃ modified Ni(1 1 1) surface, *Journal of Catalysis* 364 (2018) 248-261.
- [2] S. Kameshima, R. Mizukami, T. Yamazaki, L.A. Prananto, T. Nozaki, Interfacial reactions between DBD and porous catalyst in dry methane reforming, *Journal of Physics D: Applied Physics* 51 (2018).
- [3] K. Yuan, J.Q. Zhong, X. Zhou, L. Xu, S.L. Bergman, K. Wu, G.Q. Xu, S.L. Bernasek, H.X. Li, W. Chen, Dynamic oxygen on surface: Catalytic intermediate and coking barrier in the modeled CO₂ reforming of CH₄ on Ni (111), *ACS Catalysis* 6 (2016) 4330-4339.
- [4] K. Li, X. Chang, X. Li, S. Chen, X. Zhang, S. Assabumrungrat, Z.-J. Zhao, L. Zeng, J. Gong, Ordered mesoporous Ni/La₂O₃ catalysts with interfacial synergism towards CO₂ activation in dry reforming of methane, *Applied Catalysis B: Environmental* 259 (2019) 118092-118092.
- [5] Z. Sheng, S. Kameshima, S. Yao, T. Nozaki, Oxidation behavior of Ni/Al₂O₃ catalyst in nonthermal plasma-enabled catalysis, *Journal of Physics D: Applied Physics* 51 (2018) 445205.
- [6] Q. Wang, Y. Cheng, Y. Jin, Dry reforming of methane in an atmospheric pressure plasma fluidized bed with Ni/ γ -Al₂O₃ catalyst, *Catalysis Today* 148 (2009) 275-282.
- [7] Z. Sheng, K. Sakata, Y. Watanabe, S. Kameshima, H.-H. Kim, S. Yao, T. Nozaki, Factors determining synergism in plasma catalysis of biogas at reduced pressure, *Journal of Physics D: Applied Physics* 52 (2019) 414002.